Politecnico di Torino

TU Delft

POLITECNICO DI TORINO

Master's Degree in Aerospace Engineering
A.a 2021/2022
Graduation session October 2022

Aerodynamic and Aeroacoustic Analysis of a Ducted Fan with a Variable Nozzle in an Over-the-Wing Configuration

Supervisors

Prof. Gioacchino CAFIERO

Prof. Francesco AVALLONE

Prof. Gaetano IUSO

Candidate

Andrea CAVINI

10 2022

Abstract

In recent years, hundreds of start-ups have emerged intending to extend urban and regional transport to a new vertical dimension, reducing the time taken to travel between two points and opening the door to countless applications for this new category of aircraft. To date, several e-VTOL architectures have been proposed, most of which employ propellers to generate lift and thrust. However, since the noise generated by these aircraft is a key element, research into propulsion solutions that limit the noise impact is essential. Among the proposed architectures, the most promising seems to be the Duct Electric Vectored Thrust (DEVT) as it would allow not only to reduce the noise produced but also to use the engine itself as a thrust vector system. This thesis, developed in collaboration with the department of Flow Physics and Technology (FPT) at Delft University of Technology, aims to analyze and characterize the effect that a variable nozzle has on the fluid dynamics and aeroacoustics field of an electric ducted fan in an Over-the-Wing (OTW) configuration. The three-dimensional CAD model of the propulsion system used in the analyses was built from an architecture already employed within the department adapted to reproduce the technological solution proposed by the German company Lilium. As a first step, four different configurations with varying duct exit area were analyzed using low-fidelity numerical simulations to determine how nozzle variation affects the engine performance. Based on these analyses, the two most significant configurations were selected for a detailed numerical investigation to illustrate the differences in performance and noise generated by the two configurations. The 3DS PowerFLOW® flow solver was used for the high-fidelity computational analysis. The solver implements the LBM (lattice-Boltzmann) method along with a VLES (Very Large Eddy Simulation) turbulence modelling approach to solve the flow field. On the other hand, far-field acoustic analyses were conducted from data acquired in the fluid dynamics simulations by employing the Ffowcs Williams–Hawkings (FWH) acoustic analogy. It has been demonstrated that the configuration of the nozzle influences the flow-dynamic characteristics of the ducted fan. Closed nozzles result in lower thrust and efficiency. Nevertheless, the data suggest that there is a limit beyond which the increase in area will negatively affect performance. In accordance with the literature, the duct causes a directivity effect, as shown by the acoustic analyses. Finally, between the two configurations chosen for the acoustic analysis, it is found that the configuration with the largest output area produces produces the higher sound level.

Acknowledgements

Vorrei ringraziare i professori Gioacchino Cafiero e Francesco Avallone relatori di questo progetto di tesi. In particolare, il prof. Cafiero per avermi dato l'opportunità di svolgere il progetto di tesi presso l'Università Tecnica di Delft e il prof. Avallone per avermi seguito durante questo lungo e tortuoso percorso che mi ha portato a espandere le mie conoscenze in ambito così complesso ma innovativo come l'Aeroacustica. L'esperienza a Delft è un qualcosa che di certo mi porterò nel cuore per molti anni.

Table of Contents

List of Tables

List of Figures

Chapter 1

Introduction

In recent years, despite the Coronavirus crisis, the Urban Air Mobility (UAM) market has increased exponentially, attracting more and more companies and investors. At the heart of this new sector is a new category of aircraft, the electric vertical take-off and landing vehicles known as eVTOLs. As the name suggests, these aircraft can take off and land vertically, reducing the size of the surfaces needed to handle them and enabling urban flight thanks to their high manoeuvrability. Unlike previous VTOLs, eVTOLs are distinguished by the use of an all-electric propulsion system. This technology fits in with the current trend in the aviation sector towards a constant search for systems with a reduced environmental impact in terms of both harmful gas and noise emissions. The UAM market is forecast to grow from USD 2.6 billion in 2020 to USD 9.1 billion by 2030 [1].

(a) eVTOL for Air Taxi porpuses

(b) Delivery UAV

Figure 1.1: Examples of application of the UAM technologies in the urban context

But what does Urban Air Mobility represents? The new UAM embody the potential answer to a series of growing problems that we will start to face soon or later, as

well as represents a new push for the self-driving vehicles industry. First, UAM represents the idea of extending urban transportation to the airspace. The global urban population is projected to grow in the next years, United Nations forecast that by 2030 60% of the world's population will be urban [2]. A new level of transport will be necessary to reduce land traffic but also travel time (Figure 1.1a). UAM can also improve connectivity between cities, in a future where people will be more and more connected. In addition, the introduction of electric vehicles such as eVTOLs to move people will lead to an increasingly significant reduction (the more this technology is adopted) in greenhouse gas emissions from urban transport. Finally, the new urban air mobility will lead to the application of small unmanned aerial vehicles (UAVs) for goods deliveries (Figure 1.1b). Nasa has forecasted that by 2030 over 1.4 B express packages could be delivered by Unmanned Aircraft Systems (UAS) [3].
In this project, the main focus will be on the propulsion technology behind eVTOls for passenger transport; UAVs will not be directly addressed, even though the propulsion technology behind the two aircraft is essentially the same but obviously on a different scale.

1.1 eVTOLs: configurations and technology

The eVTOLs market appears set to take off, within a few years we can expect to see "flying cars" become the most popular transportation system in big cities. Today, many state-funded projects, established aviation companies, and emerging start-ups are developing various concepts of electric vertical take-off aircraft, a map summarising the projects currently active worldwide is shown in Figure 1.2. As the number of participating companies increases, the design landscape of eVTOLs is also enriched with new ideas and configurations.
In general, eVTOLs can be categorised based on the type of application as follows [4]:

- **City Taxis** will fly within densely populated urban areas, covering distances from 15 to 50km;
- **Airport Shuttles** will transfer passengers from transport hubs or points of interest to airports between 15 and 50km
- **Inter City flights** will cover commuter routes of up to 250 km between major cities.

Each of these categories has different performance requirements, that's why the eVTOLs market is characterised by a series of different architectures. However, they all share a fundamental requirement: low noise emission. This is essential

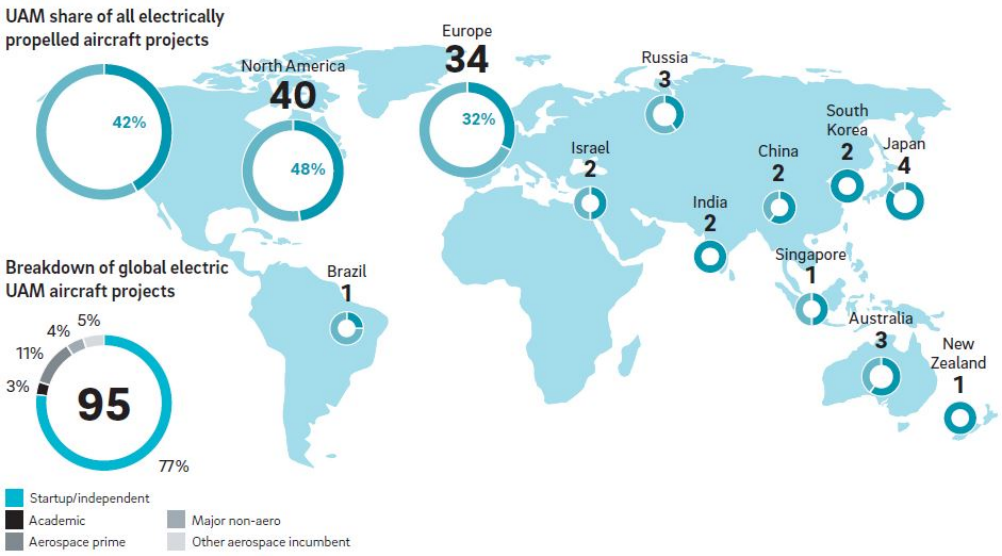

Figure 1.2: Distribution of the 95 known electric UAM aircraft projects

to guarantee the operation of these aircraft inside urban areas while respecting people's health.

Common eVTOLs design are presented in Figure 1.3. The main difference between the architecture is how lift is generated by the aircraft [4].
The *Multi-copter* category has a simple design and it's very efficient during vertical take-off, landing and hovering phases thanks to the low disc-loading. Multi-copter generates lift through the rotation of propellers but loses efficiency during the cruise as it does not have aerodynamic surfaces that generate lift. This type of eVTOL can only be used for urban air mobility applications with a low-range mission.
The second category is *Lift + Cruise*, an architecture combining the features of a multi-copter and those of a normal cruise aircraft: a multi-propeller system and an aerodynamic lift surface that can be considered as a wing. This layout has fewer propellers and a shorter chord to reduce drag during the cruise flight, it has good performance in both vertical take-off and landing and cruise but a high rotation speed of the propellers can produce a meaningful noise emission issue. Despite the noise problem the Lift + Cruise can be used for UAM applications.
The third category of eVTOL is called *Tilt Rotor*, it differs from the previous ones by the installation of a complex system that allows the wing and propeller or the propeller alone to rotate increasing the overall performance of the aircraft. When transitioning from hover to forward flight phase, the propulsion system, and in some cases the whole wing, is rotated 90 degrees. In this case, the pitch of propellers can be changed on the base of the mission phase to optimise their efficiency. While

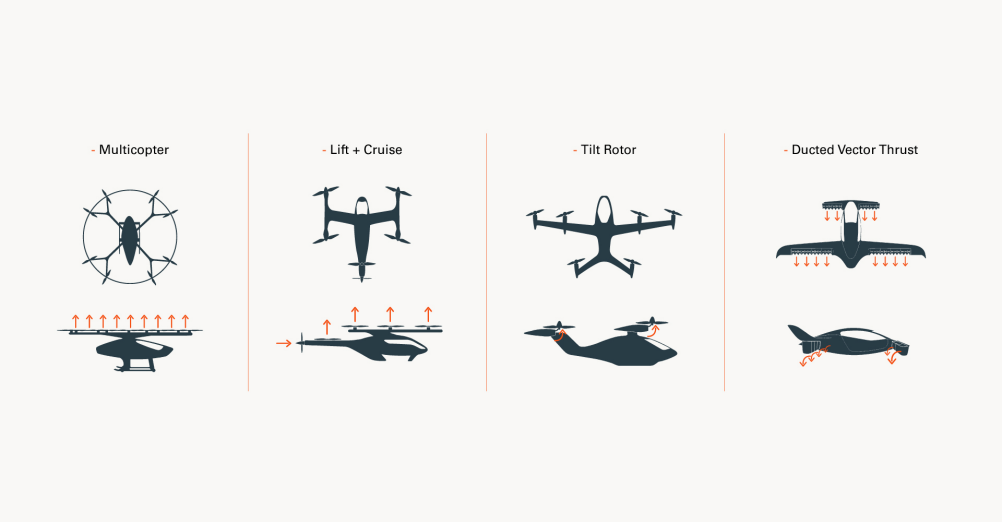

Figure 1.3: Different eVTOLs configurations

on the one hand, the use of this architecture increases the aircraft's operating range, enabling it to perform RAM (Regional Air Mobility) missions by connecting nearby population centres, on the other, the use of a tilt-rotor and pitch mechanism increases its complexity and weight. Flight dynamics and propeller design are very challenging for engineers and developers working on this type of eVTOL, however, this architecture proves to be the most versatile.

All the eVTOL categories covered so far feature a propeller propulsion system but this is not the only system used in this category of aircraft. The fourth category is probably the most advanced one in terms of aerodynamic efficiency and noise reduction. The Ducted Electric Vector Thrust (DEVT) is based on a system of ducted fans distributed over the wings (OTW) which, as in the case of the previous category, can be rotated by 90 degrees according to the flight phase. The main benefit of a ducted fan over an unducted propeller is the significant noise reduction that can be achieved by targeted optimization and the use of acoustic liners This is crucial if we consider that this type of aircraft will have to carry passengers on board and take off/land from surfaces located near residential areas (think about the noise emitted by a helicopter when it flies overhead).
Moreover, when referring to a distributed system of ducted fans there are two possible configurations. One is a configuration that provides the installation of this system away from the aerodynamic surfaces of the aircraft so as not to disturb the flow on the wing. Another possibility is instead to locate the ducted fans over the wing thus introducing interaction with the flow that laps the wing and recalling the concepts of aircraft where boundary layer ingestion is applied. This second

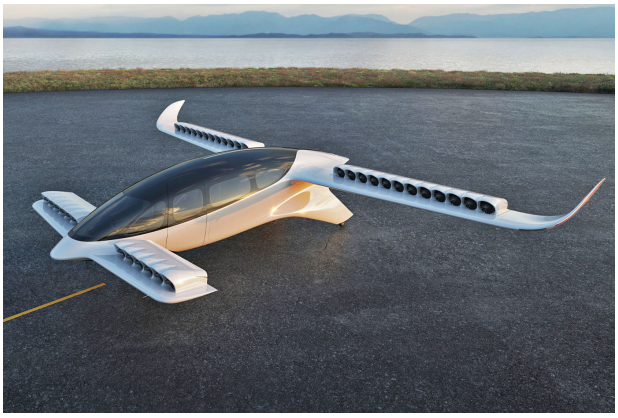

Figure 1.4: Lilium jet ducted fan architecture

design is what the project will focus on, in particular, the system developed by the Lilium jet will be taken as an example (Figure 1.4), this design is characterised by 36 electric ducted fans situated over aircraft's canard and main wing with a ratio of 1:2 between the two surfaces (12 engines located on the canard and 24 on the main wing).
This distinctive distributed architecture is also being considered a possible solution for large passengers aircraft. As demonstrated by ONERA's DRAGON distributed electric hybrid drive concept (Figure 1.5), the application of this electric drive configuration on a 150-passenger aircraft can have significant benefits in terms of fuel consumption (-7%) compared to a reference turbofan aircraft with the same EIS over a design range of 2750 nm [5]. In this concept, however, the distributed ducted fans system is located under the wing. In the case of our interest, we will only focus on the OTW configuration.

Figure 1.5: ONERA's DRAGON concept with distributed ducted fan

1.2 Research goals

When referring to an aircraft, weight is a parameter that strongly affects efficiency and must be limited. In the case of electric aircraft, excessive battery weight or reduced battery life due to high power consumption can limit aircraft performance. It is therefore of fundamental importance to implement a propulsion system that ensures high efficiency in all the different flight phases. In this way, it is possible to increase the operating range of the aircraft.
While eVTOLs that feature a propeller propulsion system are usually equipped with variable pitch blades that allow the aircraft to have near constant efficiency over a range of airspeeds, ducted fan eVTOLs do not feature this system as their design is closer to that found in aircraft turbofans. If from the first point of view the ducted fan seems less efficient, in reality, this system has a big advantage over rotors in terms of noise emission. This architecture, in fact, thanks to the presence of the duct, greatly reduces the sound produced by the engine. Low noise emission is a key feature for vehicles that will operate in urban areas, so the ducted fan has the potential to become an alternative to classic multi-rotor systems.
Germany-based company Lilium solved the high-efficiency requirement by implementing a variable area nozzle (VAN) at the exit of the duct on their eVTOL which ensure high efficiency in both cruise and hover [4]. By changing the effective exit area the operating point of the fan is shifted on the efficiency curve to a higher value that in a fixed-geometry design it would not be possible to achieve. In Figure 1.6 a section of a Lilium-like architecture (a) and schematic representation of the variable nozzle operation (b) are presented.

When modifying the exit section the acoustic footprint generated by the engine is altered, and new turbulent phenomena and a variation in the exit velocity affect the acoustic field which will then behave differently than in the previous condition. Therefore it is important to assess if the effect of this modification is negative in terms of SPL generated by the propulsion system. Furthermore, distributed over-the-wing ducted fan configuration could potentially lead to an increase in aerodynamics efficiency of the wing in cruise by affecting its pressure field. The wing would then find itself working in high lift conditions and so at high efficiency. However, in this investigation, only the hover condition has been considered.

The primary objective of this thesis is to investigate how the aerodynamic and therefore the aeroacoustic field of a ducted fan installed in an over-the-wing (OTW) configuration is influenced by the variation of the area ratio σ (or expansion ratio) defined as follows:

$$\sigma = \frac{A_{exit}}{A_{disk}} \tag{1.1}$$

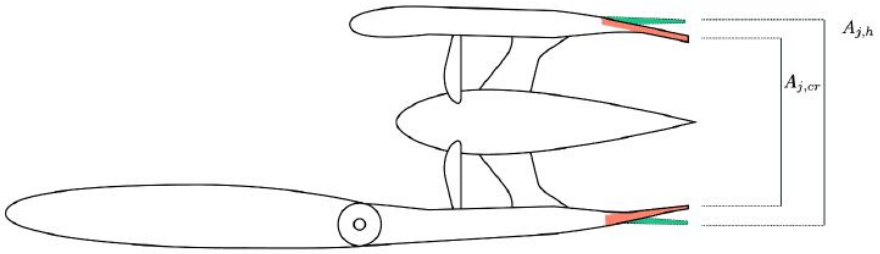

(a) Lilium over-the-wing ducted fan design

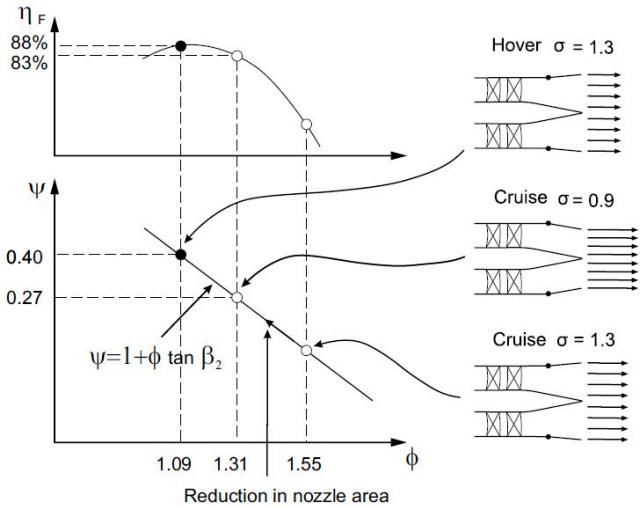

(b) Effect of a variable area nozzle on fan performance

Figure 1.6: Lilium thrust system (η is the fan efficiency, σ is a ratio of the area of the exit nozzle and the area of the duct in which the fan is located, ϕ is the flow coefficient and ψ is the fan stage loading coefficient) [4].

where A_{disk} is the area of the rotor disk and A_{exit} is the area at the exit of the duct. The effect of σ on the engine will be addressed mainly in hover configuration, with the engine rotated of 90° with respect to the cruise configuration. Once the overall effect of the nozzle has been determined, the two most significant cases will be selected. In this case, the acoustic fields of the two configurations will be analyzed and compared to assess the effect of the nozzle settings on the noise footprint.
The goals will be achieved by meeting the following objectives:

1. Understanding the aerodynamic and acoustic characteristics of ducted fan operating at typical RPM for eVTOL application, identifying the main fluid-dynamic phenomena that affect performance as well as noise emission.

2. Quantifying and analyzing the changes of the engine performance concerning

different working conditions, in particular by modifying the RPM of the rotor and σ.

3. Find the σ value that provides the best performance under the assumptions made. Compare the aerodynamic and acoustic characteristics of the chosen nozzle configuration with a significant other operating under the same conditions at a meaningful distance in relation to e-VTOL regulations.

The first objective is met by carrying out an extensive literature review. The findings from the literature review are discussed in Chapter 3. The second objective has been achieved by carrying out a low-fidelity computational analysis of the engine in different working conditions. We are not interested in a deep focus on the performance of the engine but to understand the trend that these changes determine on the engine performance map and verifying the positive effect of a higher σ on the engine in the hover case. From these analyses, an optimal value of σ for the engine operating in hover condition is selected together with another. The last objective has been achieved by carrying out a high-fidelity computational analysis of the two nozzle configurations. In Chapter 5 complete details of the numerical setup are discussed.
The following section covers the approach taken to reach the objective and the motivation behind its selection.

1.3 Approach

Based on the literature review, which showed that the topic has not been practically covered except for applications on drones and UAVs, and taking into account the few experimental studies conducted on the topic, conducting a computational study was considered the best approach. The lack of established geometries that respected the characteristics sought for the ducted fan led to the need to create a model from scratch.
The geometry of the turbofan model used by NASA during the Source Diagnostic Test (SDT) whose use is strictly reserved for research purposes within the Delft University of Technology was selected for the realization of the analysed model. The design of the original nacelle has been modified to allow the installation of the engine on the trailing edge of a wing and to reduce the aerodynamic interference between the two. For the wing, a NACA 0010 airfoil has been selected as it is a well-known profile with many available data in the literature. The wing has been then divided into two parts to realize the rotation system of the section where the engine is installed.
Overall the realization of the model has taken a good part of the time dedicated to the project because of the complexity of the geometry which is best described in

the first part of Chapter 5. The exit nozzle has been designed to have two separate sections that can rotate to allow the variation of the output area and therefore of the parameter σ. In the analysis, the variation of this element is done by modifying the .stl file imported into the solver.
A total of 12 medium resolution simulations varying RPM and the area ratio (σ) were performed on the engine already installed on the wing. This has allowed the outlining of the impact that the variation of the output area has on the engine performance. Then, fine-resolution simulations were performed to analyze and compare the acoustic field of the engine in hover configuration for two values of σ. For the high fidelity computational analysis performed in this study the flow solver PowerFLOW®, developed by Dassault Systèmes has been utilized. It implements the lattice-Boltzmann method (LBM) alongside a very large-eddy simulation (VLES) turbulence modelling approach to resolve the flow field. The reason for choosing such a solver over a traditional Navier-Stokes-based solver is their higher computational efficiency, lower dispersion, and dissipation errors [6]. The computation of the acoustic field is performed using the Ffowcs Williams–Hawkings (FWH) analogy. A more detailed discussion on the flow solver and the computational setup has been carried out in Chapter 4 and 5 respectively.

1.4 Thesis outline

The organization of this thesis is as follows. Together with this chapter, the document consists of 9 chapters a brief introduction to which has been provided below:

- **Chapter 1** : an introduction to the growing UAM field and commonly used VTOL designs are presented as well as the aim of the project and the related problem.
- **Chapter 2** : introduces the reader to the theoretical foundations of ducted fan aerodynamics and the fundamental concepts of acoustics and aeroacoustics being used in the thesis.
- **Chapter 3** : results obtained in other research concerning the problem analyzed in this thesis are discussed. This literature review allows for a comprehensive view of the problem and the phenomena expected to be found.
- **Chapter 4** : introduces the principles of the Lattice Boltzmann Method (LBM) and its implementation in the flow solver used for the analysis. The chapter also discusses how the FWH aeroacoustic analogy is implemented in the aeroacoustic solver of the tool.

- **Chapter 5** : presents the setup created to perform the analysis in PowerFLOW®. The chapter includes the process used in creating the geometry and a description of the computational setup. Special emphasis is given to mesh resolution and simulation parameters.
- **Chapter 6** : results from the grid resolution study are discussed.
- **Chapter 7** : results from the Engine performance analysis are presented. First, the effect of exit area variation on performance is discussed. Then, the cases chosen for the high-resolution analysis are presented.
- **Chapter 8** : Fluid dynamic and Aeroacoustics results from the high-resolution simulations are discussed. Finally, noise sources are identified, and the acoustic results are related to the unsteady fluid dynamic phenomena present in the flow field.
- **Chapter 9** : provides the conclusions to the thesis. Key findings from the analysis are collected and their importance is discussed. The chapter concludes with recommendations and advice for possible developments of the project.

Chapter 2

Theoretical Background

In this chapter, a theoretical background and concepts that will be used throughout the thesis are provided to the reader. In section 2.1 the fundamentals of the theory behind the aerodynamics of ducted fan are discussed. Basic definitions of the acoustic theory and the phenomena that see the generation of sound in fluid-solid interaction are then discussed in Section 2.2. Finally, the aeroacoustics analogies are described in section 2.4. Particular attention is given to the Ffowcs-Williams-Hawking (FWH) acoustic analogy since it is the one on which the far field analysis carried out in this project is based.

2.1 Performance of Ducted Fan

A ducted fan consists of a propeller inserted into an annular duct with an airfoil-like section, which can be either symmetric to the rotation axis or asymmetric. It can be considered as a hybrid between a propeller and a turbofan engine, where the turbofan is nothing more than a ducted fan driven by a turbojet engine. The role of the duct is to guide the fluid through the blade space, however, its primary duty is more complex. For a ducted fan the total thrust T is composed of two contributions: one from the rotor T_r and one from the duct itself T_d. The contribution of the duct to the total thrust may reach up to 30% in high-loaded engines[7]. The beneficial effect of this architecture is twofold. By increasing the pressure differential around the rotor disc, the total thrust that can be generated is significantly increased, as is the propulsive efficiency of the engine.

A simple first-order analysis of the performance of a ducted fan can be done using the *Momentum Theory* as for an open rotor. The *Momentum Theory* is based on the conservation's laws of fluid dynamics, also some simplifications are assumed. In particular inviscid, incompressible steady and quasi-dimensional flow is assumed.

In addition, for the ducted rotor, it is assumed that the flow at the diffuser exit has expanded back to ambient atmospheric pressure. Figure 2.1 show the flow models in hovering condition for both open and ducted rotor.

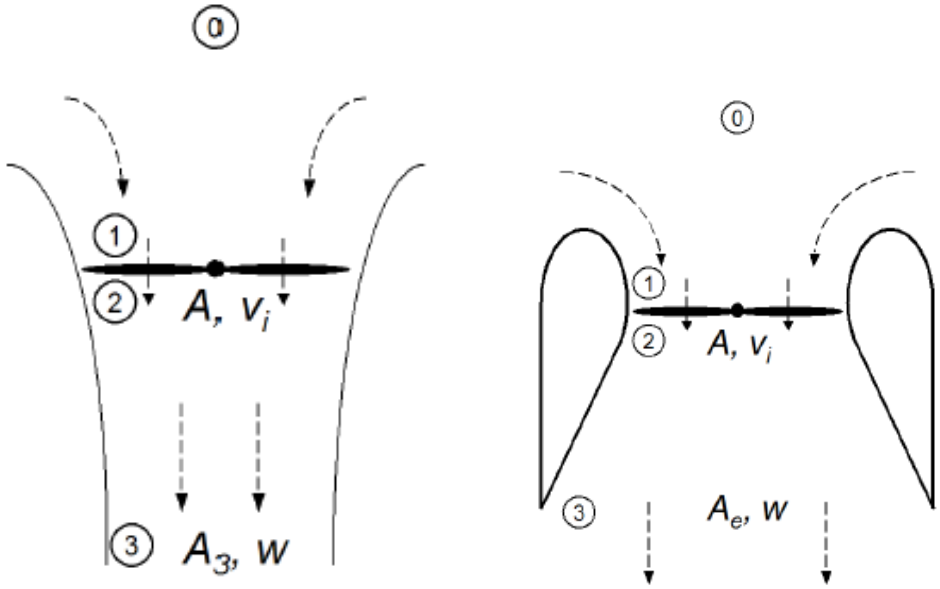

(a) Open rotor **(b)** Ducted rotor

Figure 2.1: Flow-field model in hover condition for an open rotor (a) and a ducted rotor (b)

The free-stream condition is represented by Station 0. Stations 1 and 2 are located immediately above and below the rotor disk's plane, respectively. Station 3 is at the diffuser's exit plane for the ducted rotor while for the open rotor it is the far wake indefinitely downstream. A key parameter which impact the performance of a ducted rotor is represented by the diffuser expansion ratio σ, which is equal to the ratio between the outlet area A_{exit} and the disk area A_{disk}:

$$\sigma = \frac{A_{exit}}{A_{disk}} \tag{2.1}$$

By considering the hover case, the following boundary conditions are determined:

- Velocities: $V_0 = 0 \quad V_1 = V_2 = V_i \quad V_3 = W$
- Pressure: $p_0 = p_3 = p_{atm}$
- Areas: $A_1 = A_2 = A_{disk} \quad \text{and} \quad A_3 = A_{exit} \cdot \sigma$

2.1.1 Momentum Theory: Ducted Rotor

In the case of a ducted rotor, the conservation equations take into account the effect of the area ratio σ. In particular, the conservation equations are written as follows.

$$\text{Conservation of Mass:} \quad \dot{m} = \rho V_i A_{disk} = \rho A_{exit} V_{exit} \tag{2.2}$$

from which the exit velocity is found to be:

$$V_{exit} = \frac{V_i}{\sigma} \tag{2.3}$$

$$\text{Conservation of Momentum:} \quad T_{total} = \dot{m} V_{exit} = \rho A_{disk} \frac{V_i^2}{\sigma} \tag{2.4}$$

$$\text{Conservation of Energy:} \quad P = \frac{1}{2} \dot{m} V_{exit}^2 \tag{2.5}$$

from which a relation between ideal Power and Total thrust can be written as:

$$P = \frac{1}{2} \frac{T_{total}^{3/2}}{\sqrt{\rho A_{exit}}} \tag{2.6}$$

For a ducted rotor the actuator-disk model is used just to derive the expression of the rotor thrust T_{rotor}:

$$T_{rotor} = \Delta p A_{disk} = \frac{1}{2} \rho A_{disk} V_{exit}^2 \tag{2.7}$$

The theoretical relation between the thrust generated by the rotor and the total is, therefore:

$$\frac{T_{rotor}}{T_{total}} = \frac{1}{2} \frac{\rho A_{disk} V_{exit}^2}{\rho A_{disk} V_i V_{exit}} = \frac{1}{2\sigma} \tag{2.8}$$

In general, is preferred to use the performance-related parameters coefficients rather than the dimensional parameter. Thrust coefficient $C_{T_{total}}$ and power coefficient C_P are defined as follow.

$$C_{T_{total}} = \frac{T_{total}}{\rho \Omega^2 D^4} \tag{2.9}$$

$$C_P = \frac{P}{\rho \Omega^3 D^5} \tag{2.10}$$

The figure of merit is a parameter which is often used as an efficiency measure of ducted fans in hover conditions [8].

$$FM = \frac{C_T^{3/2}}{\sqrt{2} C_P} \tag{2.11}$$

Applying the momentum theorem, the thrust components given by the various elements (which contribute to the total thrust) are determined [9].

$$\frac{T_{diffuser}}{T_{total}} = -\frac{(\sigma-1)^2}{2\sigma} \tag{2.12}$$

$$\frac{T_{inlet}}{T_{total}} = \frac{\sigma}{2} \tag{2.13}$$

The figure below displays the effects of various thrust components on total thrust.

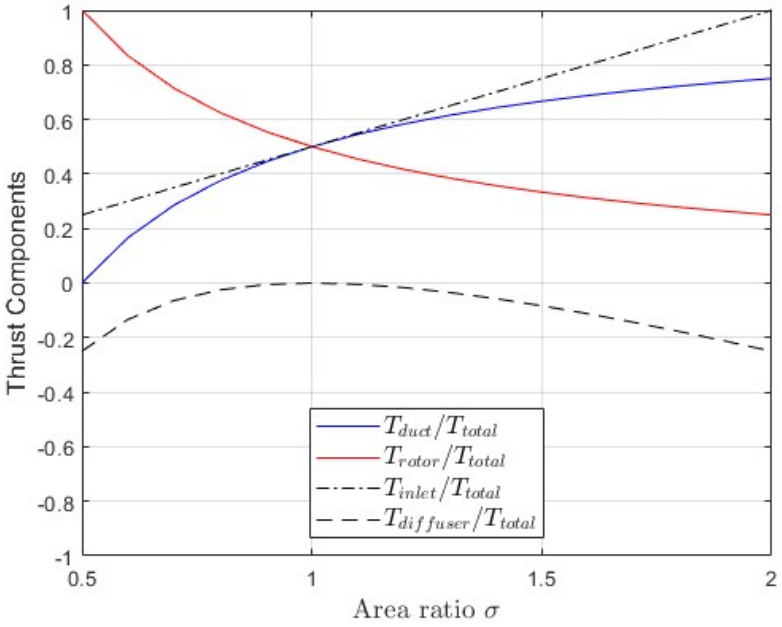

Figure 2.2: Ducted fan theoretical thrust components

From Figure 2.2 it is determined how the duct's contribution to total thrust increases as area ratio σ increases.

2.1.2 Momentum Theory: Open Rotor

For an open rotor, the following equations are determined from the conservation laws:

$$\text{Conservation of Mass:} \quad \dot{m} = \rho V_i A_{disk} \tag{2.14}$$

$$\text{Conservation of Momentum:} \quad T = \dot{m}(V_3 - V_0) = \dot{m}W \tag{2.15}$$

$$\text{Conservation of Energy:} \quad P = \frac{1}{2}\dot{m}w^2 \tag{2.16}$$

While the actuator disk model of the rotor is:

$$T = \Delta p A_{disk} \tag{2.17}$$

the power can also be written as:

$$P = TV_i \tag{2.18}$$

As done before with the ducted fan, the open rotor power can be related to the thrust:

$$P = \frac{T_{total}^{3/2}}{\sqrt{2\rho A_{disk}}} \tag{2.19}$$

The conservation of energy is nothing but Bernoulli's equation if applied between stations 0 and 1, and 2 and 3:

$$p_0 + \frac{1}{2}\rho V_0^2 = p_1 + \frac{1}{2}\rho V_1^2$$

$$p_2 + \frac{1}{2}\rho V_2^2 = p_3 + \frac{1}{2}\rho V_3^2$$

the pressure jump on the disk is:

$$\Delta p = \frac{1}{2}\rho V_3^2 \tag{2.20}$$

By combining equations 2.14,2.15 2.17 the relation between the rotor-induced velocity and the exit velocity is obtained:

$$V_{exit} = 2V_i \tag{2.21}$$

The momentum theory is predicting that the exit velocity of an open rotor is two times the induced velocity at the rotor disk. From this result is also possible to determine that the area of the open propeller wake is half the Area of the rotor disk. Therefore, the contraction of the slipstream exiting the rotor is predicted. From the conservation of mass:

$$\rho A_{disk} V_i = \rho A_{exit} V_{exit}$$

$$A_{exit} = \frac{A_{disk}}{2} \tag{2.22}$$

2.1.3 Momentum Theory: Ducted Rotor vs Open Rotor

A more meaningful comparison can be made between the performance of the ducted fan and that of the open rotor. From the previous equations, it is possible to relate the performance parameters of the two engines so that a visual comparison can be done. In particular from equation 2.19 and 2.6, which describe the relationship between fundamental performance characteristics of the two rotors, the following relationship is determined:

$$\frac{P_{DF}}{P_{OR}} = \frac{1}{\sqrt{2\sigma}} \left(\frac{T_{DF}}{T_{OR}}\right)^{3/2} \left(\frac{A_{disk_{OR}}}{A_{disk_{DF}}}\right)^{1/2} \tag{2.23}$$

By holding any two variables fixed between the two configurations the behaviours of the other variable can be analyzed. First, considering the two configurations producing the same amount of thrust T_{total} and have the same disk area A_{disk} (i.e. having the same disk loading) the following relations are defined:

$$\frac{P_{DF}}{P_{OR}} = \frac{1}{\sqrt{2\sigma}}$$

$$\frac{T_{rotor}}{T_{OR}} = \frac{1}{2\sigma}$$

$$\frac{V_{i_DF}}{V_{i_OR}} = \frac{\dot{m}_{DF}}{\dot{m}_{OR}} = \sqrt{2\sigma}$$

$$\frac{V_{exit_{DF}}}{V_{exit_{OR}}} = \frac{1}{\sqrt{2\sigma}}$$

Moreover, the relation between the specific thrust T_{total}/P_i of the ducted rotor and the open rotor is found to be:

$$\frac{(T_{total}/P_i)_{DF}}{(T_{total}/P_i)_{OR}} = \sqrt{2\sigma}$$

Figure 2.3 shows the performance comparison between a ducted rotor and an open one with the same total thrust and disk area. As the area ratio, σ increases the ideal power ratio decreases meaning that the ducted rotor needs less power to produce the same thrust as the open one. The same trend is followed by the rotor-induced velocity ratio. Also, the specific thrust T_{total}/P_i is increased with the area ratio σ as it follows the same pattern of the mass flow $\dot{m}$. The results can be linked to the analysis done earlier on the thrust components of the ducted rotor. By increasing the area ratio (also known as expansion ratio) the thrust component of the duct increases.

Another interesting analysis can be done while considering the two configurations consuming the same amount of (ideal) power P and having the same disk area A_{disk}. In this condition the following relations are found:

$$\frac{T_{DF}}{T_{OR}} = (2\sigma)^{1/3}$$

$$\frac{T_{rotor}}{T_{OR}} = \frac{1}{(2\sigma)^{2/3}}$$

$$\frac{V_{i_DF}}{V_{i_OR}} = \frac{\dot{m}_{DF}}{\dot{m}_{OR}} = (2\sigma)^{2/3}$$

$$\frac{V_{exit_{DF}}}{V_{exit_{OR}}} = \frac{1}{(2\sigma)^{1/3}}$$

Figure 2.4 shows the relations between the ducted rotor and open rotor performance parameters while increasing the area ratio σ. With the two configurations using the same amount of ideal power the total thrust produced by the ducted configuration continuously increases as the area ratio is increased. At the same time, the mass flow $\dot{m}$ and the induced velocity V_i also increases while the thrust component generated by the rotor itself (in the duct configuration) is reduced. The same trend is followed by the exit speed V_{exit}.

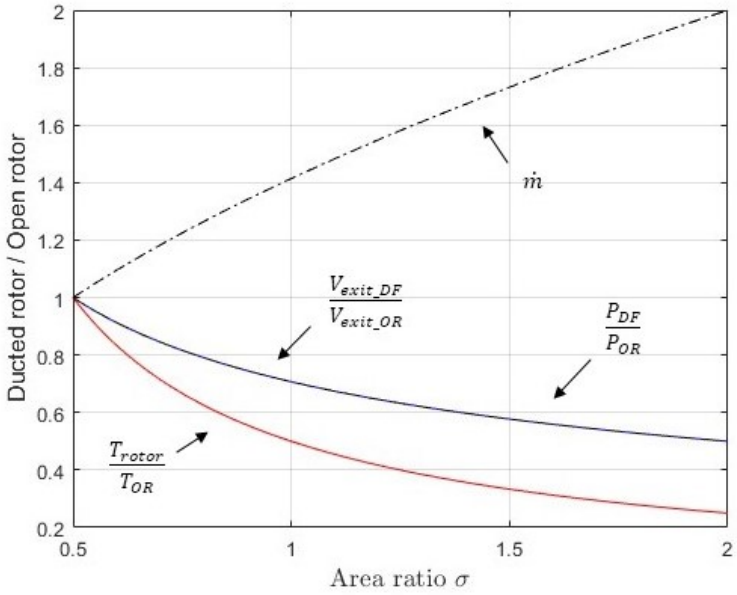

Figure 2.3: Comparison for same total thrust and disk area

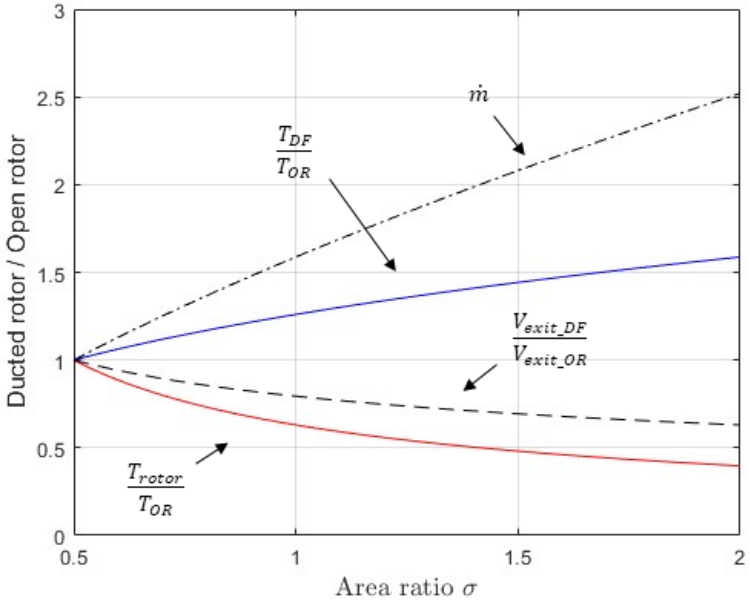

Figure 2.4: Comparison for the same power and disk area

From the previous analysis, the ducted rotor seems to perform better than the open configuration. For example, if we consider an area ratio of $\sigma = 1.0$ which would represent a duct exit area of the same size as the disk area, the ducted configuration can produce approximately 30% grater static thrust while consuming the same ideal power P_i. Alternatively, fixing the total static thrust, the ducted fan only requires 70% of the power of the free propeller. As seen, total thrust increases as σ increases, at least in theory.
The momentum theory does not take into account viscous effects such as skin friction losses and flow separation that would limit the ducted rotor performance. In addition, the behaviour of the airflow entering the duct is strongly influenced by the radius of the inlet lip and the pressure jump generated by the rotor (and thus by the rotational speed of the rotor). The stagnation point on the duct lip moves when the flow must turn more to enter the duct. If the duct inlet lips radius is not enough to guide the flow under those conditions, the flow will separate even before reaching the engine. The separated flow, ingested by the rotor, will result in increased noise and vibration, as well as additional losses that will affect performance. While the ducted fan can bring benefits, a careful design of the duct is of key importance. Moreover, the thrust increase must be evaluated along with the additional weight and drag that this configuration brings.

2.2 Basic concepts of Acoustics

The purpose of this and subsequent sections is to introduce the basic concepts of acoustics and aeroacoustics, which are necessary for the proper understanding of the methods applied in this study.

2.2.1 Sound

Sound, as we know it, is defined as an isoentropic pressure perturbation travelling in the form of longitudinal waves in a medium (solid, liquid or gas) at a fixed speed. The speed at which sound propagates is called the speed of sound and is generally associated with the letter c. The value of this speed depends on several physical parameters including the density and temperature of the medium. Considering air at $T = 20°$ and atmospheric pressure, the speed of sound in is $c_0 = 343\,m/s$.
Sound waves create a region of compression and expansion (Figure 2.5) in the propagation direction. The rate of expansion and compression defines the frequency of that particular sound wave.

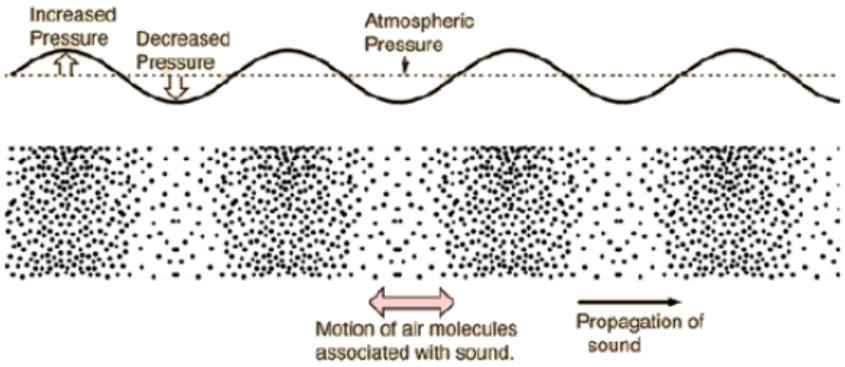

Figure 2.5: Mechanism of sound propagation [10]

The perception of sound that humans and animals have, is the response to a physical stimulus to the ear. The frequency range between $20\,Hz$ and $20\,kHz$ is detected by the human ear, it defines the sound frequency range of interest for acoustic analysis.
The propagation of sound waves produces a small variation of the local pressure in compressible media. Sound pressure p' is defined as the change in pressure with respect to a reference value p_0 (usually the atmospheric pressure).

$$p'(t) = p_0 + p(t) \tag{2.24}$$

2.2.2 Measurement of Sound

The ultimate purpose of sound measurement in most applications is to determine the level of annoyance that sound causes to a human listener. Since the human ear's sensitivity is logarithmic, measurements are usually made through the use of the sound pressure level (SPL) which transforms the pressure signal from a linear to a logarithmic scale expressed in decibel dB.

$$SPL = 10 \log_{10} \left(\frac{{p'_{rms}}^2}{{p_{ref}}^2} \right) \tag{2.25}$$

The reference pressure P_{ref} is the pressure against which the fluctuation is taken, which is in general, the atmospheric pressure $P_{ref} = 101325\ Pa$. In the SPL definition, the acoustic pressure root means square p'_{rms} is computed to better assess the strength of the pressure fluctuation. The root means square or rms is defined as:

$$p'_{rms} = \frac{1}{2T} \int_{-T}^{T} p'^2(t)\, \mathrm{d}t = \frac{1}{2T} \int_{-T}^{T} \left(p(t) - p_0\right)^2\, \mathrm{d}t \tag{2.26}$$

Sound is recorded through microphones as a very rapid pressure fluctuation. Since the rate of change of pressure is very high, it is easier to treat sound in the frequency domain than in the time domain. By applying the Fourier transform, it is possible to transform any time-dependent quantity from time-space to frequency space. Considering the function $p'(t)$ the Fourier transform $\hat{p}(\omega)$ is defined as:

$$\hat{p}(\omega) = \mathcal{F}_p(\omega) = \int_{-\infty}^{\infty} p'(t)\, e^{-i\omega t}\, \mathrm{d}t \tag{2.27}$$

while, according to Fourier's inversion theorem, $p'(t)$ can be obtained from $\hat{p}(\omega)$ using inverse Fourier transform:

$$p'(t) = \mathcal{F}_{\hat{p}}^{-1}(t) = \frac{1}{2\pi} \int_{-\infty}^{\infty} \hat{p}(\omega)\, e^{i\omega t}\, \mathrm{d}\omega \tag{2.28}$$

The contribution to the Overall sound pressure Level (OASPL) of the different frequencies which define the analyzed phenomenon can be computed once the Fourier transform of the time-dependent function has been applied. The OASPL provides a measure of the total energy in a noise spectrum and can also be used to characterize the directivity of the noise source.

2.3 The acoustic wave equation

Sound generation and propagation characteristics can be described using the wave equation. To derive this equation, we must first define fluid motion equations.

2.3.1 Conservation equations in fluid dynamics

The behaviour of fluid is governed by the Navier-Stokes equations, a system of coupled partial differential equations (PDE) which is obtained by applying the principles of conservation of mass, momentum and total energy to a control volume. The behaviour of the fluid can be described by using a coordinate system fixed in the space or one which moves with the fluid particle. These two methods are well known as the Eulerian and Lagrangian respectively. Because following all fluid particles and describing all variations around each particle along its trajectory is nearly impossible, the Eulerian method is preferred in applying the three conservation laws to the fluid (e.g. air or water). The thermodynamic variables such as pressure p and temperature T are thus position and time-dependent. Considering a compressible flow, the conservation equation can be written as [10]:

$$\textbf{Continuity} \quad \frac{\partial \rho}{\partial t} + \nabla \cdot (\rho \mathbf{u}) = 0 \qquad i = 1...3 \tag{2.29}$$

$$\textbf{Momentum} \quad \frac{\partial (\rho \mathbf{u})}{\partial t} + \nabla \cdot (\rho \mathbf{u}\mathbf{u}) = \nabla \cdot \mathbf{\Pi} + \rho \mathbf{f} \tag{2.30}$$

$$\textbf{Energy} \quad \frac{\partial (\rho E)}{\partial t} + \nabla (\rho E \mathbf{u}) = \nabla \cdot (\mathbf{\Pi} \cdot \mathbf{u}) - \nabla \cdot \mathbf{q} + \rho \mathbf{f} \cdot \mathbf{u} \tag{2.31}$$

$\mathbf{\Pi}$ is the stress tensor which is composed of an isotropic component and a non-isotropic component:

$$\mathbf{\Pi} = -p\mathbf{I} + \tau \Rightarrow \sigma_{ij} = -p\delta_{ij} + \tau_{ij} \tag{2.32}$$

The pressure p is the mean value of the stress tensor normal component σ_{ii}:

$$p = -\frac{1}{3} \sum_i \sigma_{ii}$$

and τ is the viscous stress term. To close the set of the equation the viscous stress is related to the velocity component following Newton's law

$$\tau_{ij} = 2\mu \underbrace{\frac{1}{2} \left(\frac{\partial u_i}{\partial x_j} + \frac{\partial u_j}{\partial x_i} \right)}_{Strain\ rate\ Tensor} + \lambda \delta_{ij} \frac{\partial u_k}{\partial x_k} \tag{2.33}$$

E is the total energy which is defined as the sum of the internal energy e and the kinetic energy $V^2/2$

$$E = e + \frac{V^2}{2}$$

while $\mathbf{q}$ is the heat flux that Fourier's law defined as:

$$q_j = -\kappa \left(\frac{\partial T}{\partial x_j} \right) = c_p \frac{\mu}{Pr} \left(\frac{\partial T}{\partial x_j} \right) \tag{2.34}$$

where κ is the thermal conductivity, Pr is the Prandtl number and μ is the dynamic viscosity. In conclusion, the Navier-Stokes equations contain seven unknowns: density ρ, pressure p, temperature T, the three velocity components $\mathbf{u} = [u\, v\, w]$ and the internal energy e. To close the system, in typical aerodynamics applications the perfect gas law

$$p = \rho R^* T \tag{2.35}$$

and the definition of the internal energy

$$e = c_v\, T$$

are considered.

2.3.2 Wave equation for stagnant uniform fluid

In Section 2.14 we defined the sound as a small pressure perturbation p' resulting from compressible effects. Assuming that an acoustic wave propagates in the medium isentropically, it is possible to show that the other quantities are also small and therefore the acoustic variables satisfy the linearized equations of motion. The relation between the pressure and the density fluctuation can be obtained from the state equation for an isentropic flow:

$$p' = \rho' c_0^2 \quad c_0^2 = \left(\frac{\partial \rho}{\partial p} \right)_s \tag{2.36}$$

where the constant of proportionality is given by the isentropic bulk modulus of the fluid $(dp/d\rho)_s$ and $c_0 = c_0(\rho, s)$ can be shown to be the speed at which small perturbations propagate i.e. the speed of sound [11] which is not necessarily a constant.
To simplify the derivation of the wave equation, we consider the case of acoustic perturbation (p',ρ',v'...) in a stationary ($v_0 = 0$) and uniform fluid, i.e. a fluid where the time average properties (ρ_0, p_0, v_0, s_0) are uniform.

Flow quantities can thus be broken down into average contributions and perturbation contributions when a perturbation $(\rho', p', v'...)$ is present in the field.

$$\mathbf{u}(\mathbf{x},t) = \mathbf{u_0} + \mathbf{u}'(\mathbf{x},t) \quad \left|\frac{\mathbf{u}'}{\mathbf{u_0}}\right| \ll 1$$

$$\rho(\mathbf{x},t) = \rho_0 + \rho'(\mathbf{x},t) \quad \left|\frac{\rho'}{\rho_0}\right| \ll 1$$

$$p(\mathbf{x},t) = p_0 + p'(\mathbf{x},t) \quad \left|\frac{p'}{p_0}\right| \ll 1$$

Considering the assumption of small perturbations and neglecting the second orders terms, the mass 2.29 and momentum 2.30 conservation law simplify into the linear acoustic equations:

$$\frac{\partial \rho'}{\partial t} + \rho_0 \nabla \cdot \mathbf{u}' = 0 \tag{2.37}$$

$$\rho_0 \frac{\partial \mathbf{u}'}{\partial t} + \nabla p' = 0 \tag{2.38}$$

where viscous effects τ as well as external forces $\mathbf{f}$ were neglected. In sound propagation, viscus effects are significantly smaller than inertial forces ($Re_a \gg 1$). Subtracting the divergence of the Eq. 2.38 from the time derivative of Eq. 2.37:

$$\frac{\partial^2 \rho'}{\partial t^2} - \nabla^2 \rho' = 0 \tag{2.39}$$

and using the constitutive equation 2.36 to express the density fluctuations as a function of the pressure fluctuations, we finally obtain the homogeneous linear acoustic wave equation:

$$\frac{1}{c_0^2}\frac{\partial^2 p'}{\partial t^2} - \nabla^2 p' = 0 \tag{2.40}$$

In the derivation of Eq. 2.40 source terms were not considered, therefore only the propagation process is described. In order to obtain the wave equation that takes into account the presence of noise sources, it is necessary to eliminate the assumptions of no external forces and mass sources. By rearranging the conservation laws and repeating the previous steps, it is possible to derive the non-homogeneous acoustic wave equation:

$$\frac{1}{c_0^2}\frac{\partial^2 p'}{\partial t^2} - \nabla^2 p' = q \tag{2.41}$$

where q represents the source terms, in the extended form it is written as:

$$\frac{1}{c_0^2}\frac{\partial^2 p'}{\partial t^2} - \nabla^2 p' = \frac{\partial Q_m}{\partial t} - \rho_0 \nabla \cdot \mathbf{f} \tag{2.42}$$

In the derivation of the Eq. 2.42 we are still considering acoustic waves as an isoentropic process, thus $ds = 0$. In the absence of this assumption, the equation of state between pressure density and entropy would apply $p = p(\rho, s)$. In differential form it would be written as:

$$dp = c^2 d\rho + \frac{p}{C_v} ds \tag{2.43}$$

while in the linear form:

$$dp' = c_0^2 d\rho' + \frac{p_0}{C_v} ds' \tag{2.44}$$

again, this equation can be used to derive the linear wave equation which in this case takes into account the change in entropy [10]:

$$\frac{1}{c_0^2}\frac{\partial^2 p'}{\partial t^2} - \nabla^2 p' = \frac{\partial}{\partial t}\left(Q_m + \frac{\gamma - 1}{c_0^2} Q_w\right) - \rho_0 \nabla \cdot \mathbf{f} \tag{2.45}$$

Therefore, in the linearized wave equation, the main sources of sound are represented by mass injection, momentum (through unsteady forces) and energy (through entropy fluctuations) fluctuation. These sources are usually distinguished according to the type of acoustic radiation in the medium surrounding them as *Monopole*, *Dipole* and *Quadrupole*.

2.3.3 Green's functions

As already mentioned, the wave equation 2.40 describes the propagation of sound in a stationary homogeneous medium. In general, one wants to calculate the value of the sound pressure $p'(\mathbf{x}, t)$ at the observer's position. Green's function formalism [12, 10] can be used to obtain an integral solution of the wave equation when sources are present.
Green's function G is defined as being a solution to the following inhomogeneous wave equation:

$$\frac{1}{c_0^2}\frac{\partial^2 G}{\partial \tau^2} - \frac{\partial^2 G}{\partial y_i^2} = \delta(\mathbf{x} - \mathbf{y})\delta(t - \tau) \tag{2.46}$$

which is completed by specifying the boundary conditions at a surface σ with outer normal $\mathbf{n}$ enclosing the volume Ω in which $\mathbf{x}$ and $\mathbf{y}$ are localized (Figure 2.6):

$$\mathbf{n} \cdot \nabla G + bG = 0 \tag{2.47}$$

It is distributed in space as a function of the observer position $\mathbf{x}$ and time t but also of the impulsive source $\mathbf{y}$ emitting at the time τ so that the solution will be $G(\mathbf{x}, t|\mathbf{y}, \tau)$. The sound heard at time t must be generated at time $\tau < t$ so that

$$G(\mathbf{x}, t|\mathbf{y}, \tau) = 0 \quad t < \tau$$

. This requirement is also known as the casualty condition which is one of the most important proprieties of the Green's function. The terms on the right-hand side of the equation represent the Dirac delta function which has the following proprieties:

$$\delta(t-\tau) = 0 \text{ when } t \neq \tau \text{ and } \int_{-T}^{T} \delta(t-\tau) \ -T < t < T$$

$$\delta(\mathbf{x}-\mathbf{y}) = 0 \quad \text{when} \quad \mathbf{x} \neq \mathbf{y} \text{ and } \int_V \delta(\mathbf{x}-\mathbf{y}) dV(\mathbf{y}) = \begin{cases} 1 \text{ when } \mathbf{x} \text{ is in V} \\ \\ 0 \text{ when } \mathbf{x} \text{ is not in V} \end{cases}$$

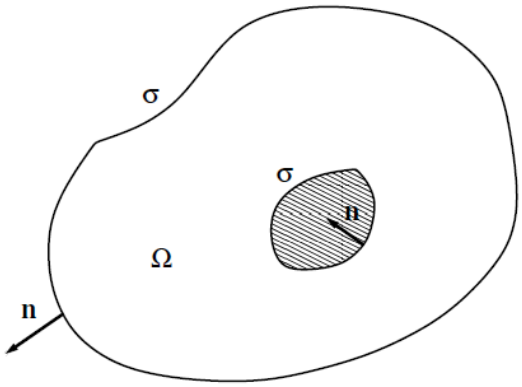

Figure 2.6: Volume Ω, surface σ and normal $\mathbf{n}$

In the general case of a generic source $q(\mathbf{y}, \tau)$ not necessarily vanishing before some time t_0 and considering a Green's function G not necessarily satisfying the actual boundary condition on Ω it is possible to find a solution to the wave propagation equation applying the following approach. First, the linear wave equation 2.41 multiplied by $G(\mathbf{x}, t|\mathbf{y}, \tau)$ is subtracted to the equation for the Green's function multiplied by $p'(\mathbf{y}, \tau)$. Then, integrating over the control volume Ω and times from an arbitrary time t_0 to the listener time t, yields:

$$\frac{1}{c_0^2}\int_{t_0}^{t}\int_{\Omega}\left(p'\frac{\partial^2 G}{\partial\tau^2} - G\frac{\partial^2 p'}{\partial\tau^2}\right)\mathrm{d}^3\mathbf{y}\mathrm{d}\tau - \int_{t_0}^{t}\int_{\Omega}\left(p'\frac{\partial^2 G}{\partial y_i^2} - G\frac{\partial^2 p'}{\partial y_i^2}\right)\mathrm{d}^3\mathbf{y}\mathrm{d}\tau$$
$$= \int_{t_0}^{t}\int_{\Omega} p'(\mathbf{y},\tau)\delta(\mathbf{x}-\mathbf{y})\delta(t-\tau)\mathrm{d}^3\mathbf{y}\mathrm{d}\tau - \int_{t_0}^{t}\int_{\Omega} q(\mathbf{y},\tau)G \ \mathrm{d}\mathbf{y}\mathrm{d}^3\tau$$

$p'(\mathbf{x}, t)$ is defined as:

$$p'(\mathbf{x},t) = \int_{t_0}^{t}\int_{\Omega} p'(\mathbf{y},\tau)\delta(\mathbf{x}-\mathbf{y})\delta(t-\tau)\mathrm{d}\mathbf{y}\mathrm{d}\tau$$

integration by parts is applied to the first and second integral, with respect to time and space respectively:

$$p'(\mathbf{x},t) = \int_{t_0}^{t}\int_{\Omega} q(\mathbf{y},\tau)G(\mathbf{x},t|\mathbf{y},\tau)\mathrm{d}\mathbf{y}\mathrm{d}\tau - \int_{\Omega}\left[\left(p'\frac{\partial^2 G}{\partial\tau^2} - G\frac{\partial^2 p'}{\partial\tau^2}\right)\mathrm{d}^3\mathbf{y}\mathrm{d}\tau\right]_{\tau=t_0}^{\tau=t} - \int_{t_0}^{t}\int_{\sigma}\left(p'\frac{\partial G}{\partial y_i} - G\frac{\partial p'}{\partial y_i}\right)\mathbf{n}\ \mathrm{d}\sigma\mathrm{d}\tau \quad (2.48)$$

The second integral can be eliminated in case the chosen initial conditions see $p' = 0$ and $q = 0$ at an initial time by considering $t_0 = -\infty$. The first integral represents the effect of the sources distributions $q(\mathbf{y},\tau)$, while the third integral represents the contribution to the perceived sound determined by the acoustic diffusion of the bodies immersed in the flow. In general, it represents the effect of differences between the actual physical boundary conditions on the surface S and the conditions applied to Green's function.

When an impulsive, point source $\delta(\mathbf{x}-\mathbf{y})\delta(t-\tau)$ is considered in the absence of walls, the only boundary is the one at infinity, where the Green's function and sources vanish, thus the contribution of the third integral to the solution is null. The solution to the wave equation 2.46 in this case is the so-called free-field Green's function G_0:

$$G_0(\mathbf{x},t|\mathbf{y},\tau) = \frac{\delta(t - \frac{|\mathbf{x}-\mathbf{y}|}{c_0} - \tau)}{4\pi|\mathbf{x}-\mathbf{y}|} \quad \text{when} \quad t > \tau \quad (2.49)$$

where $\tau^* = -\frac{|\mathbf{x}-\mathbf{y}|}{c_0}$ is the retarded or source time, it represents the time at which the source field must be known at the position $\mathbf{y}$. In this case, the boundary conditions correspond to the radiation or Sommerfeld condition which states that in an unlimited domain only outgoing waves have real existence. Mathematically it is expressed as:

$$\lim_{r\to\infty}\left(\frac{\partial G}{\partial t} + c_0\frac{\partial G}{\partial r}\right) = 0 \quad (2.50)$$

If solid bodies are present, the tailored Green's function is applied as it satisfies the same locally reacting linear boundary conditions as the actual field. In this case, the solution becomes:

$$p'(\mathbf{x},t) = \int_{-\infty}^{\infty}\int_{\Omega} q(\mathbf{y},\tau)G_0(\mathbf{x},t;\mathbf{y},\tau)\mathrm{d}\mathbf{y}\mathrm{d}\tau - \int_{-\infty}^{\infty}\int_{\sigma}\left(p'\frac{\partial G_0}{\partial y_i} - G_0\frac{\partial p'}{\partial y_i}\right)\mathbf{n}\ \mathrm{d}\sigma\mathrm{d}\tau \quad (2.51)$$

2.4 Aeroacoustic analogies

In the previous section, a linearized wave equation capable of describing the propagation of sound has been derived for a steady and uniform media. In this case, the sound is considered to be generated by a disturbance which results in a well-defined boundary motion. For turbulence flows like jets, however, no surface with a prescribed motion is present, thus noise must be generated by other mechanisms. Turbulence noise is generated by the action of inertia and compressibility when a vortex structure is subjected to a sudden change. The density fluctuation induced by unsteady pressures then propagates as sounds.
When describing the noise generated by turbulence is not always possible to make assumptions that allow the linearized equations of motion to be used. Acoustic analogies are applied in these cases, the objective is to determine the equations that describe the generation of sound waves that propagate to the acoustic far field, as distinct from defining the fluid motion in the turbulent flow [12]. This is achieved by rearranging the Navier-Stokes equations in various forms of the inhomogeneous acoustic wave equation enabling the use of CFD/CAA simulations to computationally predict noise in the far-field without the need for a large simulation domain with high resolution. In the following, the most important analogies for the thesis are presented.

2.4.1 Lighthill's analogy

Lighthill's analogy is an exact equation is not obtained through linearization of the equations but rather through a rearrangement of the Navier-Stokes' equations. The equation can be derived as follow. First, the divergence of the momentum equation is subtracted from the time derivative of the continuity equation, yielding:

$$\frac{\partial^2 \rho}{\partial t^2} = \frac{\partial^2 \left(\rho u_i u_j - \sigma_{ij}\right)}{\partial x_i \partial x_j} \tag{2.52}$$

where $\sigma_{ij} = -\mathbf{p}\delta_{ij} + \tau_{ij}$, the diagonal elements of the stress tensor are defined as gauge pressure $\mathbf{p}$. Considering the perturbation relative to a reference media with constant proprieties ($p_0 = 0$, $\rho_0 = 0$) and steady ($u_0 = 0$):

$$\mathbf{p}' = p - p_0$$

$$\rho' = \rho - \rho_0$$

$$u_i' = u_i$$

and subtraction from each side of the equation $\partial^2(\rho' c_0^2)/\partial x_i^2$ with c_0 is constant and represents the ambient speed of sound outside the flow, the Lighthill's equation is

obtained:

$$\frac{\partial^2 \rho'}{\partial t^2} - c_0^2 \frac{\partial^2 \rho'}{\partial x_i \partial x_j} = \frac{\partial^2 T_{ij}}{\partial x_i \partial x_j} \tag{2.53}$$

The term T_{ij} on the right side is known as the Lighthill's tensor.

$$T_{ij} = \rho u_i u_j + \left(p' - c_0^2 \rho'\right) \delta_{ij} - \tau_{ij} \tag{2.54}$$

It is a source term as it contains all the effects which generate the acoustic waves:

- $\rho u_i u_j$: Are the non-linear convective forces described by the Reynolds stress tensor
- $(p' - c_0^2 \rho') = 0$: Represents an entropy source term
- τ_{ij}: Viscous forces.

All of these sources have a double spatial derivation, making them quadrupole sources. The left side of the equation, on the other side, represents the radiation of waves from a finite volume of turbulent flow into a surrounding stationary medium [12]. Although equation 2.53 is exact, it is not so easier to solve than the Navier-Stokes equations. As a result, it is necessary to introduce some simplifying assumptions For high Reynolds number flow, the swirling component of the current is the dominant mechanism in sound generation. In these cases inertial effects outweigh viscous ones ($\tau_{ij} << \rho u_i u_j$). Moreover, if the same flow is considered to be almost incompressible (the Mach number of the flow is small) and homentropic so that entropy changes are no longer present $(p' - c_0^2 \rho') = 0$ and $\rho \approx \rho_0 = \text{const}$. It is possible to introduce the so-called Lighthill's approximation which makes Lighthill's equation explicit. The Ligthill's tensor in this case become

$$T_{ij} \approx \rho_0 u_i u_j$$

The conclusion of this approximation is that for an almost incompressible flow, Lighthill's source terms are non-linear and dependent on the velocity gradient. Noise is therefore generated by a nonlinear interaction, consequently, linear approximations if applied do not give the right result.

2.4.2 Ffowcs-Williams-Hawking (FWH) acoustic analogy

It is important to notice that in Lighthill's acoustic analogy 2.53 the source term models only free turbulence and does not take into account the effect of stationary or moving bodies in the flow. The presence of solid bodies in the flow affects the way sound waves are generated and radiated in the flow. Curle [12, 13] extended Lighthill's analogy to include the effects of a surface/solid body in the flow. However,

Curle's analogy considers the surface included in the media to be stationary.
In most aviation problems though, the noise is generated by moving elements such as rotor blades. In these cases, the analogies of Lighthill and Curle cannot be applied. Ffowcs-Williams and Hawkings (FW-H) equation represents an extension of Lighthill's and Curle's analogy for a flow where the solid interacting with fluid motions is itself in motion. In the FWH formulation, it is assumed that the acoustic

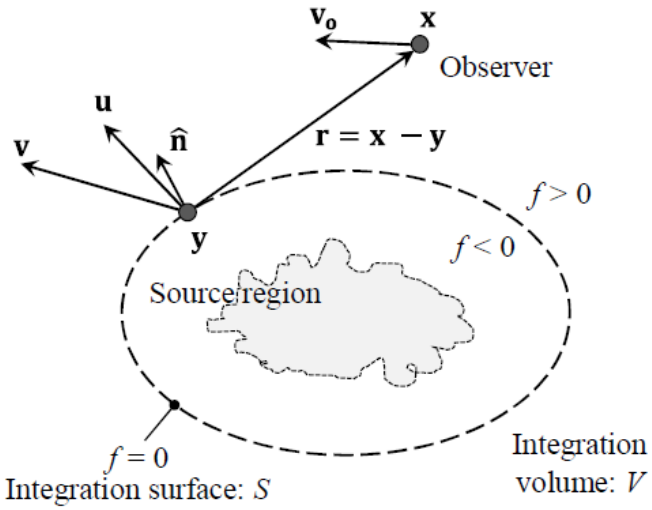

Figure 2.7: Problem definition of the FW-H acoustic analogy [14]

medium, at rest and the site of propagation, extends throughout the entire space, even in the space occupied by the body. The first step in the derivation of the FWH equation is the definition of a rigid control surface S enclosing the body in motion in the fluid whose points move with velocity $\mathbf{V}(\mathbf{x}, t)$. The surface S is described by a function $f(\mathbf{x}, t)$ such that $f < 0$ in the flow portion enclosed by the surface S, $f > 0$ outside the surface and $f = 0$ on the surface. Figure 2.7 shows how the fluid domain is divided, $\hat{\mathbf{n}}$ is the normal to the surface pointing outside such that $\nabla f = \hat{\mathbf{n}}$. The acoustic field of the fluid domain enclosed by the surface ($f < 0$) is assumed to be zero and replaced by a surface distribution of sources which restores the conservative character of the field. The acoustic effect of these sources on the outer field is equivalent to that of the moving body.
This is achieved through the formalism based on generalized functions such as the Dirac $\delta(f)$ and Heaviside step function $H(f)$. Applying the generalized functions to the continuity and momentum equation:

$$H(f)\left[\frac{\partial \rho}{\partial t} + \frac{\partial}{\partial x_i}\left(\rho u_i\right)\right] = 0 \tag{2.55}$$

$$H(f)\left[\frac{\partial}{\partial t}\left(\rho u_i\right)+\frac{\partial}{\partial x_j}\left(\rho u_i u_j-\sigma_{ij}\right)\right]=0 \tag{2.56}$$

yields to:

$$\frac{\partial}{\partial t}\left[\left(\rho-\rho_0\right)H(f)\right]+\frac{\partial}{\partial x_i}\left[\rho u_i H(f)\right]=Q_m\delta(f) \tag{2.57}$$

where $Q_m\delta(f)$ is a source term localized on the surface (the $\delta(f)$ function defines it as null everywhere except on the surface) which can be interpreted as a distribution of mass sources. And

$$\frac{\partial}{\partial t}\left[\rho u_i H(f)\right]+\frac{\partial}{\partial x_j}\left[\left(\rho u_i u_j-\sigma_{ij}-p_0\delta_{ij}\right)H(f)\right]=F_i\delta(f) \tag{2.58}$$

whereF_i in the momentum equation represents a surface distribution of forces. The presence of the Heaviside function $H(f)$ on the left-hand side in terms of equations 2.57 and 2.58 restore the quiescent conditions inside the integration surface. The two equations are now rearranged into an inhomogeneous wave equation following the same approach used for the derivation of Lighthill's analogy, leading to the FW-H equation:

$$\begin{aligned}\frac{\partial^2}{\partial t^2}\left[\rho' H(f)\right]-c_0^2\frac{\partial^2}{\partial x_i\partial x_i}\left[\rho' H(f)\right]=\\ =\frac{\partial}{\partial t}\left(Q_m\delta(f)\right)-\frac{\partial}{\partial x_i}\left(F_i\delta(f)\right)+\frac{\partial^2}{\partial x_i\partial x_j}\left(T_{ij}H(f)\right)\end{aligned} \tag{2.59}$$

where:

$$T_{ij}=\rho u_i u_j-\tau_{ij}+\left(p'-c_0^2\rho'\delta_{ij}\right)$$

The source term on the right-hand-side of the FWH equation consists of three terms. Pressure fluctuations which characterize the flow outside the surface S are equivalent to the ones associated with an equivalent quiescent acoustic medium forced by the three source terms. The first two terms are surface distribution sources (denoted by the Dirac function δ_{ij}) which have a mathematical form of a *Monopole* and *Dipole*. The third term has instead the shape of a *Quadrupole* source term. Moreover, due to the presence of the Heaviside's function $H(f)$ this is a volume distribution of sources.
When we consider the function f to be $f>0$ everywhere, the FWH equation reduces to the Lighthill's equation as the surface S vanish ($\delta(f)=0$ and $H(f)=1$).

To better define the physical meaning of the three sources, we consider the case where the surface S coincides with the surface of the analyzed body (i.e. an impenetrable surface):

- $\mathbf{Q_m}\delta(\mathbf{f})$: Represents the fluid displacement generated by the movement of the body
- $\mathbf{F_i}\delta(\mathbf{f})$: Represents the unsteady loading applied on the body by the surrounding fluid
- $\mathbf{T_{ij}H}(\mathbf{f})$: The Quadrupole term accounts for all the physical sources and non-linear effects (turbulence, vorticity, shocks etc.) found in the fluid outside the integration surface S.

Chapter 3

Literature review

With the aim to gradually reduce the environmental footprint generated by air transport over the next few decades, the world's leading aviation organisations have in recent years drawn up challenging targets relating in particular to the reduction of aircraft noise and pollutant gases. This, together with the exponential growth of the UAM sector, has made it essential to find new propulsion systems capable of meeting the ambitious targets and the new operating environment of next-generation air transport. Electric and distributed propeller systems seem to be the current trend among eVTOL and novel aircraft design manufacturers, while only a few have identified ducted propeller systems as a possible solution [4].
Electric ducted fans represent a promising alternative for several reasons. In this section, a detailed analysis of the main aerodynamic effects and consequent variations in the performance of a ducted fan will be presented, comparing the benefits that this system brings compared to a non-ducted propeller. The main aeroacoustics qualities of ducted fans and the properties of an over-the-wing configuration are also presented. This information has been obtained through in-depth bibliographic research that allowed us to outline the main characteristics of this propulsion system in light of which both the ducted fan design and the analysis conditions have been chosen.

3.1 Ducted fan, aerodynamic and performance

Ducted fan consists of a propeller inserted into an annular duct with airfoil-like section which can be either symmetric with respect to the rotation axis or asymmetric. It can be considered as a hybrid between a propeller and a turbofan engine, where the turbofan is nothing more than a ducted fan driven by a turbojet engine. The presence of the duct results in a higher static thrust/power ratio for a given

diameter if compared to the same propeller in a free configuration. This is the result of the combined effect of suction on the diffusion of the propeller jetstream effect has been confirmed by several studies [15, 16]. This is true both in the case of a simple propeller positioned inside a duct and even more so in the case of an optimised fan.
It is important to emphasise a fundamental concept, in ducted fans the shape of the blades used is different from those of a typical open propeller as they must be designed taking into account the interaction between the rotor and the internal surface of the duct.

(a) Bell X22

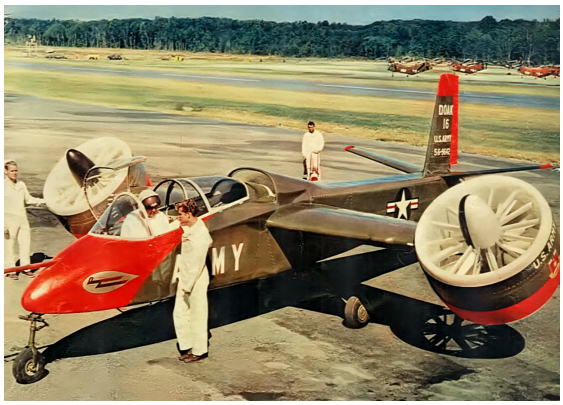

(b) Doak VZ-4

Figure 3.1: NASA tilt-rotor concept.

Interest in this type of propulsion system is not new. Several analyses of ducted propeller concepts can be traced back to the 1960s and 1970s, a period during which NASA conducted extensive theoretical and experimental research on this type of system in parallel with the development of two tilt-rotor prototypes the Bell X22 and the Doak VZ4D [17] (Figure 3.1). More recently, however, new studies have focused mainly on the application of this system to Unmanned Aerial vehicles

(UAV) at low Reynolds number regimes and high RPM configurations [8, 18, 19, 20, 21, 22]. The conditions under which these concepts have been analysed, however, do not seem to be suitable for high-speed flight conditions, for which the Reynolds numbers relative to the working conditions are higher, as well as the compressible effects acquire high importance. These analyses, however, allow understanding the main aerodynamic phenomena and behaviours of the flow inside and outside ducted fans. They are also a good starting point for understanding the phenomena we expect to occur.
The introduction of advanced numerical analysis and high fidelity computational fluid-dynamic (CFD) simulations have enabled in-depth aerodynamic analyses that are difficult to perform in the experimental field due to the complex geometry. However, much of the research currently available on the subject lacks references to the geometries used (often for reasons of industrial confidentiality), making them difficult to replicate. In addition, many numerical analyses lack experimental validation, often making the results unreliable.

Concerning the effects on aerodynamic phenomena, the presence of the duct leads to a reduction in the size of the tip vortex that is created at the blade tip due to the pressure difference between the two sides of the blade [21, 22]. In

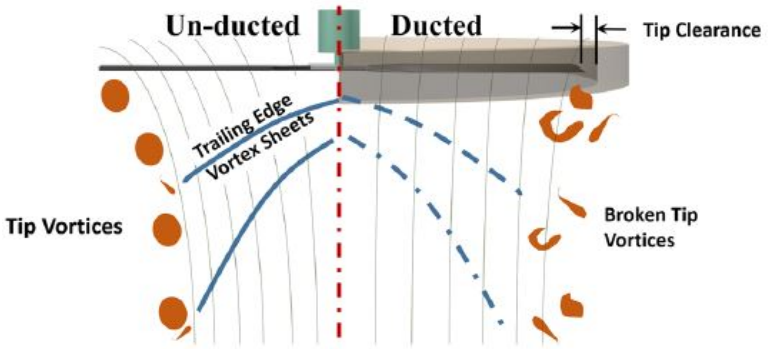

Figure 3.2: Duct effect on the tip-vortex [22].

general, the tip vortex size decreases as the tip clearance decrease. Tip clearance refers to the distance between the duct surface and the blade and it is usually represented as a percentage of the blade length. It has been confirmed that a smaller tip clearance increases the thrust generated by the ducted fan, inducing a greater pressure difference across the disk [8, 23]. Moreover, reducing the size of the tip-vortex leads to an overall reduction in aerodynamic losses due to turbulent interaction between the main tip vortex itself, the secondary vertices and the wake of each blade.

In the case of an open propeller, once formed behind the blade, the tip vortex generated at each blade pass follow a helical path that moves downstream interacting with the other turbulent structures resulting from blades wakes (Figure 3.3a).

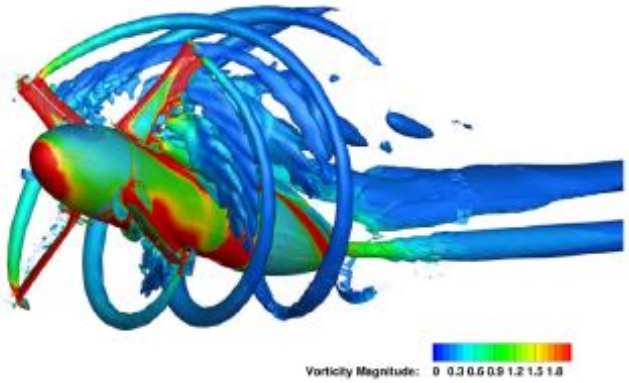

(a) Free propeller helical wake

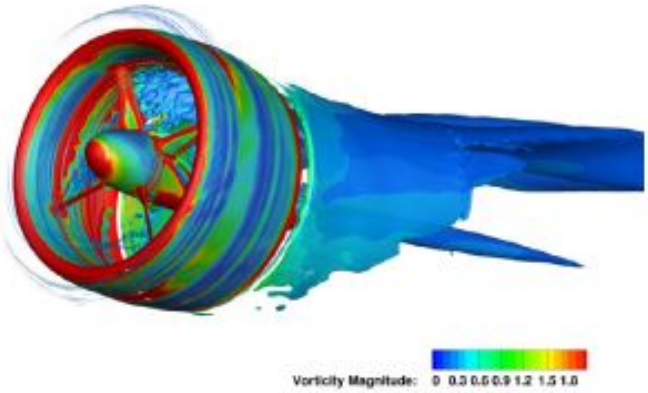

(b) Ducted propeller wake

Figure 3.3: Difference between ducted and un-ducted propeller wake [24].

Conversely, when the blade rotates closer to a surface the tip vortex path change as well as the flow field behind the rotor. As outlined by Reynard [23] due to the strong pressure jump across the propeller disk the slipstream contracts moving the vortex away from the surface, then the slipstream contraction rapidly diminishes downstream moving downwards the turbulent structure. At a certain distance behind the propeller disk, the vortex filament starts to interact with the surface of the duct, the lower convective velocity near the wall deforms the filament resulting in a change of the filament's shape. Although this analysis has been carried out for a propeller placed on top of a finite wing (to simulate an over-the-wing configuration) and not for a ducted fan, it can be expected that these phenomena can also

occur when the interaction between rotor and surface is continued along the whole diameter of the duct. This complex phenomenology can therefore result in flow separation.

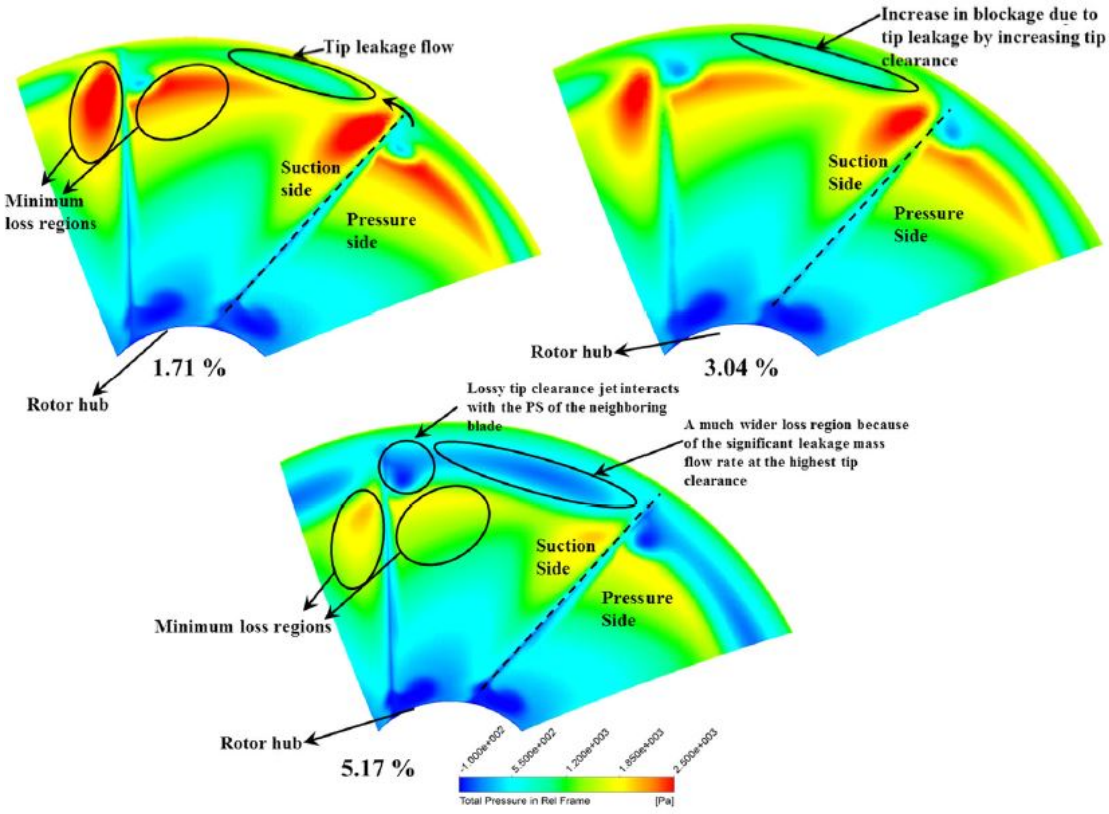

Figure 3.4: Relative total pressure comparison at the rotor exit plane for the baseline blades with 1.71%, 3.04%, and 5.17% tip clearances [8].

When the tip clearance increases, aerodynamic loss due to the tip leakages rise resulting in intensification in the blockage effect due to the tip vortex. In addition, the larger interaction of the tip vortex with the pressure side of the rotor blade causes the total pressure to drop in the passage. Ataturk and Camci [8] proved this effect in their analysis. By reducing the tip clearance of a 559mm ducted fan from 3.04% to 1.71% the hover efficiency of the engine increased by 17.85% at higher rotor speeds. On the other hand, when the tip clearance is increased from 3.04% to 5.17%, up to an 18.1% drop in hover efficiency was observed. Figure 3.4 provides a clear representation of the phenomenon by showing how the fluid dynamic field changes in the region around the blades when the tip clearance is modified. From the figure is also possible to identify a region where losses are unaffected by tip clearance variation. The area is located near the rotor hub, here the combination

between hub corner separation and three-dimensional hub end-wall flow produces a re-circulation zone. The overall swirl component of the flow (which leads to turbulent interactions and therefore losses), however, can be reduced by designing proper stator vanes. These benefits the engine performance and noise emission. Also, the use of stator vanes could reduce engine power requirements. This is not possible in an open rotor configuration.
In general, ducted fan design is very challenging and must be developed based on aircraft mission. Duct lip geometry has been proven to be a critical part of the overall design of a ducted fan together with the aspect ratio of the duct. While the choice of the aspect ratio is limited by the adverse pressure gradient, which may lead to flow separation inside the diffuser, the geometry of the duct lip affects the proprieties of the incoming flow affecting the lip suction effect and altering the location of the pressure centre [20]. For an eVTOL equipped with an OTW ducted fan, the optimal design point is the cruise condition, if we consider the length of a UAM or RAM mission the longest phase is the cruise one during which the distributed ducted fan system should provide the minimum aerodynamic drag. For this reason, the design of the duct and its lip have a strong impact on the flight performance of an eVTOL.

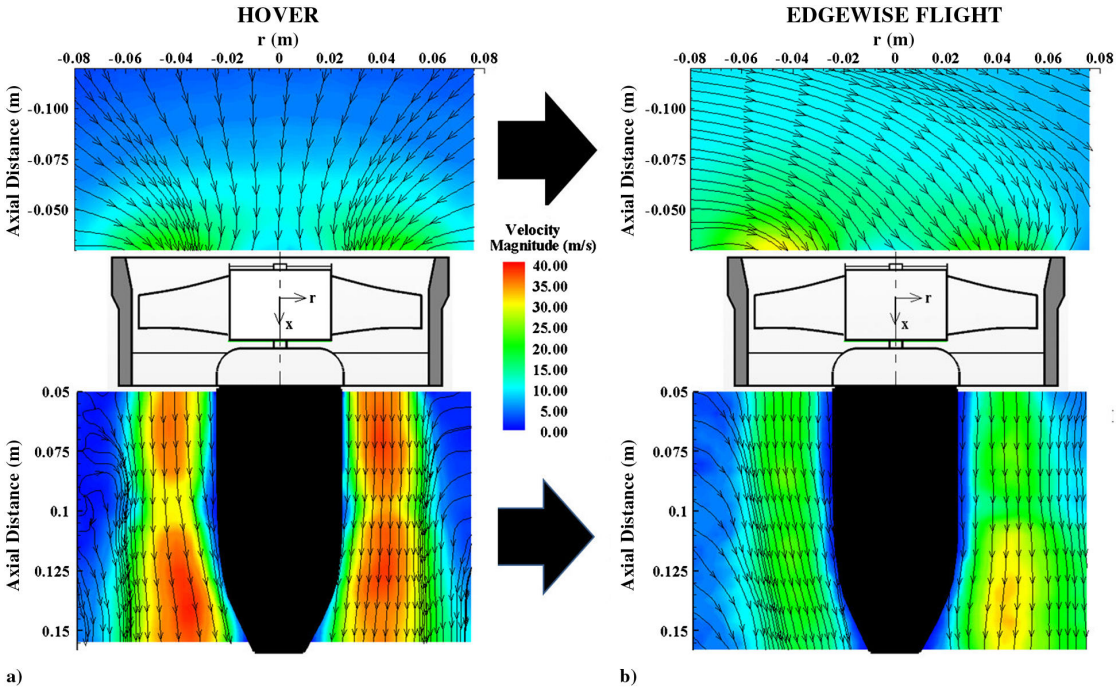

Figure 3.5: Streamlines at the inlet and exit pf a ducted fan for a) hover and b) edgewise flight (PIV measurements) [18].

Bontempo [16] shows that the Advance Ratio of the fan (which is related to the speed of rotation of the rotor and the free stream speed) influence the shape of the incoming streamlines and could determine the separation of the flow entering the thruster during hover and crosswind conditions. Also, at low RPM settings flow separation can occur due to the blockage effect of the ducted fan overcoming the positive suction, high RPM settings of the rotor increase the magnitude of the velocity in both inlet and exit region as expected from the increased fan pressure ratio [18].
While in the forward flight the nacelle has a negative contribution to the aerodynamic drag, during the hover phase the duct is found contributing to the total thrust generated by the system [15, 24].
In off-design conditions such as edgewise flight, however, the geometric characteristics and thrust settings of the engine greatly influence the aerodynamic field and thus the performance. The breathing area of the fan rotor is reduced in edgewise flight because of the flow streamline distortion (Figure 3.5), the maximum velocity magnitude is shifted toward the hub when a separation bubble is formed at the leading-edge lip while in normal hover conditions the max value is located in the middle of the duct. At the same time, the streamlines at the trailing edge of the inlet plane are more normal to the fan inlet plane, as a result, this side sees a slightly higher mass flow rate than the leading side affecting the direction and magnitude of the exit jet. This effect is reduced by the increased rotational speed of the fan [18]. In summary, non-axial inflow results in not only distortion of streamlines and strong forces and moment on the duct but also imbalanced disk loading which can cause more severe problems like vibration and thus increase in noise generation.

3.2 Ducted fan aeroacosutic

During past decades, research into the noise emission of fans surrounded by a finite/infinite/semi-infinite duct has attracted great interest, particularly in the areas of turbofan/turbomachinery but also in wind power applications. The aerodynamic of a ducted fan is very complex. The noise emission of this architecture strongly depends on the flight conditions, engine settings, the interaction of the fluid with the structure and on the aerodynamic phenomena occurring in the flow. Concerning UAM and RAM applications,the noise level signature of eVTOL's propulsion system must be kept at low levels in order to maintain a high comfort threshold for both passengers and ground staff as well as not to be a source of discomfort for the urban environment. Ducted fans can enable this key requirement giving market access to inner-city operations. The presence of the duct has a significant positive impact on sound emission and the resulting sound field of a

rotating fan/propeller.
While in an open propeller the noise spreads uniformly in all directions (Figure 3.6),

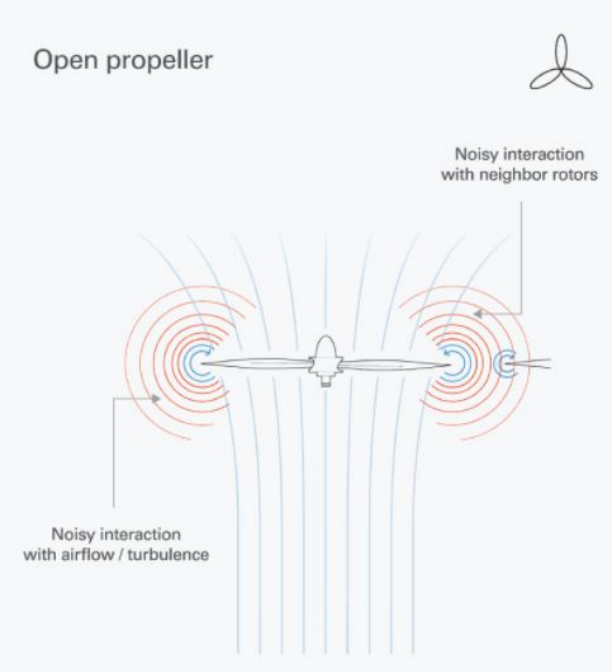

Figure 3.6: Sound radiation of open rotors [25].

in a ducted fan the duct act like a shield reducing the noise emission and altering the acoustic patterns and directivities (Figure 3.7). This behaviour has been verified by several studies both numerical and experimental [26, 27, 28], changes in the noise radiation are not only caused by the duct itself but also by the variation of the propeller noise if compared with the same in an open rotor configuration. This is strictly related to the different flow field of the two propulsion systems. Moreover, the duct provides a platform on which acoustic liners can be installed, further reducing the overall perceived noise level.

The acoustic field of a ducted fan consists of two main acoustic signatures:

- A tonal or harmonic noise generally caused by sources that repeat themselves exactly during each rotation, in this case by the rotor blade passing.
- A broadband noise which is a random, non-periodic signal caused by turbulent aerodynamic fluctuations.

The german-based manufacturer Lilium has demonstrated that it is possible to obtain a propulsion system based on ducted fans with a limited noise impact.

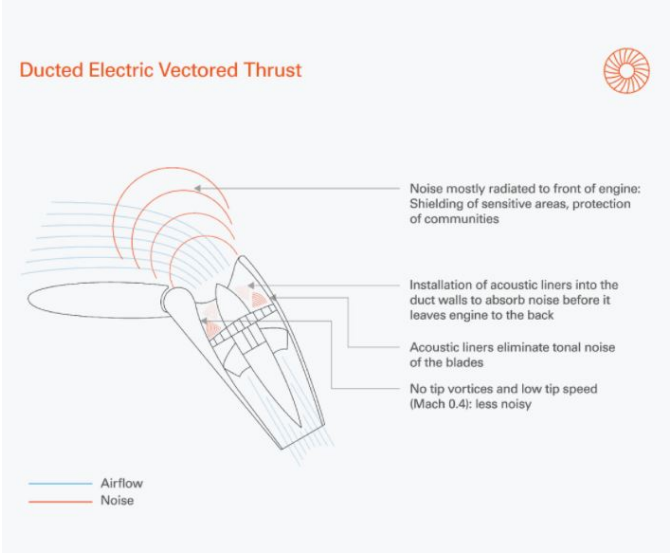

Figure 3.7: Sound radiation of a ducted fans [25].

In particular, they claim that Lilium jet will be virtually inaudible during cruise flight while during near ground operation such as hovering for take-off and landing the aircraft overall sound pressure level (OSPL) is 60dB at 100m [4]. Reducing the noise emitted by a ducted fan can be achieved through the use of acoustic liners placed on the inner duct of the ducted fan and by improving the design of the rotor and stator components of the engine to minimize turbulent effects and vibration.

In general, it can therefore be stated that those factors which boost the aerodynamic performance also reduce the noise emissions such as reduced tip clearance and avoiding flow separation [29]. As displayed in Figure 3.8 the acoustics generation and propagation of a free propeller (Figure 3.8a) and ducted fan (Figure 3.8b) are shown in a clear way. Noise components from the tip vortices and aerodynamic interactions of the ducted propeller contribute in a small way compared to the high pressure fluctuations generated by the free propeller tip vortices.
Finally, it is important to note that the analysis of a free propeller does not provide relevant information for the investigation of the acoustic field of the same propeller in a duct. This happens because the acoustic field changes drastically when the duct is introduced [28].

3.3 Over-the-wing configuration

While most research has focused on comparing ducted fan with propellers in an isolated configuration, the analysis of the effect determined by the coupling of this

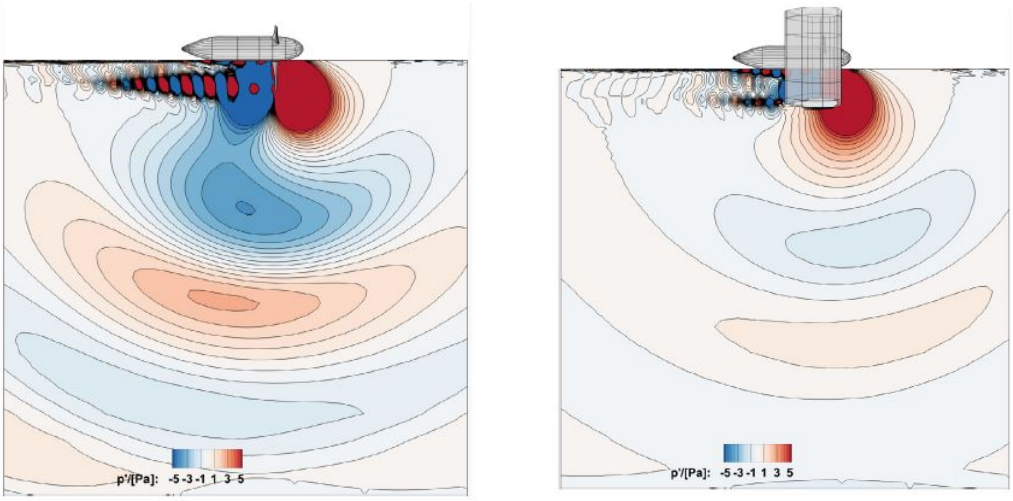

(a) Free propeller aeroacoustic field **(b)** Ducted propeller aeroacoustic field

Figure 3.8: Instantaneous sound pressure contours for a free propeller vs equivalent ducted [24].

propulsion system and the wings is a topic that has rarely been discussed in the literature. A distributed over-the-wing configuration can, at least in theory, bring benefits both in terms of the thrust performance of the overall aircraft and in terms of energy consumption. However, the extra weight that the duct brings must not be neglected.
The installation of the ducted fan over an aerodynamic surface firstly leads to a considerable change in the surface pressure field as reported in many research [23, 30, 31]. The strong static-pressure jump generated across the propeller/fan disk leads to a decrease in pressure on the wall upstream of the disk and an increase in pressure downstream of it as shown in Figure 3.9. The magnitude of these peaks is strongly correlated to the thrust settings of the engine, in particular, the higher the thrust setting is the higher the negative and positive peaks are. On the other hand, at low throttles, the blockage effect of the nacelle is dominant, the flow is slowed and the static pressure rises [31]. Other factors like the tip-clearance and blade pitch affect the intensity of the pressure jump across the rotor disk [23]. Moreover, the variation in pressure distribution on the wing results in a corresponding increase in the aerodynamic performance of the wing.
By increasing the flow speed on the upper surface of the wing the total lift generated by the wing is improved, in addition, the drag generated by the duct is reduced if the rotor is placed at the point of maximum thickness of the wing airfoil [30, 32]. The pressure jump across the disk discussed previously, also leads to an extra

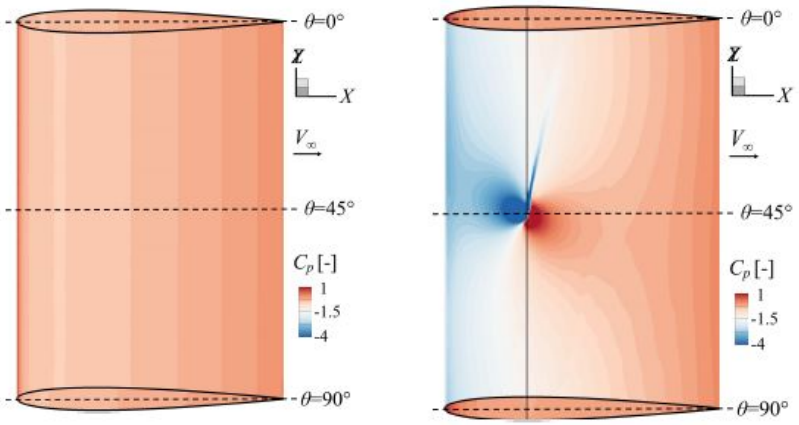

(a) Cp distribution in unistalled case

(b) Cp distribution in installed case

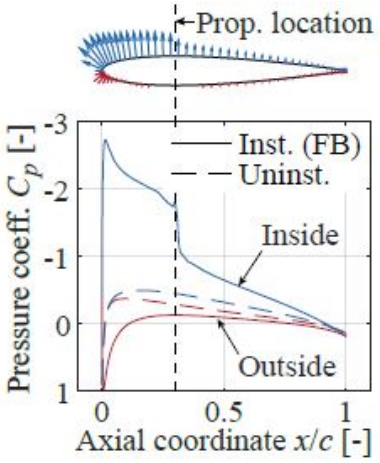

(c) Cp distribution in installed case

Figure 3.9: Pressure coefficient contours on the duct's inner surface and wing for the unistalled (a) and installed (b) cases, average Cp on wing section comparison (c) [30].

net-axial force which increases the duct thrust [30]. A graphic example of this effect is given in Figure 3.9c.
These results derive from preliminary analyses in which the ducted fan or propeller was simply placed on the wing without modifying either the geometry of the duct itself or that of the wing airfoil. The interaction between the boundary layer and the rotor blades is another interesting phenomenon that can influence the properties of the flow processed by the thruster, especially if the architecture involves an optimised installation where the upper part of the wing also acts as a duct for the

ducted fan. In these cases, it is possible to consider the flow behaviour similar to what happens in Boundary Layer Ingestion (BLI) propulsive configurations.
First of all, a BLI-like configuration reduces the wetted area of the engine nacelle, leading to a reduction in the aircraft's total shape drag (if we compare the same geometry but with the thrusters located away from the wing). Furthermore, by ingesting the boundary layer the low-velocity air in it does not mix out downstream in the wing's wake and instead is re-energized in the ducted fan resulting in a reduction of the wake dissipation [33]. Nevertheless, the thickness of the boundary layer is influenced by the installation of the propulsive system and in particular by the pressure gradient it induces on the wing. When the blockage effect of the fan nacelle is dominant the adverse pressure gradients induces boundary layer growth, while when a favourable gradient is present the growth of the boundary layer is slowed down and in some cases may even be reversed [31]. Variation of the angle of attack (AOA), similarly, affects the size of the boundary layer and thus the performance of the thruster.
Although this configuration seems to bring great advantages, the lack of research and data on the most important phenomena characterising the interaction between ducted fan and wing does not allow to verify whether these benefits are real.

Chapter 4

Methodology

The purpose of this chapter is to provide the reader with the necessary basis for understanding the methodologies used to conduct the CFD and CAA analyses of this thesis. The LBM solver PowerFLOW® by Dassault Systèmes has been used to investigate the fluid dynamic and aeroacoustic field of the configuration.
In Section 4.1 and Section 4.2 the fundamentals of the lattice Boltzmann method (LBM) are discussed: in Section 4.1 the Boltzmann equation on which LBM is based is introduced while in Section 4.2 describe the LBM method.
Section 4.3 shows how the LBM is implemented in Dassault Systèmes PowerFLOW®.
The methodology behind the aeroacoustics analyses is discussed in section 4.4 where, in particular, the method used to obtain the aeroacoustic data is described and thus how it is implemented in the solver.

4.1 The Boltzmann Equation

When we talk about describing fluid dynamics, the first thing that comes to mind is the equations of Naiver-Stokes which describe the fluid at a fully-continuum level through the use of macroscopic quantities such as density, pressure and velocity. This is not the only way to describe the behaviours of a fluid, fluids can also be described on a microscopic and mesoscopic level. In the first case, the activity of particles at a molecular level can be described by tracking every single molecule in gas and determining how they collide with each other. This process is obviously impossible because of the infinite number of particles and the lack of information on the initial state. Instead of attempting a full description of the fluid, is possible to attempt a mesoscopic description of it employing particle density distribution function. In this way we obtain a statistical description of the behaviours of the particles [34].

We then consider a particle distribution function $f(\boldsymbol{\xi}, \boldsymbol{x}, t)$ which describe the density of particles at a time t, at point x having speed ξ. This can also be seen as a probability function of finding particles with speed ξ near the point x at time t. The distribution function f allows to obtain a macroscopic description of the fluid, local density ρ, momentum density $\rho\boldsymbol{u}$ and total energy ρE of the fluid can be found as zeroth-, first- and second-order moments of the distribution function respectively [35]. Moments con be found by weighting $f(\boldsymbol{\xi}, \boldsymbol{x}, t)$ with some function of ξ and integrating over the entire velocity space:

$$\rho(\boldsymbol{x}, t) = \int f(\boldsymbol{x}, \boldsymbol{\xi}, t)\, d^3\xi \tag{4.1}$$

$$\rho(\boldsymbol{x}, t)u(\boldsymbol{x}, t) = \int \boldsymbol{\xi}\, f(\boldsymbol{x}, \boldsymbol{\xi}, t)\, d^3\xi \tag{4.2}$$

$$\rho(\boldsymbol{x}, t)E(\boldsymbol{x}, t) = \frac{1}{2}\int |\boldsymbol{\xi}|^2\, f(\boldsymbol{x}, \boldsymbol{\xi}, t)\, d^3\xi \tag{4.3}$$

We now know that the distribution of particles can be defined by the function f but we don't know how the particles evolve in time. By deriving the evolution of this function in time we obtain the Boltzmann equation which offers a mathematical description of the particle distribution function $f(\boldsymbol{x}, \boldsymbol{\xi}, t)$ of the particles at $(\boldsymbol{x}, \boldsymbol{\xi})$ in space and at time t.
The general Boltzmann equation reads:

$$\frac{Df}{Dt} = \left(\frac{\partial f}{\partial t}\right)_{coll.} \tag{4.4}$$

By developing the total differential with respect to time t we obtain the Boltzmann-Equation [35]:

$$\frac{\partial f}{\partial t} + \boldsymbol{\xi}\,\frac{\partial f}{\partial \boldsymbol{x}} + \frac{\boldsymbol{F}}{\rho}\,\frac{\partial f}{\partial \boldsymbol{\xi}} = \Omega(f) \tag{4.5}$$

In the equation, the left side represents the transport of particles and the influence of external forces on their behaviour while on the right side of the equation there is the *collision operator* $\Omega(f) = \left(\frac{\partial f}{\partial t}\right)_{coll.}$. It describes the variation of f that occurs after the interaction between the particles, thus governing the evolution of the fluid towards thermodynamic equilibrium.

Analyzing in detail the different terms that appear on the left side of the equation:

- $\frac{\partial f}{\partial t}$ represents the evolution of the function $f(\boldsymbol{x}, \boldsymbol{\xi}, t)$ through time.
- $\boldsymbol{\xi} \frac{\partial f}{\partial \boldsymbol{x}}$ represents the particles diffusion.
- $\boldsymbol{F} \frac{\partial f}{\partial \boldsymbol{\xi}}$ is a term that takes into account the effect that external forces have on the fluid.

If no collision occurs, the speed ξ of each particle will remain constant in time. The presence of collisions between particles however brings an additional source term that indicates the rate of change of f due to the collision-related changes in particle direction.

4.1.1 Collision operator

When two particles collide their velocity is altered. The new condition depends on their pre-collision location as well as the forces acting during the collision itself. However, is possible to assume that the collision spread particles' velocities in all directions around their mean velocity. Hence a physical system that is out of equilibrium tries to achieve a condition in which it can be considered in equilibrium. This process that occurs after the collision of two particles is also known as a relaxation process.
The *collision operator* can have different forms, however, three quantities are always conserved in a collision between particles in a monatomic gas: mass, momentum and transnational energy. The conservation equations of these quantities are presented below:

$$\textbf{Mass conservation:} \quad \int \Omega(f)\, d^3\xi = 0 \tag{4.6}$$

$$\textbf{Momentum conservation:} \quad \int \boldsymbol{\xi}\, \Omega(f)\, d^3\xi = 0 \tag{4.7}$$

$$\textbf{Total Energy conservation:} \quad \int \frac{|\boldsymbol{\xi}|^2}{2}\, \Omega(f)\, d^3\xi = 0 \tag{4.8}$$

The original *Boltzmann collision operator* is a very complex double integral over velocity space, it models the interaction between two particles with high detail. Because of the complexity of the original collision operator other models have been proposed. *Bathgnar, Gross and Krook* developed a collision operator that is relatively simple but still satisfies the conservation of mass, momentum and energy. The *BGK* collision operator expressed in 4.9 is widely used today [35].

$$\Omega(f) = -\frac{1}{\tau}(f - f^{eq}) \tag{4.9}$$

As introduced before, the distribution of particles tends to reach a state of equilibrium f^{eq} by a relaxation process. The *BGK* collision operator does not attempt to follow the collision in detail but rather captures the relaxation process by directly modelling it. In the equation the term τ represents the relaxation time, it has to be in the same order as the collision time while the term f^{eq} refers to the equilibrium distribution function. The Boltzmann equation with the BGK collision operator also known as the Boltzmann-BGK equation written as:

$$\frac{\partial f}{\partial t} + \boldsymbol{\xi}\,\frac{\partial f}{\partial \boldsymbol{x}} + \frac{\boldsymbol{F}}{\rho}\,\frac{\partial f}{\partial \boldsymbol{\xi}} = -\frac{1}{\tau}(f - f^{eq}) \tag{4.10}$$

To complete the discussion, the Maxwell-Boltzmann Equilibrium Distribution equilibrium equation is introduced in the following Subsection.

4.1.2 The Maxwell-Boltzmann Equilibrium Distribution

The local equilibrium distribution function is written as follows [35]:

$$f^{eq}(\boldsymbol{x}, \boldsymbol{\xi}, t) \;=\; \rho \left(\frac{m}{2\pi k_b T}\right)^{\frac{D}{2}} \cdot \exp\left(-\frac{m|\boldsymbol{v}|^2}{2k_b T}\right) \tag{4.11}$$

here the relative velocity $\boldsymbol{v}$ has been introduced, it represents the deviation of the particle velocity from the local mean velocity:

$$\boldsymbol{v}(\boldsymbol{x}, t) = \boldsymbol{\xi}(\boldsymbol{x}, t) - \boldsymbol{u}(\boldsymbol{x}, t) \tag{4.12}$$

This function is valid when we consider a fluid that has the same density and viscosity at each point and each time. The term ρ represents the macroscopic density, it can also be seen as the zeroth-order moment tensor of the equilibrium function:

$$\rho = \int f^{eq} d\xi$$

In the equation also appear the Boltzmann constant k_b, the spatial dimension D (which is $D = 3$ in the 3D case), the temperature T, the microscopic velocity $\boldsymbol{\xi}$ and the macroscopic velocity $\boldsymbol{u}$. Note, in equation 4.11 the macroscopic velocity is considered to be non-zero. If $\boldsymbol{u} = 0$ we switch to the absolute equilibrium distribution equation:

$$f^{eq}(\boldsymbol{x}, \boldsymbol{\xi}, t) \;=\; \rho \left(\frac{m}{2\pi k_b T}\right)^{\frac{D}{2}} \cdot \exp\left(-\frac{m\boldsymbol{\xi}^2}{2k_b T}\right) \tag{4.13}$$

4.2 Lattice Boltzmann Model (LBM)

The Lattice Boltzmann Method, which originates from the Lattice-Gas-Automata (LGA), is a discrete approach to solving the Boltzmann Equation. The fundamental idea of the LBM is to construct simplified kinetic models that incorporate the essential physics of microscopic or mesoscopic processes so that the macroscopic averaged properties obey the desired macroscopic equations [34].
This method is based on the Boltzmann-BGK equation 4.10 which components are defined in the continuum phase space. Unlike most transport equations that are discretized in the physical space and time, the Boltzmann equation's main variable f is a function of coordinates in physical space, velocity space, and time. Therefore, to get the LBM is necessary to discretize it into two different steps. First, the continuous space of velocities $\boldsymbol{\xi}$ is discretized to a finite set of ξ_i to reduce the continuum velocity space to only a certain number of discrete velocities. This first passage is obtained through a method based on the Hermite polynomials and Gauss-Hermite quadrature. The function f_i obtained after the fist step is similar to the distribution function introduced in 4.1, it represents the density of particles with velocity $\boldsymbol{c_i} = (c_{ix}, c_{iy}, c_{iz})$ at position $\boldsymbol{x}$ and time t.
Second, an additional discretization simultaneously in physical space and time of the discrete-velocity Boltzmann equation by means of the Characteristic Method. In the following, the discussion of the steps necessary to obtain the Lattice-Boltzmann-BKG equation is simplified. For a more comprehensive discussion, the reader can refer to [35].

Starting from the Boltzmann equation we introduce a finite set of velocities to obtain the discrete-velocity Boltzmann equation, moreover, to simplify the discussion the external force term $\frac{\boldsymbol{F}}{\rho}\frac{\partial f}{\partial \boldsymbol{\xi}}$ is omitted.

$$\frac{\partial f_i}{\partial t} + \boldsymbol{c_i}\frac{\partial f_i}{\partial \boldsymbol{x}} = \Omega_i \tag{4.14}$$

The equation is then integrated over a time Δt and space Δx interval, we obtain:

$$\frac{f_i(\boldsymbol{x}, t+\Delta t) - f_i(\boldsymbol{x}, t)}{\Delta x} + \boldsymbol{c}_i\frac{f_i(\boldsymbol{x}+\Delta x, t+\Delta t) - f_i(\boldsymbol{x}, t+\Delta t)}{\Delta t} = \Omega_i \tag{4.15}$$

To get an explicit equation a lattice size of $\Delta x = 1$ is chosen. In this way the term $\frac{\Delta x}{\Delta t}$ can be replaced by a lattice speed $c = 1$ over a a time step $\Delta t = 1$. Both Δx and Δt are defined in the *lattice units*, is possible to convert quantities between lattice units and physical units. With this definition the terms $\frac{f_i(\boldsymbol{x},t+\Delta t)}{\Delta t}$ cancel each other.

This leads to:

$$\frac{f_i(\boldsymbol{x} + \Delta x, t + \Delta t) - f_i(\boldsymbol{x}, t)}{\Delta t} = \Omega_i \tag{4.16}$$

In order to use the *BGK collision operator* described in 4.9 it also has to be discretized by introducing a finite set of velocities as done for the left-hand side of the equation:

$$\Omega_i = -\frac{1}{\tau}(f_i - f_i^{eq}) \tag{4.17}$$

The *Lattice-Boltzmann BGK equation* is written as follows:

$$f_i(\boldsymbol{x} + \boldsymbol{c_i}\Delta t, t + \Delta t) - f_i(t, \boldsymbol{x}) = -\frac{\Delta t}{\tau}(f_i - f_i^{eq}) \tag{4.18}$$

where $\frac{\Delta t}{\tau}$ is the collision frequency and i denotes each possible direction of the particle. The equation expresses that the particle $f_i(\boldsymbol{x}, t)$ move with velocity c_i to a nearby point $x + c_i\Delta t$ at the next time step $t + \Delta t$.
As already discussed the τ on the right-hand side of the equation represents the relaxation time. In addition to defining a time scale within which the function f_i returns to the equilibrium condition f_i^{eq}, it is also related to the kinematic viscosity ν which is a relevant physical quantity in the simulation [35]:

$$\nu = c_s^2 \left(\tau - \frac{\Delta t}{2}\right) \tag{4.19}$$

Here c_s is the *sound speed* which in general is defined as:

$$c_s^2 = \left(\frac{\partial p}{\partial \rho}\right)_s \tag{4.20}$$

In the basic isothermal LBE c_s defines the relation between pressure p and density ρ ($p = c_s^2\rho$) and represents the numerical speed of sound used in this LBM model. The equilibrium distribution function for the Lattice Boltzmann method is obtained by performing a Taylor series expansion to the 2nd order of Equation 4.11 with respect to the velocity:

$$f^{eq}(u) \simeq f^{eq}(0) + f^{eq}(0)(u) + \frac{f^{eq}(u)^2}{2} + O^2 \tag{4.21}$$

which can also be seen as [36]:

$$f_i^{eq} = \rho W_i \left(1 + A(\boldsymbol{u} \cdot \boldsymbol{c}_i) + B(\boldsymbol{u} \cdot \boldsymbol{c}_i)^2 + C(\boldsymbol{u} \cdot \boldsymbol{u})\right) \tag{4.22}$$

where A, B and C are Lattice-constants and W_i is a weighting factor. These constants can be obtained from a quadrature procedure and are specific to the chosen velocity set.
For each set of velocities, the *speed of sound* is written as follows:

$$c_s^2 = \frac{1}{3}\frac{\Delta x^2}{\Delta t^2} \tag{4.23}$$

While the velocity in the lattice unit can be defined as:

$$c = \frac{\Delta x}{\Delta t} \tag{4.24}$$

Summing up, the Boltzmann equation is simplified by the LBM by restricting the movements of the particles in a lattice made of discrete nodes. Velocity models are represented using the *DkQb* notation where k represents the dimensions and b represents the number of discrete velocity directions. Based on the dimension of the space in which we want to carry out the simulation, there are a variety of velocity sets and corresponding equilibrium distributions that are frequently used in the literature, in Figure 4.1 two cases are shown.

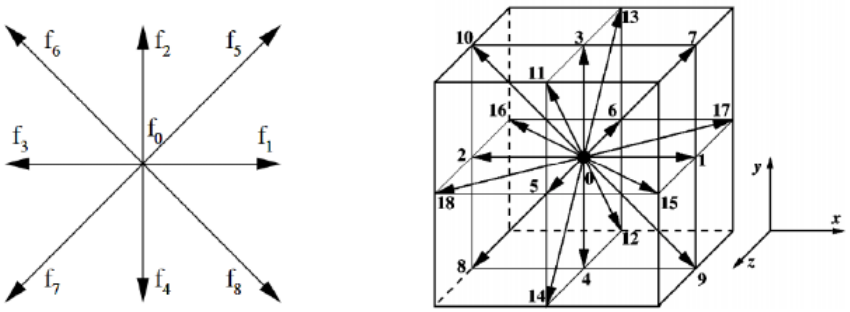

Figure 4.1: Lattice node in model D2Q9 (left) and in D3Q19 (right) [34]

For the D2Q9 model, the equilibrium distribution is written as follows:

$$f_i^{eq} = \rho W_i \left[1 + \frac{3\,\boldsymbol{c_i} \cdot \boldsymbol{u}}{c_s^2} + \frac{9(\boldsymbol{c_i} \cdot \boldsymbol{u})^2}{2c_s^4} - \frac{3\boldsymbol{u}^2}{2c_s^2}\right] \tag{4.25}$$

In the equilibrium distribution, W_i are the weight which depends on the set of velocities, c_i is the discrete microscopic velocity, u is the flow velocity and c is the lattice speed as already introduced previously. For models D2Q9 and D3Q19 the values of the weights are given below:

$$\textbf{D2Q9:} \qquad W_i = \begin{cases} 4/9 & i = 0 \\ 1/9 & i = 1,2,3,4 \\ 1/36 & i = 5,6,7,8 \end{cases} \tag{4.26}$$

$$\textbf{D3Q19:} \qquad W_i = \begin{cases} 1/3 & i = 0 \\ 1/18 & i = 1-6 \\ 1/36 & i = 7-18 \end{cases} \tag{4.27}$$

Macroscopic fluid proprieties such as density ρ and velocity u can be recovered from microscopic proprieties after solving Equation 4.18. In particular, considering the D2Q9 model, the *macroscopic fluid density* $\rho(\boldsymbol{x}, t)$can be defined as a sum of the distribution function of the microscopic particles:

$$\rho(\boldsymbol{x}, t) = \sum_{i=0}^{8} f_i \tag{4.28}$$

Therefore, the *macroscopic velocity* $\boldsymbol{u}(\boldsymbol{x}, t)$ can be defined as an average of microscopic velocities $\boldsymbol{c_i}$ weighted by the distribution functions f_i:

$$\boldsymbol{u}(\boldsymbol{x}, t) = \frac{1}{\rho} \sum_{i=0}^{8} f_i c_i \tag{4.29}$$

4.3 LBM implementation in the flow solver

The Lattice Boltzmann BKG equation can be divided into two different parts:

$$\underbrace{f_i(\boldsymbol{x} + \Delta x, t + \Delta t) - f_i(\boldsymbol{x}, t)}_{\text{Streaming}} = \underbrace{-\frac{1}{\tau}(f_i(\boldsymbol{x}, t) - f_i^{eq}(\boldsymbol{x}, t))}_{\text{Collision}} \tag{4.30}$$

which are computed separately. The order of executing the propagation and collision steps is arbitrary.
The algorithm for the LBM implementation can be summarized in the following steps [37] which are also shown in Figure 4.2, for simplicity we will refer to the D2Q9 model:

1. **Step a - Initialization**: Values of ρ, u, f_i and f_i^{eq} are initialized for the first time step of the simulation.

2. **Step b - Streaming**: After initialization, the streaming step is computed. The propagation directions are defined by the set of discrete velocities $\boldsymbol{c}_i$. The new value of the distribution function f_i^* is calculated using values from the previous time-step as follow:

$$f_i^*(\boldsymbol{x} + \boldsymbol{c_i}\Delta t, t + \Delta t) = f_i(\boldsymbol{x}, t)$$

   The length of the arrows in Figure 4.2 represents the probability of a particle moving in that direction.

3. Macroscopic ρ and $\boldsymbol{u}$ are computed from f_i^* using equations 4.28 and 4.29.

4. The new equilibrium function f_i^{eq} is computed from fluid density ρ and velocity u using Equation 4.25 (which depends on the chosen model).

5. **Step c - Collision**: the collision is processed, again the distribution function value is updated:

$$f_i' = f_i^* - \frac{1}{\tau}(f_i^* - f_i^{eq})$$

Then the process is repeated by calculating the macroscopic velocity and density from the updated function f_i', steps 2 to 5 are then repeated.

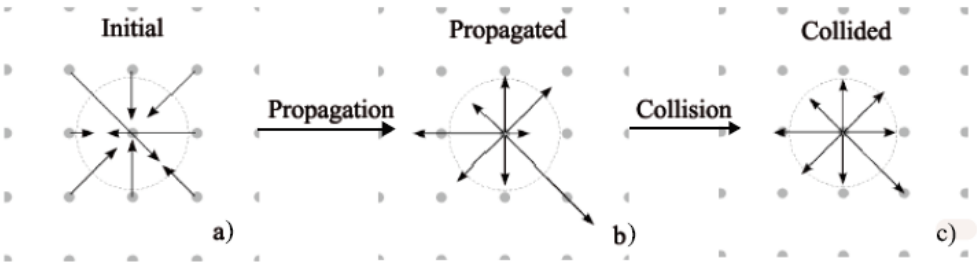

Figure 4.2: Overview of the steps through which the LBM is implemented

Boundary nodes are very tricky because here the boundary conditions (BCs) must be satisfied to represent closely the physical nature of the problem. During the *streaming* and *collision* step, as the distribution function $f_i(\boldsymbol{x}, t)$ is not defined at the boundaries, here the function has to be determined considering the constraints given by the macroscopic variables.

4.3.1 Boundary Conditions and wall modelling

The implementation of the boundary conditions (BCs) is a central step in any numerical problem. The stability and accuracy of the numerical solution strongly depend on BCs. In the case of the Lattice Boltzmann method, to reflect the macroscopic boundary conditions of the fluid two BCs types are widely used: *Bounce-Back* BCs and *Zou-He velocity and pressure* BCs.

The *Bounce-Back* is used to implement the no-slip conditions on the boundary and comes in a few variants. The basic idea behind this method is bouncing the particles back to the node of origin with reversed velocities as part of a particle reflection process. Pressure and friction (wall shear stress) forces are respectively represented by the variation of the perpendicular and tangential momentum components. In this way, the velocity at each surfel (wall) is set to zero ensuring a no-slip condition. There are two main configurations for this method: the on-grid and mid-grid bounce-back [37]. In the first case, the boundary is aligned with the lattice grid, the orientation of the boundary is thus not distinguished making this method ideal for simulating flow on complex geometries. However, this method has been verified to be only first-order accurate [37]. A way to improve the accuracy of the method is to use the mid-gird bounce-back configuration where the boundary is placed in the middle between fictitious nodes introduced by the method and boundary nodes of the fluid.

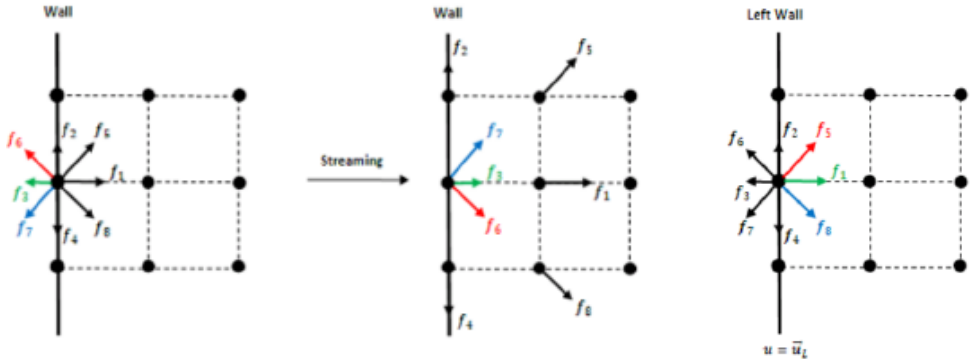

(a) Bounce Back Boundary condition on-grid implementation.

(b) Zou-He boundary condition.

Figure 4.3: Boundary conditions implemented in the LBM solver [37]

The *Zou-He* boundary condition is implemented when we're interested in defining a boundary region with prescribed velocity and pressure (density). With this implementation, some of the particle distributions are known while others are determined through a linear system using 4.28 and 4.29.
Considering the Cartesian mesh employed in the LBM solver, the resolution of the boundary layer turns out to be very hard because of the lack of the possibility of stretching the grid only in the wall-normal direction. As a result, the resolution of boundary layers down to the viscous no-slip wall (which would require a wall distance less than $y+ = 1$) is prohibitive for high Reynolds values. A wall function is then implemented by PowerFLOW to model boundary layers on surfaces.
The wall function is based on the standard *Law of the Wall* formulation:

$$u^+ = \begin{cases} y^+ & \text{if} \quad y^+ \leq 5 \\ \frac{1}{k} \ln\left(\frac{y^+}{A}\right) + B & \text{otherwise} \end{cases} \tag{4.31}$$

where $u^+ = u_s/u_\tau$ and $y^+ = yu_\tau/\nu$ are the well known dimensionless velocity and wall-distance coordinate. Friction velocity and wall shear-stress are respectively defined as $u_\tau = \sqrt{\tau_w/\rho}$ and $\tau_w = \frac{1}{2}\,\rho\, C_f\, u_s^2$. The parameters k and B have constant values empirically determined of 0.41 and 5 respectively inside the boundary layer logarithmic region ($30 \leq y^+ \leq 300$). The scaling function A carries the information of an adverse pressure gradient which slows down and expands the velocity profile:

$$A = 1 + f\left(\frac{dp}{ds}\right) \tag{4.32}$$

Equation 4.31 and the definition of the wall shear-stress define a system of two equations which once solved provide wall-shear stress for the wall boundary condition.

4.3.2 Turbulence modeling

Turbulence models are mathematical models that help in the prediction of turbulence effects without first computing the full-time-dependent flow field. In PowerFLOW® if the Reynolds Number is limited is possible to solve the lattice-Boltzmann equation 4.18 without modelling the turbulence. When the lattice length of the simulation is small enough to directly capture/resolve the smallest scales of turbulence, the direct simulation method can be applied. In this case, the solution is therefore equivalent to performing a Direct Numerical Simulation (DNS) of Navier-Stokes equations in the limit of the dynamic range [14] ($Re < 10^4$).
For high Reynolds numbers, however, the high computational cost associated with LBM-DNS leads to the need for a turbulence model. In general, the LBM can be

coupled with different turbulence modelling methods. In the case of PowerFLOW, a modified two-equation $k-\epsilon$ model, based on the renormalization group (RNG) formulation is incorporated into the LBM scheme.
Unsolved scales are selected through a model which is based on the local swirl of the flow. This method is denoted as LBM-Very Large Eddy Simulations (LBM-VLES) and its concept is similar to the one used in the non-zonal hybrid RANS/LES [14]. The turbulent kinetic energy k and dissipation ϵ are then calculated by solving the RNG $k-\epsilon$ two-equation model through a second order time-explicit finite-difference scheme on the same LBM grid. The model is used to compute a turbulent relaxation time which is then added to the viscous relaxation time:

$$\tau_{eff} = \tau + \tau_{turb} = \tau + C_{\mu}\frac{k^2/\epsilon}{T(1+\tilde{\eta}^2)^{1/2}} \tag{4.33}$$

where $C_{\mu} = 0.09$ and $\tilde{\eta}$ is a function of different parameters including the local vorticity.

4.3.3 Grid generation

The continuous geometric domain within which the simulation will be performed is divided into discrete cells via the generation of a Grid (Mesh). In a general mechanism for mesh, creation depends on the type of solver. In PowerFLOW® a semi-automated procedure is used which is significantly different from most Navier-Stokes-based flow solvers.
During the discretization step of PowerFLOW®, the whole simulation domain is split into lattice components, known as a voxel. When the lattice interacts with a solid body a surfel is created which is a planar lattice. The two different types of elements are presented in Figure 4.4

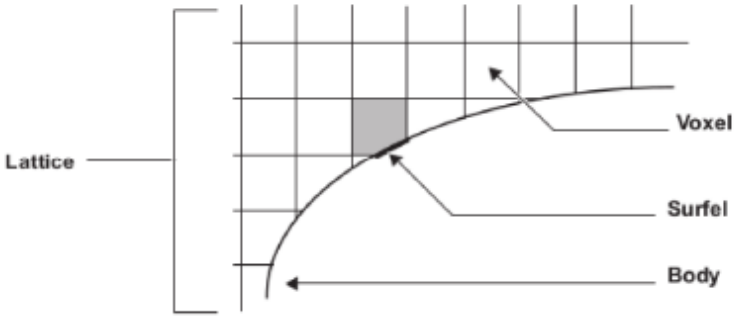

Figure 4.4: Elements of the mesh (lattice) in PowerFLOW® [38]

During the simulation, the fluid particle goes from one voxel to the next following the lattice structure. If it finds a surfel then the user-defined BC is initialized.
In order to be able to realize one simulation that is not prohibitive from the point of view of the computational cost, the dimension of the elements of the mesh must be varied. The smallest size in the mesh must be placed in the region of greatest physical interest (in other words in the region where the main fluid-dynamic phenomena that we want to study occur). Moving away from this region the dimension of the elements is increased up to the limit of the domain where we are not interested to have a high resolution.
In PowerFLOW® the mesh is divided into Variable Resolution regions (VR). The voxel size between successive VR regions increases by a factor of 2 (volume increases by a factor of 8) as compared to a higher resolution region while the time steps halves, as shown in Figure 4.5.

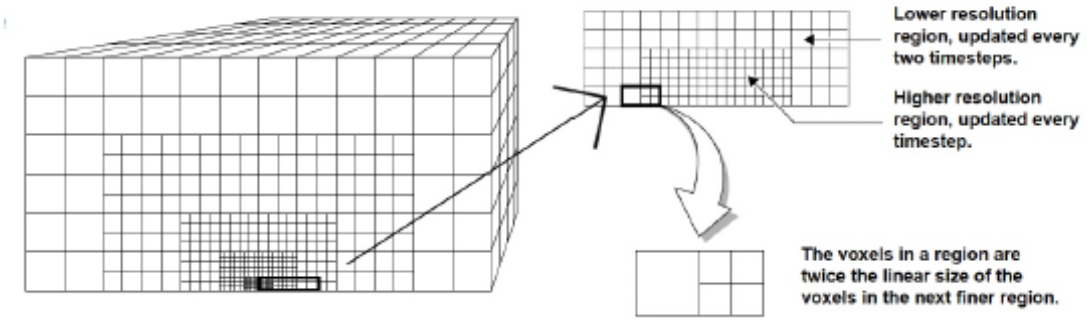

Figure 4.5: VR regions define the voxel size in PowerFLOW® [38]

The interval of data collection between distinct VR areas changes as a multiple of 2^{n-1} (where n defines the VR level) to guarantee that the data between different VR regions are in sync. The VR with the finest voxel ($n = 1$) size defines the resolution of the simulation, which can be interpreted as the extent to which flow phenomena are resolved in the simulation. The choice of the resolution and number of VR regions is a trade-off between computational cost and desired accuracy and is highly affected by the available computational power.
In the particular case of this thesis, a rotating body is present within the geometry. To simulate the rotation of a body (such as a propeller) it is possible to define a rotating local reference (LRF). This allows the user to include rotating elements inside the domain of analysis. Enclosing the rotating geometry inside the LRF creates a new reference frame allowing the user to define the rotating speed of the parts. In PowerFLOW® there are two main types of LRF:

- **Stationary LRF:** This reference does not rotate with respect to the global

frame but produces excellent results in many applications. If flow proprieties are not axisymmetric it creates artefacts.

- **Sliding-mesh LRF:** In this case the frame itself rotates with respect to the surrounding domain, hence this form of rotating frame area changes position and orientation relative to other parts of the domain.

During the discretization of the local rotating frame, PowerFLOW® divide it into different axisymmetric rings. When defining this region it is important to pay attention to the constraint that a sliding-mesh LRF can only cross two different VR regions during rotation as shown in Figure 4.6.

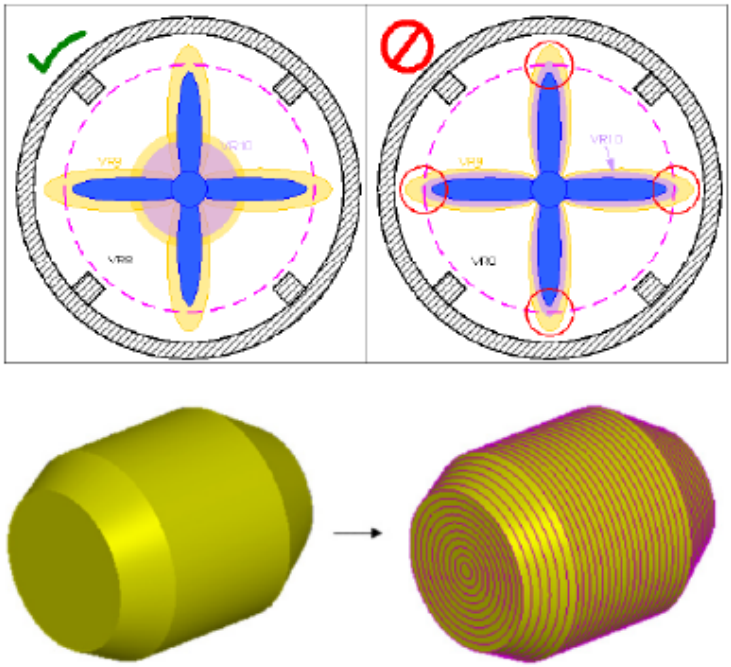

Figure 4.6: Constrains on the definition of a sliding-mesh LRF [38]

4.4 Aeroacoustic solver

The Lattice Boltzmann Method is inherently unsteady and compressible, thus it allows to perform noise extraction from the CFD solution. In order to maintain an acceptable computational cost during the calculation of noise in the far-field acoustic and thus reduce the resolution requirements on the far-field grid, the Ffowcs-Williams-Hawking (FW-H) analogy (which has been introduced in 2.4.2) is used.
The aeroacoustic analysis performed in this thesis is based on a hybrid LBM/FW-H methodology in which the unsteady and compressible near-field solution is produced using the LBM, and then the FW-H equation is used to compute the resulting far-field noise radiation. In PowerFLOW®, the surface on which the pressure field necessary for acoustical analysis is integrated can be chosen between two types. On the basis of this choice, two methods are defined by which of the FWH analogies is applied:

- **FWH solid surface (FWH SLD):** In this case the selected surface coincides with a physical body, usually the body of interest in the analysis. This method requires low computational resources as it neglect the *quadrupole* term $p'_Q(\boldsymbol{x}, t)$ as its computation involves a time consuming volume integration. Hence, when adopting a solid FW-H approach only the linear effects related to body thickness (*monopole*) and aerodynamic loading (*dipole*) are accounted for. The method could lead to erroneous results when applied to cases where volume terms significantly affect the acoustic field (eg. for jets or rotors at transonic blade-tip Mach numbers) [39].

- **FWH permeable surface (FWH PRM):** Firstly introduced by Di Francescoantonio [40] in this method the integration surface is placed away from the physical surface of the body attempting to capture the contribution of both surface and volume terms. The position of the surface strongly influences both the computational cost and the accuracy of the computed result. Interaction of turbulent structures and hydrodynamic fluctuations with the surface can result in spurious noise signals which are non-physical sounds. Moreover, when employing a permeable FW-H approach, the integration surface should be ideally placed in a region of high CFD grid resolution to accurately capture pressure fluctuations. If the region is far away from the body it results in a high computational cost. However, placing the surface too close to the body may lead to some volume terms not being included within the volume and thus to the emergence of spurious sounds.

To address the *spurious noise* problem that may be encountered while employing the FWH permeable surface approach different strategies can be adopted to limit their generation. The most relevant are discussed below.

- The first strategy sees the use of an *an open integration surface* to exclude the surface contaminated by hydrodynamic fluctuations from the calculation. A drawback of this method is that by eliminating a surface its contribution to the overall acoustic field is discarded from the computation, thus resulting in directivity errors [41].

- Another commonly used approach involves creating multiple porous surfaces with different downstream *end-caps*. On these surfaces (caps) the noise is evaluated separately for each surface and then averaged in the time- or frequency-domain to filter the hydrodynamic spurious content out from the acoustic signature [42].

4.4.1 Acoustic signal sampling

When performing acoustic analysis, it is important to properly sample high-fidelity flow source data in both spatial and temporal resolution. These determine the maximum frequency captured and how well the sampled signal reproduces the characteristics of the real one, thus avoiding falling into the phenomenon known as *aliasing*.

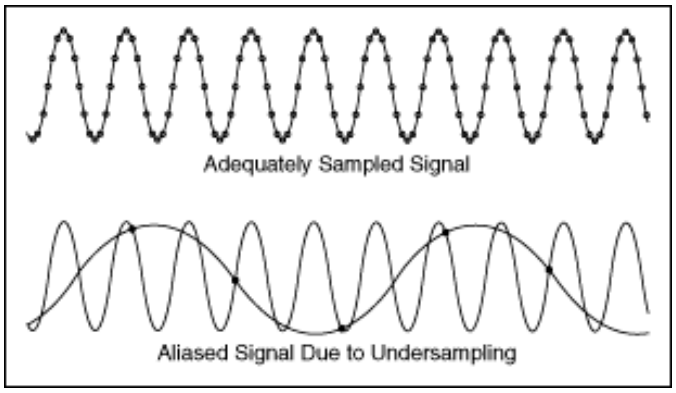

Figure 4.7: The importance of sampling rate to avoid the phenomenon of *alising*

When the sampling rate is not high enough, the information obtained from sampling a signal is not sufficient to reproduce the original signal thus leading to a reproduction error (Figure 4.7. The time criterion is directly related to the *Nyquist criterion*. The criterion states that the sampling frequency (f_s) must be at least twice the maximum frequency (f) of the phenomenon to be sampled:

$$f_s \geq 2f$$

However, when memory allows is better to increase the sampling rate by a factor of three or four to get a better resolution. On the other hand, since sampling is done within a discrete domain (mesh), it is important to define a spatial criterion for capturing acoustic waves. The gird size in the region in which the FWH integration surface is located determines the maximum range of frequency which can be analyzed. A good criterion is to assume a minimum of 10 voxels per wavelength to properly capture the behaviour of a wave [11], however in this thesis a minimum of 15 voxels (15 sampling points) has been considered.
Another key condition that must be considered when conducting an acoustical analysis is to start sampling pressure only after the initial transient phase during which the quantities have not yet converged. To reduce the total time of higher-resolution simulations that require high computing power, the flow field from a coarser one is used as a seeding file. Thus reducing the transient time. The following criteria are a good guidance to decide the start time of the measurements t_{start} [43];

- The aerodynamic parameters characteristic of the examined phenomenon should be monitored and used as a convergence factor. Sampling must begin when the selected convergence criterion has been satisfied.For example, considering the lift or drag coefficient:

$$t_{start} \text{ if } \Delta C_L \text{ or } \Delta C_D \ < \ \varepsilon$$

- There must be a sufficient number of flow passes across the item of interest. Consider at least 10 flow passes:

$$t_{start} \leq \frac{10l}{u_\infty}$$

The present thesis aims to analyze the aerodynamics and aeroacoustics of a ducted fan in hover conditions. The free stream speed value V_∞ has been considered to be equal to zero, therefore the choice of the criteria for the sampling starting time has been challenging. The selected parameters for both the fluid dynamics and aeroacoustic simulations are discussed in Chapter 5, while the convergence study is discussed in Chapter 6.

Chapter 5

Setup

This chapter presents the design of the ducted fan model realized for the thesis. The settings used in preparing the fluid dynamic and acoustic simulations are also presented. In Section 5.1, the model geometry is described while in Section 5.2 the setup used in the numerical simulations is discussed. First, the characteristics of the mesh are discussed, particularly the reference system, the domain size and the variable resolution regions. The characteristics and location of surfaces employed in the far-field analysis are then presented. Finally, the simulation settings and parameters are reported.

5.1 Ducted Fan Design

The choice of the engine geometry for the analysis has been made in such a way to comply with the following requirements:

- The engine must consist of a rotor and outlet-guided vanes (OGVs).
- The geometry of the rotor blades must be such that the blades work well close to a surface. Thus, the rotor must be a fan and not a propeller.
- The solidity of the rotor must be high (high number of blades to have a high Δp on the rotor disk)
- The engine size must be such that it can be installed on eVTOLs.

First, the few available geometries in the literature were evaluated but unfortunately, due to the low number of blades and lack of stator elements these geometries were rejected. It was then decided to use the Source Diagnostic Test fan rig of the NASA Glenn research centre (NASA SDT). This model is equipped with 22 fan blades and 26 Outlet Guide Vane (OGVs) and it perfectly fulfils all the desired

Figure 5.1: NASA SDT model installed at the NASA Glenn Wind Tunnel.

characteristics. The original geometry is shown in Figure5.1.
Since the design of the NASA engine is confidential, the dimensions and characteristics of the blades, as well as the internal dimensions, cannot be reported in this thesis. However, the figure below shows the values of the design point of the original NASA engine. These data can be found in the literature [44].

No. of Fan Blades	22
Fan Tip Diameter	22 in
Radius Ratio	0.30
Corrected Tip Speed	1,215 ft/sec
Corrected RPM	12,657
Corrected Fan Weight Flow	100.5 lbm/sec
Specific Flow	41.8 lbm/sec-ft^2
Stage Pressure Ratio	1.47
Design Bypass Ratio	8.85

Figure 5.2: Original fan design parameters [44]

As will be discussed later, the design conditions of the original engine are far from those that were used in the analysis. While the original engine is being used as a reference for turbofan analysis in the case under study, the engine is intended for UAM applications. Therefore, the operating conditions are far from the design point.

5.1.1 Wing and Nacelle

The first step in the design process involved main wing sizing and airfoil selection. This choice was guided by some aspects that the final model needed to meet:

- The engine should be integrated into the wing without compromising the inlet area which must be symmetrical.
- The engine nozzle should match the trailing edge of the wing (as this configuration has proven to be the most promising one).
- The wing should be equipped with a rotating system which allows the engine to rotate from cruise to hover condition and vice versa.

Following these constraints and, after some testing, a NACA 0010 airfoil was chosen and the wing has been divided into two parts to reproduce the mechanism that allows the engine to rotate. The total length of the wing is $l_{wing} = l_{front\ wing} + l_{engine\ wing} = 2.02\,m$ while the span of the model is $s_{wing} = 2.72\,m$. The length of the front wing $l_{front\ wing}$ is taken from the leading edge of the wing to the axis of rotation while the length of the engine wing $l_{engine\ wing}$ is taken from the trailing edge to the axis of rotation. The sizes of the wing are presented in the following figure.

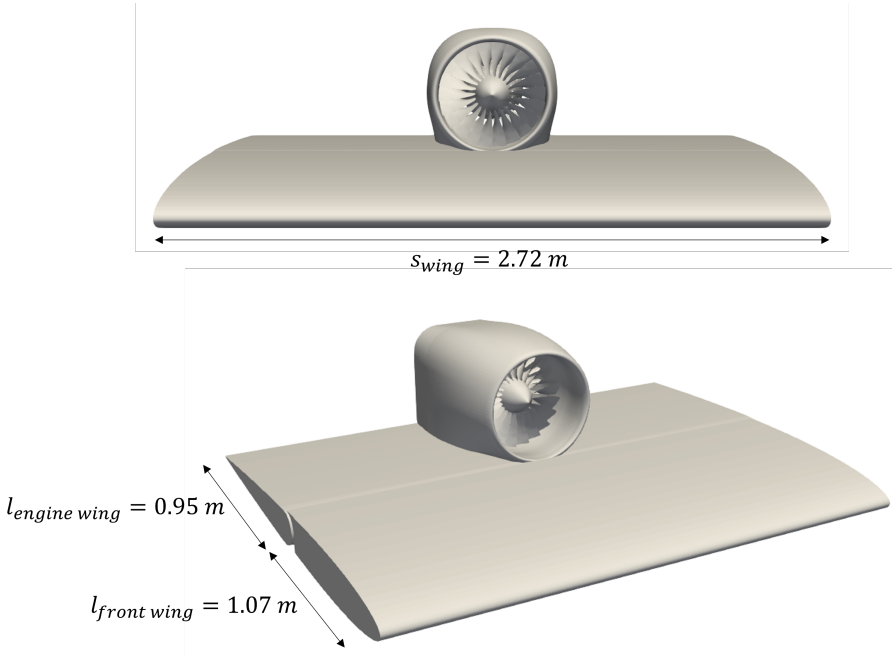

Figure 5.3: Geometry of the model and wing sizes: frontal view (top) and 3-D view (bottom)

The nacelle of the engine has been modified so that it can be integrated with the wing. The final design sees the engine rotated by an angle $\beta = 4.5$ degrees with respect to the chord of the airfoil. This angle is necessary to allow the engine to have the inlet section parallel to the surface of the wing underneath. In the figure below the final design of the engine integrated over the wing is shown. The 3D model used in the simulation was made using Solidworks.
Please note that in Figure 5.3 the engine is in the cruise configuration for illustration purposes only. The analysis as already introduced has been performed for the hover configuration with the engine rotated as shown in Figure 5.4.

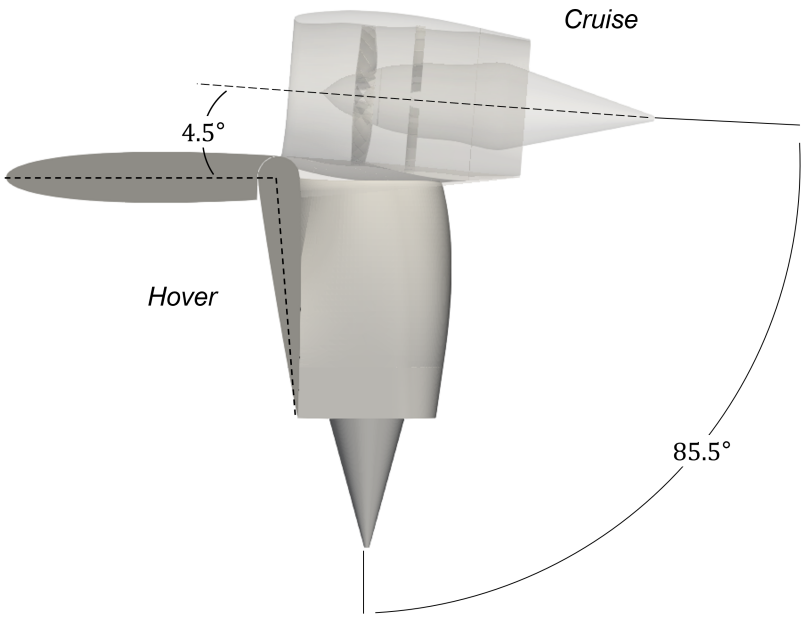

Figure 5.4: Cruise and Hover configurations of the engine

5.1.2 Variable Nozzle

The focus of this thesis is to analyze the variation in performance and noise generated by the engine as the exit area increases. This variation is achieved by symmetrically rotating the two elements into which the nozzle has been divided. The original circular nozzle geometry has been modified to recreate the shape used by Lilium and thus make it more realistic. The overall geometry of the model attempts to recreate that of a single engine, which in the actual application is implemented in a distributed system on the eVTOL wing. In the final model, the nacelle total length is $l_{nacelle} = 0.93m$ while the variable nozzle length is $l_{variable} = 0.2m$. The shape of the nozzle exit was therefore chosen to be square

with bevelled corners, both to maintain the flow symmetry and to keep the idea of an engine designed to operate in a distributed thrust vectoring system.
The area ratio σ is calculated using the disk and exit area of the engine without the area of the hub as follows:

$$A_{disk} = \frac{d_{disk}^2 - d_{hub}^2}{4}$$

The disk area of the engine is $A_{disk} = 0.2438m^2$ which is obtained by converting the rotor diameter from inches to meters (data from Figure 5.2). In Table 5.1 the main engine sizes needed in the area ratio calculation are presented. The value of exit areas refers to the baseline case $\sigma = 0.9$.

d_{disk} $[m]$	$A_{h_{disk}}$ $[m^2]$	A_{disk} $[m^2]$	$A_{h_{exit}}$ $[m^2]$	A_{exit} $[m^2]$
0.5572	0.09287	0.2167	0.06881	0.1951

Table 5.1: Engine areas

The baseline design of the engine has been designed to have an area ratio of $A_{exit}/A_{disk} = \sigma = 0.9$ following the Lilium findings [4]. These analyses show how the optimal area ratio for the cruise condition is $\sigma = 0.9$, while for the hover condition it increases to $\sigma = 1.3$. It is important to note that these results were obtained through a low-fidelity approach on an engine with different characteristics from the one analyzed in the thesis. Nevertheless, the $\sigma = 0.9$ case has been considered as the cruise-optimized configuration to simplify the analysis. Again, this is an assumption since no analysis of the engine in the Cruise condition was performed.
To verify whether the increase in area ratio under hover (maximum power) conditions results in a gain in efficiency and thrust generated by the engine, two cases were chosen to be analyzed: $\sigma = 1.1$ and $\sigma = 1.3$. Moreover, along with them a case in which the exit area is reduced has been analyzed to have a global view of the behaviour of the engine in these conditions, resulting in a total of 4 cases. In this case the area ratio is $\sigma = 0.7$. The choice of the exit area increment was limited to the $\sigma = 1.3$ case as for high wall deflections flow separation is expected. In Figure 5.5 the magnitude of area change determined by the nozzle rotation in the cases investigated is shown.

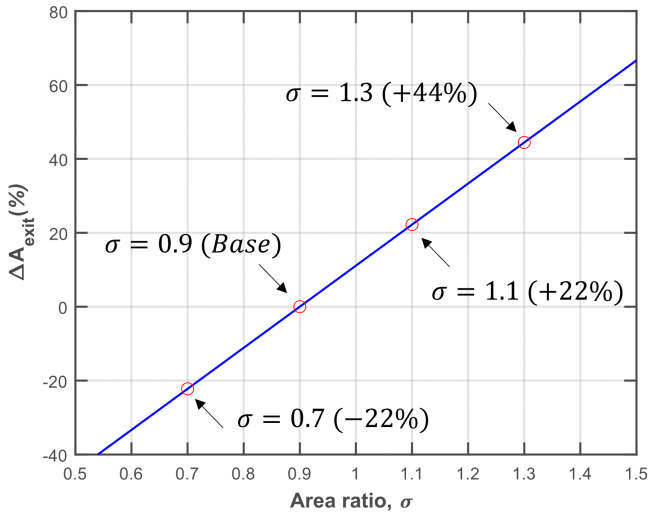

Figure 5.5: Exit area variation with respect to the baseline geometry

The process involving the calculation of the rotations necessary to obtain the defined values of area ratios first required the determination of output area values obtained for known rotation values. This first process was carried out directly on the CAD model using Solidworks software. This was necessary because the relationship between rotation and area variation is not exactly linear. Indeed, the change in the hub area influences the final value. The area values have been obtained considering a rotation of $\alpha = [5°, 10°, 15°, 20°, 25°]$.
Then, these data were interpolated and extrapolated to obtain a trend between a negative rotation of $\alpha = -30°$ and positive rotation of $\alpha = 40°$.
In the following table, the rotation needed for each considered case is presented while Figure 5.6 shows the entity of the rotation needed for different values of area ratio.

σ	α [◦]	ΔA_{exit} [%]
0.7	−11.5	−22
1.1	+11.7	+22
1.3	+24.8	+45

Table 5.2: Nozzle rotation and exit area variation for the chosen cases

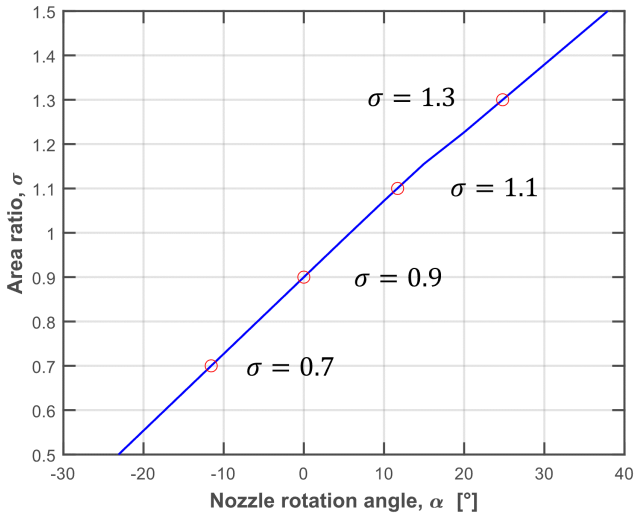

Figure 5.6: Nozzle rotation for different area ratios values (σ)

Finally, in Figure 5.7 the 3D model with the 4 different nozzle configurations is displayed. The two elements of the nozzle are simply rotated in different configurations, thus the total length of the engine is different for each case.

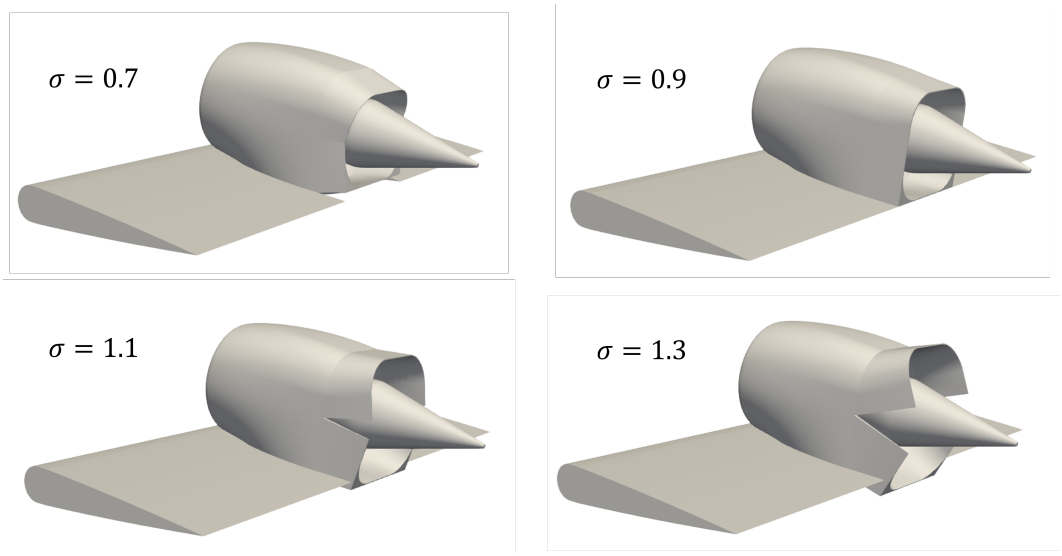

Figure 5.7: Nozzle configurations analyzed in this thesis

5.2 Numerical Simulation setup

The model presented in the previous section has been divided in different elements during the design phase. Then, the different parts were joined to create an assembly and saved as an *.stl* file. Finally, the different parts were imported into PowerFLOW. It was important that the parts were uploaded as individual elements in order to be able to define offsets of the parts themselves. These offsets were then been used as refinement regions of the mesh as will be described later in this section.

5.2.1 Coordinate systems

Three coordinate systems have been defined in the computational setup:

- **Default/Global Coordinate System è [x y z]**: the Default/global coordinate system is the global coordinate system for the setup. The other coordinate systems are defined upon it. It is located at the leading edge of the frontal wing, in the middle of the wing span. It has been also used for the definition of the simulation domain (Figure 5.8 a).
- **Fan Coordinate System [x' y' z']**: this reference system was defined to better analyze the fluid properties during post-processing (such as the velocity field). Also, it was used as a reference during the definition of the different VRs inside and outside the engine (Figure 5.8 b).
- **Local Rotating Reference Frame [x" y" z"]**: The LRF identify a region of the setup in which the simulation is performed in a rotating frame. This coordinate system was specified during the volume of rotation definition process (which will be discussed later). Through the LRF the rotation velocity of the fan is defined. For this simulation, the fan rotates in an anti-clockwise direction (forward-looking the LRF coordinate system, Figure 5.8 c).

All the results presented in this thesis are relative to the Fan Coordinate System.

5.2.2 Domain dimensions

The simulation volume is a box-shaped region which contains all the other geometry in the case and bounds the fluid flows. The simulation volume is identified as a fluid region while the solid geometry (such as the model under investigation) must be identified as a solid element. The size of the simulation domain is usually much larger than the analyzed model. It must be large enough to minimize wall effects on the flow field. In this thesis, the dimension of the simulation domain

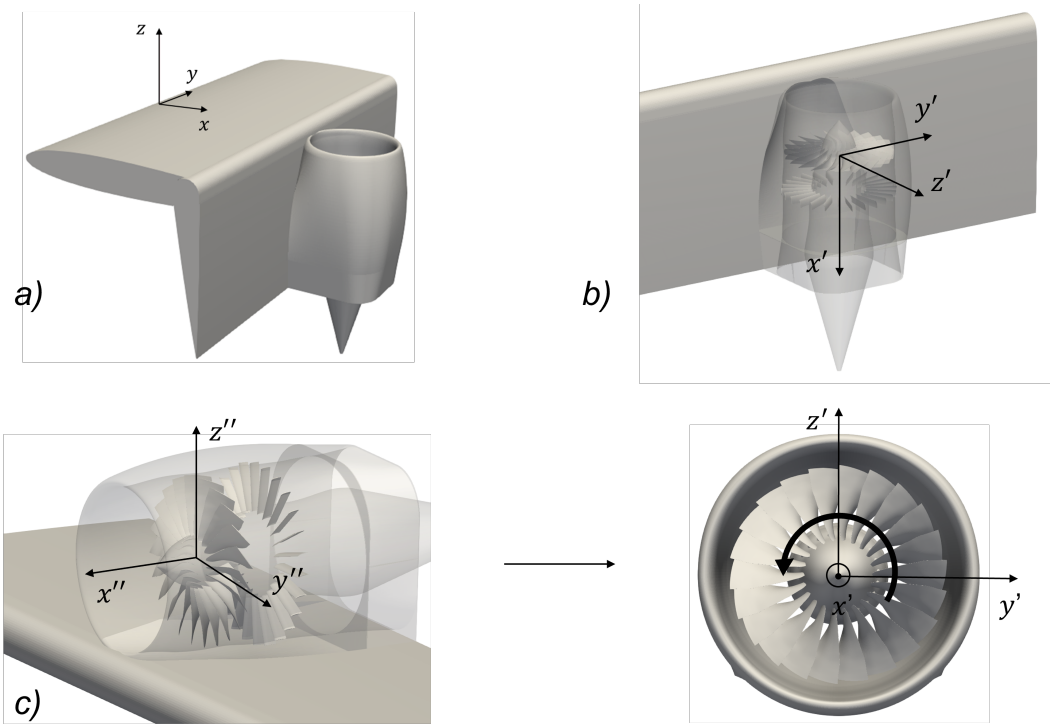

Figure 5.8: Coordinate systems defined in the numerical setup and fan rotation direction

has been defined taking the Fan Coordinate Systems as a reference. The side walls of the domain are located on both sides of the frontal wings symmetrically to the reference system. Therefore the distance of the two lateral faces of the domain from the Fan Coordinate System is $l_y = 1.36\,m$. The Other 4 faces are placed at a constant distance from the Fan Coordinate System in both the x and z directions. More precisely, at a distance equal to 60 times the diameter of the rotor: $l_x = l_z = 60 \cdot D_{rotor} = 32.84\,m$. In Figure 5.9 the simulation volume is shown together with its dimensions. As can be seen, the edges of the domain include rectangles. These must be defined in the case file so that the boundary conditions at the inlet, outlet and on the other edge can be assigned. The boundary conditions, along with the parameters used in the simulations, are discussed in section 5.4.

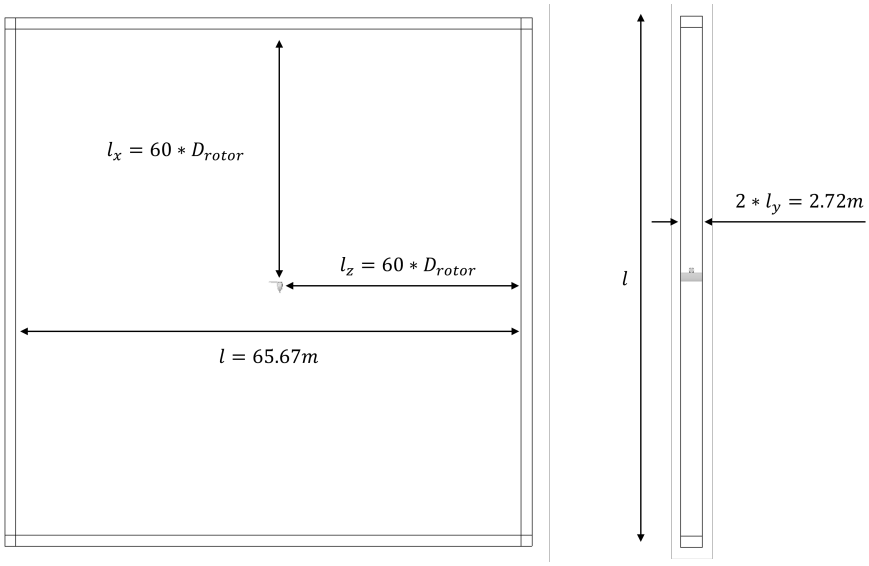

Figure 5.9: Simulation volume dimensions

5.2.3 Mesh resolution

The geometric domain that one wants to study must be discretized through the generation of a mesh, as introduced in section 4.3.3. Mesh resolution is a key factor in any numerical simulation. In the case of computational fluid dynamics (CFD), it defines how well the flow field is discretized and in particular the distance between two neighbouring cells. High resolution allows for high simulation accuracy but on the other hand, greatly increases the computational cost of the simulation. Therefore, the geometric domain is discretized into different regions each with different resolutions. However, neighbouring regions must have a level of resolution which change with a constant increment factor. These regions are defined as Variable Regions (VRs) in PowerFLOW. The VR with the highest mesh resolution must be placed around the area of interest and in general close to those parts of geometry where relevant physical phenomena are expected to occur. Moving away from these elements the mesh gets progressively coarser till the lower level of resolution in the domain.
Referring to the finest mesh case (which has been used in the high resolution study) the domain has been divided into 12 VR regions. The corresponding voxel size for each VR level is presented in Table 5.3

VR Region	11	10	9	8	7	6
Voxel size [mm]	0.332	0.664	1.32	2.65	5.31	10.62
VR Region	5	4	3	2	1	0
Voxel size [mm]	21.25	42.5	85	170	340	680

Table 5.3: Voxel dimensions for each VR region (Fine mesh case)

Since the purpose of this analysis is to analyze the fluid dynamic and acoustic fields of this engine the areas of greatest interest at the physical level are the rotor and stator. Therefore, the highest resolutions VR regions are placed near these two elements. An algorithm was used to automatically calculate the total number of Vr and cell sizes in the various regions. Following is a brief explanation of the preceding procedure.
According to the target y+ value on the rotor blade, the smallest voxel size was initially determined. First, the Reynolds Number on the blade tip has been calculated:

$$Re = \frac{\rho U L}{\mu} = 9.615 \cdot 10^5 \tag{5.1}$$

where L is the tip chord of the blade and U is the velocity of the blade tip, while the values of ρ and μ have been taken from the free stream conditions. The tip velocity is considered to be $U = 153.13\, m/sec$, this value comes from the hypothesis of a rotor tip speed of Mach 0.45. More information will be given in Section 5.4. Now, an empirical correlation for a fully turbulent flow over a flat plate is used to

$U\ [m/s]$	$L\ [m]$	$\rho\ [kg/m^3]$	$\mu\ [Pa \cdot s]$
153.13	$9.17 \cdot 10^{-2}$	1.225	$1.789 \cdot 10^{-5}$

Table 5.4: Variables used in the Reynolds Number calculation

estimate the skin friction coefficient C_f:

$$C_f = [2 \log_{10}(Re) - 0.65]^{-2.3} \tag{5.2}$$

This empirical correlation can be replaced with any other empirical correlation. However, since the correlation is used just for an estimate of the $y+$ values, which correlation is chosen is irrelevant. Knowing the skin friction coefficient is now possible to compute the value of the skin friction τ_w:

$$\tau_w = \frac{1}{2} \rho U^2 C_f \tag{5.3}$$

The friction velocity u_τ and the y^+ value are then computed as follows:

$$u_\tau = \sqrt{\frac{\tau_w}{\rho}} \tag{5.4}$$

$$y^+ = \frac{\rho y_p u_\tau}{\mu} \tag{5.5}$$

Where y_p is the height of the cell centroid. Finally the height of the cell can be calculated:

$$y_h = 2 \cdot y_p \tag{5.6}$$

With this method, defining a y^+ target on the blade chord is possible to compute the finest voxel size of the mesh. The total number of VRs regions is also assumed to be $N = 13$ in this initial phase.
Since in PowerFLOW the grid is composed of cubic cells, the height of the cell corresponds to its size. Moreover, the simulation volume has a thickness equal to the frontal wing span, the largest voxel size in the grid must be at least half this dimension. In other words, in the lower resolution VR region there must be at least 2 voxels in the y direction of the domain (see Figure 5.9).
Starting from the finest voxle size computed with the method described above the largest voxel size is calculated with the following equation:

$$dx_{VR_i} = dx_{finest} \cdot 2^{N-i} \tag{5.7}$$

where N is the total number of VR regions. At this point, the cell size in the most coarse region is compared to the domain width. If the largest voxel size allows more than two voxels on the domain thickness this value is kept. Otherwise, the cell size is set as half the Y domain thickness. As a result, all other regions will be scaled up from this value. For the finest case the size of the different voxel are presented in Table 5.3.

In this analysis, the rotor and stator blades are the regions of greatest interest. Therefore, VR regions from 11 to 9 which are the regions with the highest resolution are placed in these regions. By doing so, the most important fluid dynamic phenomena in these regions are effectively resolved while also optimizing the simulation's computational cost. To verify that the mesh resolution is not influencing the results a grid convergence analysis is necessary. For this purpose, 4 levels of mesh resolution were defined. In Table 5.5 information on the grid resolutions levels is presented. Detailed information on the grid convergence study will be provided in Chapter 6

Resolution	VR levels	Smallest voxel (10^{-4} m)	Fine equivalent voxels (10^6)
Very Coarse	9	26.5	2.00
Coarse	10	13.28	11.37
Medium	11	6.64	73.6
Fine	12	3.32	519.43

Table 5.5: Levels of mesh resolution for the grid convergence study

5.2.4 VR regions

For the analyzed case the mesh can be divided into three key regions: the high-resolution region inside the engine (which also include the wake refinement), the field around the engine (medium resolution regions) and the far-field (low-resolution regions). In Figure 5.10 the location of the variable resolution regions outside the engine is shown. The shape of the variable resolution regions of the field around

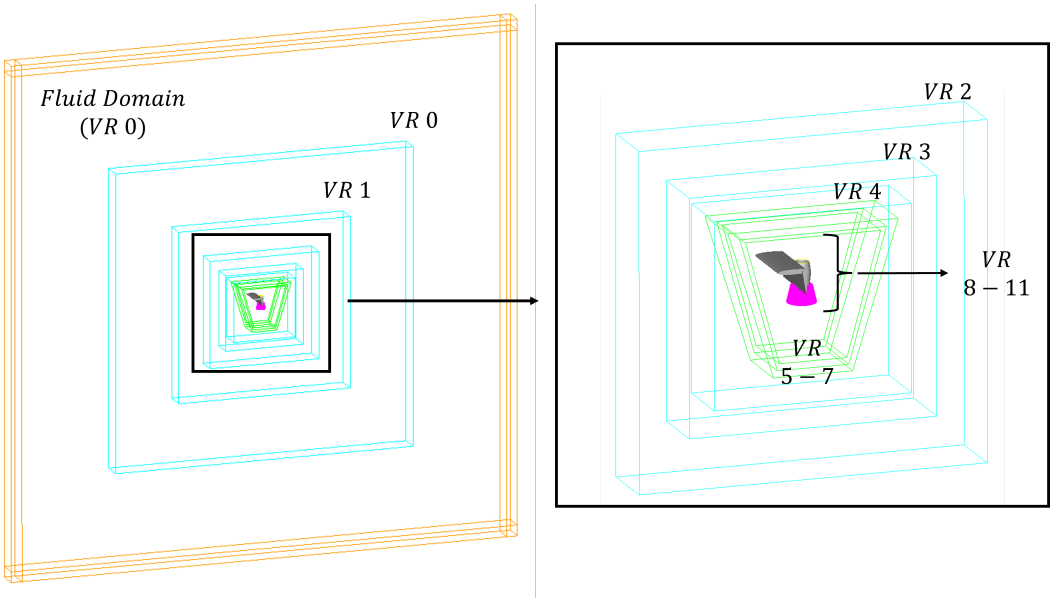

Figure 5.10: Variable resolution regions, far-field (light blue), near field (green) and high resolution VRs

the engine(VRs from 5 to 7) was chosen so that the surface used for the permeable Ffowcs Williams and Hawkings method could also be placed within it. In addition, the chosen shape makes it possible to reduce the number of voxels in that region and thus the computational cost. Mesh resolution does not affect the position or

size of these regions. On the other hand, the far-field regions (VR levels from 5 to 0) have a cubic shape and are variable in size. In this case, the distance between these regions is defined by 6 voxels, whose size varies depending on the level assigned to each (this changes as the mesh resolution changes). As these areas are far from the region where the fluid dynamic phenomena of interest can be found, is not necessary to keep their position fixed. A crucial aspect is that all these regions have the same thickness as the fluid-dynamic domain. Distances of the mid-field VR regions are presented in Table 5.6. Distances are given taking the Fan coordinate system as reference.

VR level	**Offset [-X]**	**Offset [+X]**
7	$3 \cdot D_{rotor}$	$6 \cdot D_{rotor}$
6	$VR_7 + 0.25 \cdot D_{rotor}$	$VR_7 + 0.5 \cdot D_{rotor}$
5	$VR_6 + 0.5 \cdot D_{rotor}$	$VR_6 + 0.5 \cdot D_{rotor}$
4	$VR_5 + D_{rotor}$	$VR_5 + D_{rotor}$

Table 5.6: High resolution VR regions location

Concerning the high-resolution regions, VRs were positioned in such a way that they could optimally resolve the fluid dynamic phenomena of interest for the analyses. The two finest VR levels have been defined on the stator and rotor blades as offsets of these surfaces. In this case offset means the creation of a region having the same geometry as the selected surfaces which is placed at a defined distance from them. Specifically, the distance of the two offsets from the surface of the rotor and stator blades are fixed to 6 and 12 voxels of the finest level of the Coarse mesh respectively. Moreover, for grid consistency an offset of the hub and nacelle with a VR level of 10 was also created. The location of the high resolution VR regions are presented in Table 5.7 while in Figure 5.11 the same regions are shown.

5.3 Acoustic settings

To investigate the noise produced by the engine, a far-field analysis is carried out. In order to apply the FWH method, instantaneous pressure fluctuations were sampled on a permeable surfaces. Results from the two method have been compared and discussed in Chapter 8 together with the identification of the main noise source.
The level of resolution of the VR within which the permeable surface is placed influence the spatial resolution and in particular it define the highest frequency that can be sampled as described in Section 4.4.1. For a larger range of frequencies, it would be necessary to place the permeable FWH surface within a high-resolution

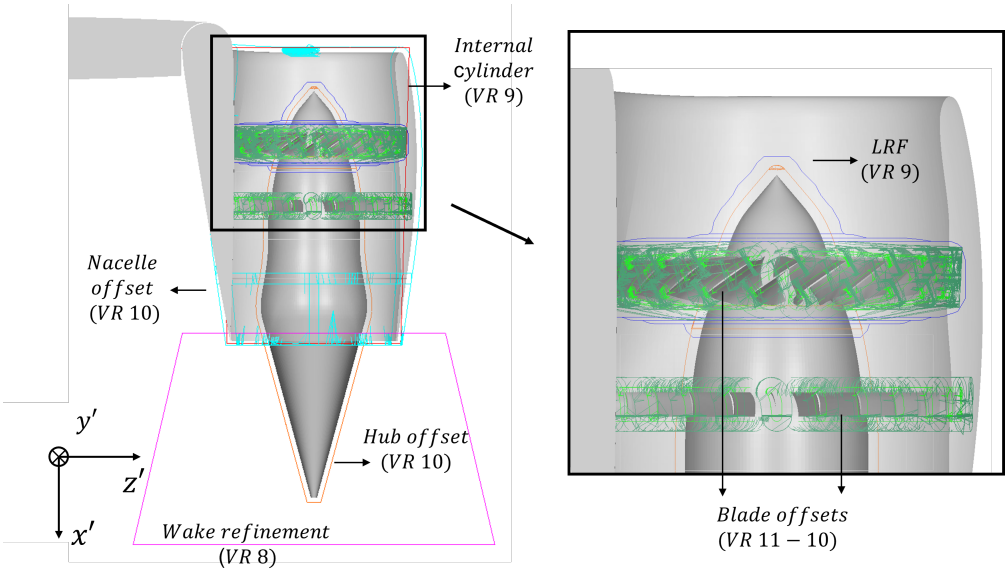

Figure 5.11: High resolution VR regions

VR level	Location	Color
11	Offset rotor and stator blades	Light Green
10	Offset rotor and stator blades Offset nacelle Offset hub	Dark Green Light Blue Orange
9	Internal cylinder LRF region	Red Dark blue
8	Wake refinement (cylinder)	Purple

Table 5.7: VR levels and locations in the high resolution regions

region, but this would increase computation costs significantly. By placing the permeable surface of FWH inside the VR 7, the computational cost could be reduced while still resolving the acoustic field. Thus, the permeable surface ahs been placed inside the VR 7 region as it represent a good compromise between computational cost and achievable results. The FWH permeable surface is displayed in Figure 5.12. The particular shape allows all noise sources to be enclosed while maintaining a necessary distance from the engine to prevent the formation of spurious noises, as already discussed in 4.4. The higher frequency sampled can be computed as follow:

$$f_{cutoff} = \frac{c_0}{N_{points}\, dx_{voxel}} \tag{5.8}$$

where $c_0 = 340.29\, m/s$ is the speed of sound which is the speed at which the pressure fluctuations move, $N_{points} = 15$ and dx_{voxle} is the dimension of the voxel of the VR inside which the surface is placed.

Resolution	**Spatial cut-off frequency** (Hz)
Very Coarse	534.05
Coarse	1068.10
Medium	2136.2
Fine	4272.4

Table 5.8: Cut off frequency from the spatial criterion considering 15 voxles per wavelength (VR 7)

Based on a cell size of $dx_{voxel} = 5.31 \cdot 10^{-3}\, m$ in the VR 7 region, the spatial cut-off frequency is $f_{cutoff} = 4272.4\, Hz$. The choice of VR level for the permeable surface results in a low cutoff frequency. Nevertheless, if it were placed in a finer region, the overall computational cost of the simulation would increase substantially. On the time side, an aliasing safety factor of 4 was used to calculate the sampling frequency which comes up to be $F_{sampling} = 20\, kHz$.
Table 5.8 shows the cut-off frequency for the different mesh resolutions. These data are given for completeness. However, since the finest mesh was used in the acoustic analysis, a grid convergence study was not performed on the acoustics field.

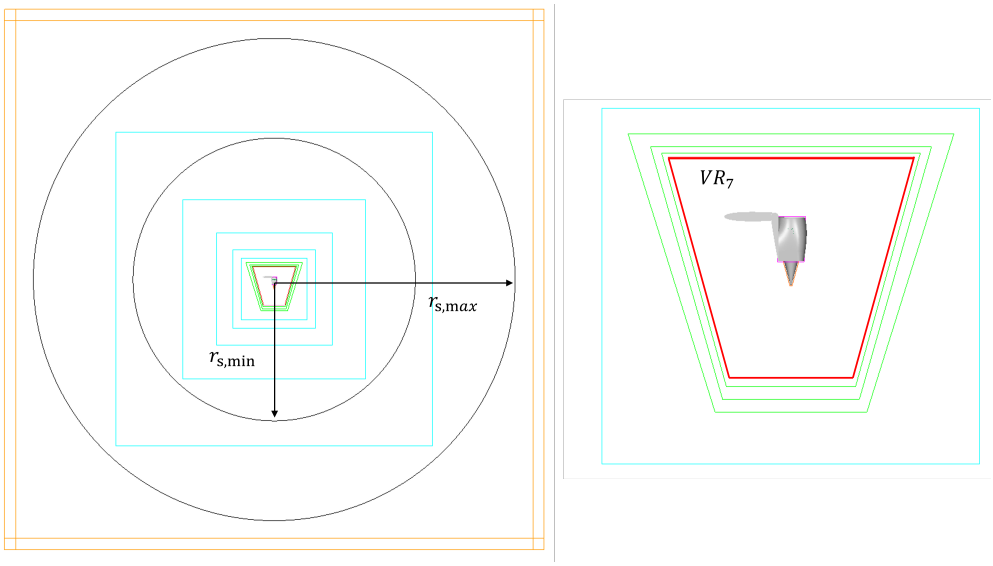

Figure 5.12: Acoustic sponges (black) and FWH permeable surface (red) locations

5.3.1 Acoustic sponge

When performing acoustic analysis over a restricted domain, acoustic waves may reflect off at the ends of the fluid domain, causing sound measurements to be artificially affected. To prevent this phenomenon, an acoustic sponge can be applied in the simulation. Acoustic sponge are defined as volume regions with a variable viscosity which act as an acoustic suppression zone. In PowerFLOW, the parameter $\Gamma = N_u/T$ can be adjust to dump the acoustic waves outside the area of interest. Two acoustic sponge have been defined in the simulation with the shape of cylinder with radius $r_{s,min}$ and $r_{s,max}$ respectively for the inner and outer sponge. The diameter of the two sponges was chosen so they would not cross any VR boundaries and to separate the region where acoustic phenomena will be analyzed from the outer region. The fluid domain is thus divided into three zones:

- **Inner region:** Region inside the small sponge which has a radius of $r_{s,min} = 17.18\,m$. Here Γ has a constant value of $\Gamma_{min} = 0.005$ since sound signals are not intended to be dumped.
- **Outer region:** Region outside the larger sponge where Γ has an higher value equal to $\Gamma max = 0.5$. This region is defined outside the $r_{s,max} = 29.32\,m$ radius sponge. Here the dissipation of the acoustics wave is maximized.
- **Transition region:** This region is located within the two sponges. The dumping effect increases from Γ_{min} to Γ_{max} according to the following function:

$$\Gamma = K_B \cdot exp^{(K_A \cdot r_s)} \tag{5.9}$$

where r_s represents the position relative to the Fan coordinate system,i.e., the position within the fluid domain. K_A and K_B are two constants which are defined as:

$$K_A = \frac{\ln\left(\frac{\Gamma_{min}}{\Gamma_{max}}\right)}{r_{s,min} - r_{s,max}} \tag{5.10}$$

$$K_B = \frac{\Gamma_{min}}{{K_A}^{r_{s,min}}} \tag{5.11}$$

5.3.2 Microphones position

To compare the acoustic field characteristics of the two chosen configurations, a Far-Field Analysis (FAA) was carried out. The data were obtained through the use of PowerACOUSTICS software, which takes as input pressure data sampled

on a solid or a permeable FW-H surface as described in the section 4.4. Points where the noise patter is computed are identified as microphones were arranged in a circular pattern around the engine in the XZ plane with a resolution of 10° for a total of 36 points.

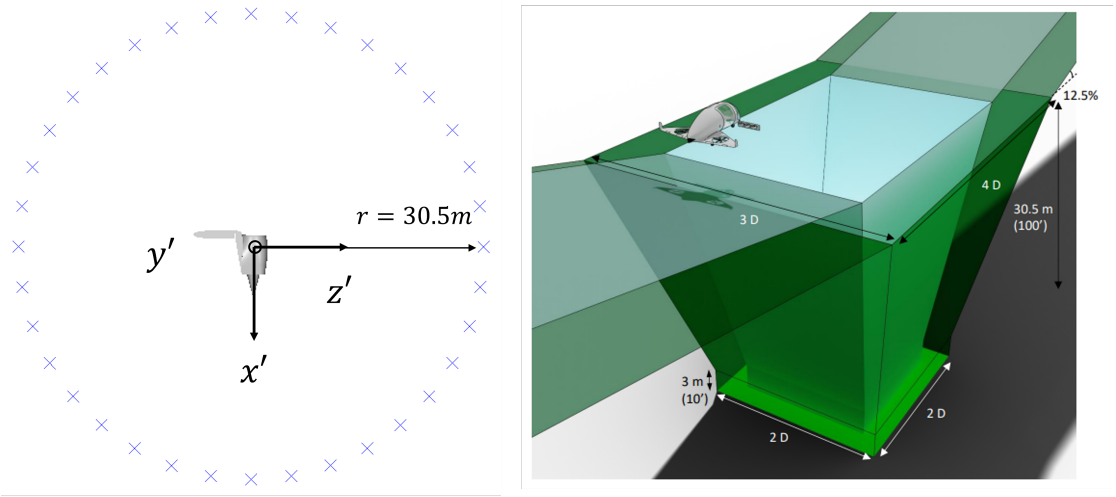

(a) (b)

Figure 5.13: Microphones locations and Vertiport model used as reference [45]

The choice of distance for far-field analysis (and thus the radius of the microphones circular pattern) was made based on the current regulation in the European e-VTOL aircraft field. In particular, since there is no regulation for the certification of noise generated by an aircraft belonging to this category, it was chosen to consider a model vertiport named *Reference volume Type 1*. Manufacturers of e-VTOL aircraft can use the model realized by EASA [45] as a reference to demonstrate how their aircraft can take off within this volume. The h2 parameter defined as the *High hover height* of the vertiport model is therefore chose as the distance at which the microphones are placed around the engine from the center of the Fan Coordinate System, $h2 = 30.5\,m$. The size and shape of the vertiport are presented in the figure 5.13 (b) together with the microphone circular array (a).

5.4 Global simulation settings

So far, the model geometry and the characteristics of the implemented mesh have been discussed, but not the global parameters that define the analysis. For this thesis, it was decided to study the ducted fan under hover conditions, thus considering a zero forward velocity. As a results, free stream conditions were taken

at sea level. The free stream turbulence is set at 1% of the local velocity which is set to $0.05\,m/s$ to have a non-zero value. The turbulence length scale is set to $1\,mm$. Those values describe the turbulence characteristics of a flow in its initial state.

Global parameter	Value
Pressure	$101325\,Pa$
Temperature	$288.15\,K$
Density	$1.225\,kg/m^3$
Kinematic Viscosity	$1.46 \cdot 10^{-5}\,m^2/s$
Turbulence Intensity	1%
Turbulence Length Scale	$1 \cdot 10^{-3}\,m$

Table 5.9: Global simulation parameters

The Reynolds Number of the simulation is calculated taking into account the characteristic length and velocity. The characteristic length is set to be the rotor blade tip chord $l_{char} = 9.17 \cdot 10^{-2}\,m$ and have been used also in the grid generation as the length used to calculate the resolution (number of voxels of the finest level over that length). For the characteristic velocity, the blade tip velocity has been considered. Assuming a blade tip velocity of Mach $U_{tip} = 0.45$ the rotational speed and thus the characteristic velocity was found to be $5344\,RPM$ and $U_{tip} = 153.13 m/s$ respectively. This choice was made in order to minimize noise generated by compressible phenomena. As low noise emissions is a key requirement that must be met for the type of aircraft on which such an engine is implemented. The Reynolds Number of the case is then found to be $Re = 961296$ which is the same as the Reynolds Number calculated in the mesh definition 5.1.

5.4.1 Boundary conditions

Boundary conditions are applied to every surface within the simulation.
In the case of the analyses performed, 3 types of boundary conditions were assigned to the surfaces:

- **Wall - Standard Wall**
- **Inlet - Pressure and Velocity**
- **Outlet - Static Pressure and Free Flow Direction**

The wall BC is assigned to all the surfaces of the model, i.e. nacelle, variable nozzle, rotor, stator, hub and the two elements of the wing. Since the simulation is

carried out using a Very Large Eddy Simulation method, as introduced in 4.3.2, a turbulence model is applied. In this case the boundary condition standard wall mimic a wall with a fully developed turbulent boundary layer. Thus the structures of the boundary layer are not resolved but a wall function is applied (see 4.3.1). The boundary conditions applied to the fluid domain surfaces are shown in the Figure 5.14

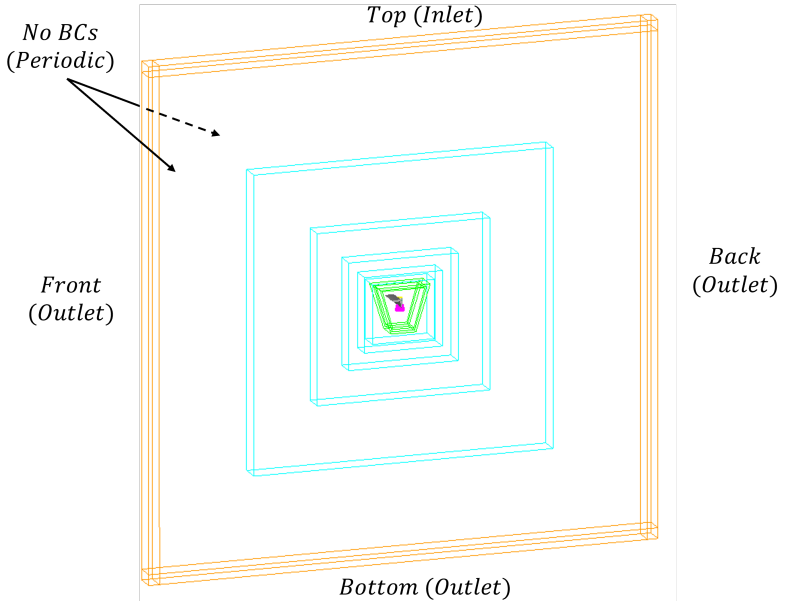

Figure 5.14: Boundary conditions associated to the fluid domain faces

For the Inlet boundary condition, the modulus and direction of the three velocity components and the ambient pressure were defined. While for the outlet boundary condition, only the ambient pressure value was assigned. Finally, the side surfaces were not assigned boundary conditions. In this case, the periodic boundary condition applies. Thus, fluid entering or leaving a simulation volume boundary face is equivalent to fluid leaving or entering from its opposite face. As a result, the wing is simulated as it was an infinite wing.

5.4.2 Time convergence

In section 4.4.1, the criteria behind the choice of the transient time for the simulation were introduced. For this thesis the value of the forces acting on the engine has been used as a method for identifying the transient time as the flow speed u_∞ is set to nearly $0\,m/s$. The condition used to identify the transient time is thus t_{start} if $\Delta F_z < \varepsilon$. The value of the force acting on the engine (in the z direction) is never constant due to the turbulent and unstable flow. Measurements were

considered unaffected by the transient phenomena if the difference between two consecutive rotations of the mean force in the z direction is less than $\varepsilon = 2\%$. In order to be more conservative, it has been decided to start measuring after 10 total rotations (which corresponds to 0.0674 *sec* in the simulation) despite the fact that the condition had already been met after 8 rotations. In figure 5.15 the time convergence of the forces is shown.

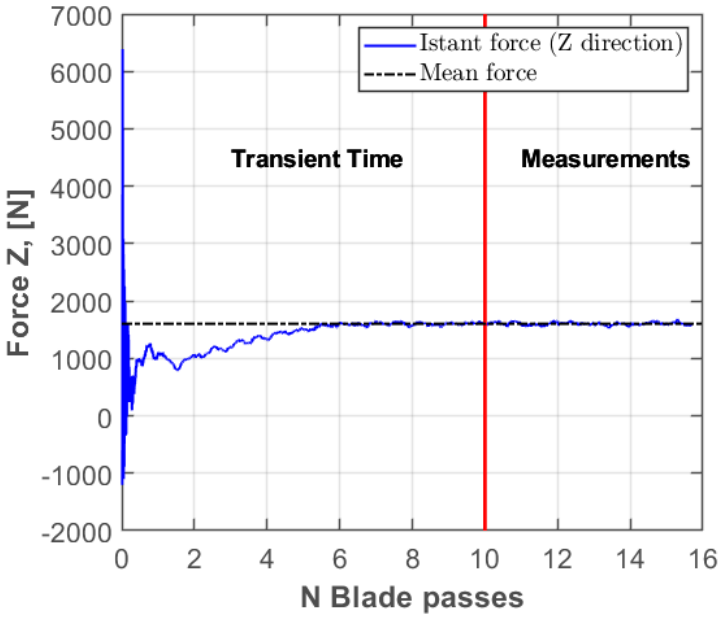

Figure 5.15: Time convergence of the forces acting on the engine, the red line show the end of the transient time

For simulations with a finer grid, the simulation has been initialized from a seed file obtained from the solution of a more coarse simulation (which has been carried out in the same conditions). This lead to a further reduction of the transient time an thus a reduction of the total computational cost.

5.4.3 Measurements

A crucial aspect in CFD simulations is represented by where and how measurements are performed. The size of the measurements files highly affect the computational cost and time. Thus, it is important to define the sampling domain as well as the sampling frequencies trying to limit it to only those domains of interest making a trade off between the computational cost and the amount of data necessary to understand the flow characteristics. In the following table the main measurements

Measurement type	Duration [sec]	Frequency [Hz]
Averaged forces	0.067	14.85
Averaged flow field	0.067	14.85
Instantaneous flow field	0.0112	6412
Instantaneous forces	0.0112	64128
FWH permeable	0.067	20000
Performance data on planes	0.067	14.85

Table 5.10: Simulation measurements

are presented.
The total time for the measurements is 0.067 *sec* which is equal to 6 complete rotations. However, not all the measurements has been carried out throughout this period to reduce the space required for saving data. For comparisons between different configurations, the flow and the main variables used for engine performance analyses were averaged over the entire measurement period.
To compare the two cases ($\sigma = 0.9$ and $\sigma = 0.7$) with the finest grid, the same process was carried out. In both the finer and coarser cases, instantaneous flow data were collected at a frequency equal to 5° of rotation (for a total sampling time equal to 1 complete rotation) and used for a deeper analysis of the unsteady phenomena. Whenever the temporal average is used, the signal comes from a period opposite to the sampling frequency, so every temporal step contributes equally to the measurement.
Instantaneous flow fields are the only exception, which are sampled as a single time-step in order to depict the flow pattern In the two cases in which the acoustic field is analyzed (and thus the grid is found to be the finest), the instantaneous forces on the rotor and stator were evaluated in order to compare with the acoustic data obtained and determine whether unsteady phenomena are affecting the noise generated. Measurements necessary for FWH application are also included here. A discussion of the motivations behind the frequency choice can be found in the Section 5.3

Chapter 6

Convergence study

Since the grid resolution affects the solver's ability to resolve the fluid-dynamic field, it is important to perform an analysis of grid convergence. This analysis aims to establish that the results are independent of the mesh resolution but it is also a straightforward method for determining the discretization error in a CFD simulation. Mesh characteristics are defined on the base of the operating condition under which the model is being studied. Hence, if these conditions are changed it is necessary to perform a new grid resolution. For this thesis, resolution studies have been done for the condition which was identified to be the baseline hover settings. In particular for an engine rotational speed of 5344 RPM and an exit area ratio of $\sigma = 0.9$.

6.1 Grid resolution analysis

As introduced in Chapter 5, four levels of mesh resolution were chosen to carry out the mesh convergence analysis, namely *Very Coarse*, *Coarse*, *Medium*, *Fine*. The resolution of the mesh is defined by the number of voxels assigned over the characteristic length represented in the case study by the rotor chord c. The settings of the four mesh resolution levels have been presented in Table 5.5. As the size of the smallest voxel is halved when the mesh resolution level is increased, the number of equivalent fine voxels quadruples increasing computational costs. Therefore, it is important to determine the effectiveness of the mesh refinement on the flow parameters' accuracy.

To examine the spatial convergence of the simulation the Grid Convergence Index (CGI) was chosen [46]. The Grid Convergence Index (GCI) methodology has been proposed to provide a mechanism to calculate and report discretization error estimates in computational fluid dynamics (CFD) simulations. It permits the

quantification of the uncertainty present in grid convergence. This method uses a grid convergence error estimator that is obtained by applying the generalized Richardson Extrapolation theory. The GCI of the finest grid which is represented by the index GCI_{21} (where 1 is the finest grid and 2 the 2^{nd} finest grid) is defined as follows:

$$GCI_{21} = \frac{1.25 \left| \frac{\phi_1 - \phi_2}{\phi_1} \right|}{r_{21}^p - 1} \quad \text{where} \quad p = \frac{|\ln \frac{\varepsilon_{32}}{\varepsilon_{21}}|}{ln(r_{21})} \tag{6.1}$$

In the equation above, r represents the grid refinement factor (between two consecutive grid resolution levels) which is $r = 2$ for this study, p is the apparent order of convergence, ϕ represents a variable critical for the investigation and ε is the difference between the variable ϕ of two consecutive grid resolution levels $\varepsilon_{21} = \phi_2 - \phi_1$. In the case of this thesis, it was chosen to consider the total thrust generated by the engine T_{tot} and the thrust generated by the rotor T_{rotor} as critical variables for the convergence analysis.
The engine total thrust was computed using the following equation:

$$Total\,Thrust = T_{tot} = (\dot{m}_{exit} U_{x,exit} - \dot{m}_{inlet} U_{x,inlet}) + (p_{exit} - p_{inlet})\, A_{exit} \tag{6.2}$$

As the engine lacks a core stage (i.e. the model used representative of an electric engine) the mass flow at the inlet $\dot{m}_{inlet}$ is equal to the mass flow at the exit $\dot{m}_{exit}$. The location of the surfaces can be seen in Figure 7.1. On the other hand, the thrust produced by the rotor is computed directly by the solver.

Grid Case	$\mathbf{T_{tot}}$ $[N]$	**Rel. Error** %	**GCI** %	$\mathbf{T_{rotor}}$ $[N]$	**Rel. Error** %	**GCI** %
Very Coarse	1532.2	–	–	717.6	–	
Coarse	1825.3	16.1	8.95	810.2	11.4	17.01
Medium	2023.4	9.8	5.46	830.9	2.5	3.7
Fine	2084.4	2.9	1.63	842.1	1.3	1.98

Table 6.1: Grid convergence reference parameters with the respective relative errors and GCI for each gird case

Data needed to calculate total thrust were obtained by sampling the physical quantities of the fluid on surfaces also used during the engine performance analysis (see Chapter 7) and averaging them over the entire measurement time. The same procedure was used to compute the rotor thrust. For these cases, however, quantities were sampled over the rotor blades.
The total thrust generated by the engine is a good choice for representing the

overall accuracy of the mesh since it depends on the flow parameters both inside and outside the ducted fan. The relative error between the total thrust value for the fine and medium grid levels is around 3%. Further mesh refinement would have resulted in a lower relative variance, but at the same time would have increased the simulation's computational cost. The GCI of the fines grid is $GCI_{21} = 1.62\%$. It is important that each grid level yields solutions that are in the asymptotic range of convergence for the computed solution. To do this, one can check whether two GCI values calculated for three grids are in the asymptotic range of convergence:

$$\frac{GCI_{23}}{r^p GCI_{21}} = 1.0302$$

which is approximately equal to one and indicates that the solutions are well within the asymptotic range of convergence. Figure 6.1a shows the change in the T_{tot} values for the different grid levels.

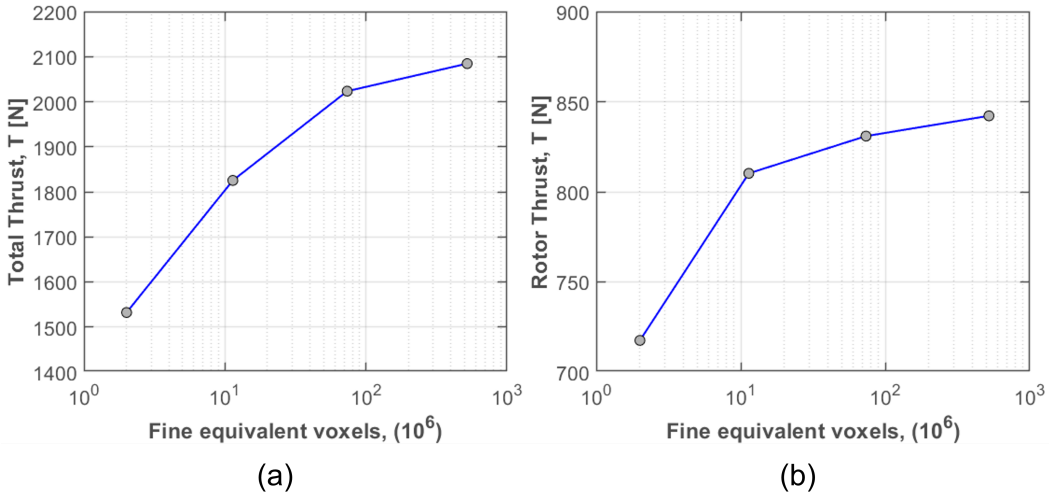

Figure 6.1: Variation of the total thrust (a) and rotor thrust (b) against the grid resolution level

Concerning the rotor thrust T_{rotor}, a relative variation of 1.3% is found between the fine and medium resolution grids. The flow field around the rotor strongly influences the thrust generated by the rotor, hence this parameter is a good choice for the accuracy of the mesh around the rotor's blades. The difference, in this case, is lower than for the total thrust analysis, the answer to these results can be found in the higher VR levels placed as offsets around the rotor blades. The GCI of the finest grid is $GCI_{21} = 1.98\%$ which is a little bit higher than the total thrust

one. Again, two GCI values are analyzed to verify that the results fall within the asymptotic range of convergence:

$$\frac{GCI_{23}}{r^p GCI_{21}} = 1.0135$$

The result indicates that the solutions are within the asymptotic range of convergence. Figure 6.1b shows the different T_{rotor} values for each grid case.

A more in-depth analysis was performed to study the variation of the static pressure on the blade as the grid resolution increases since the pressure distribution on the blade is the source of the rotor thrust value. The static pressure distribution over the blade is directly computed by the solver as for the thrust. In computing the static pressure coefficient C_p the ambient pressure $P_{ref} = 101325\,Pa$ and density $\rho_{ref} = 1.225\,kg/m^3$ together with the rotor blade tip velocity $V_{ref} = 153.13\,m/s$ were used. Figure 6.2 shows the distribution of the static pressure coefficient over the rotor blade at $r/R = 0.5$.

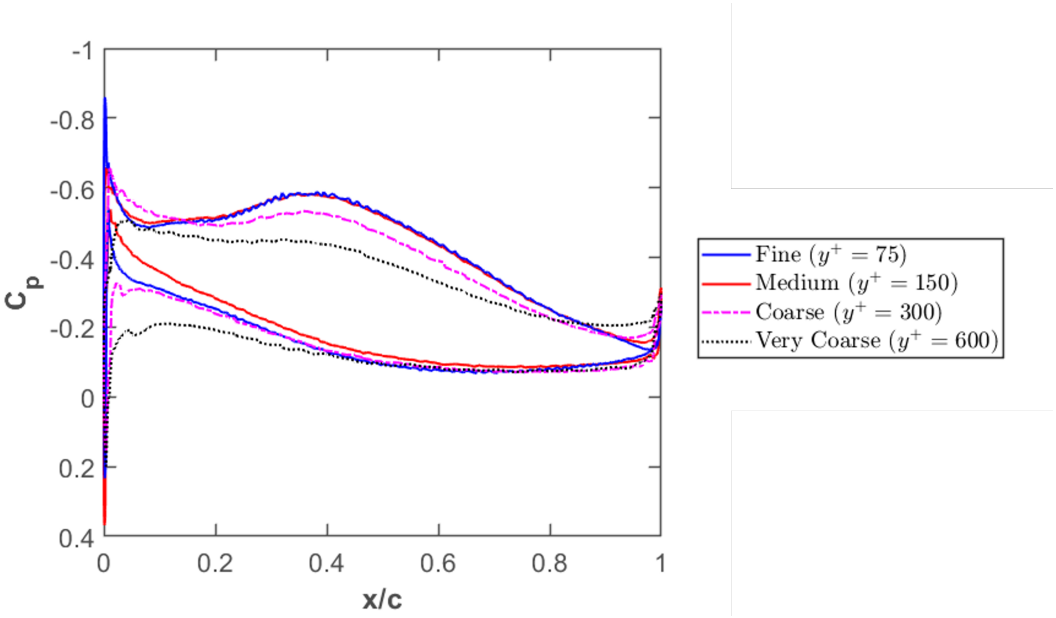

Figure 6.2: Distribution of the static pressure coefficient C_p on the rotor blade at $r/R = 0.5$

As can be seen from the figure by increasing the resolution on the rotor blades the pressure distribution is better captured. In particular for the fine and medium grid cases the higher spatial resolution allows the strong static pressure variation that characterizes the leading edge and trailing edge of the blade to be captured. In

cases where the grid is less refined these strong variations are averaged out. While the trend on the suction side of the blade is almost identical between the fine and medium cases, on the pressure side the medium grid deviates slightly from the finer grid. Finally, it is important to point out how the difference of both parameters between the coarse and medium grid is high showing a grid dependence of the results. The choice of using the Coarse grid level for the performance analysis is not correct because of the large difference with the finest grid level. However, as the purpose of the investigation is to obtain a general trend, the choice can be justified.

Chapter 7

Engine performance analysis

The following chapter presents the CFD investigation carried out to analyze the influence of the nozzle exit area on engine performance. The purpose of this first stage of the thesis was to understand the global trend of the engine performance while the parameter of interest was changed, thus, to reduce the computational cost and the total time required to complete the analyses, the coarse mesh was chosen (see Table 5.5). Analyses were performed for the 4 configurations presented in Section 5.1.2, for each 3 engine operating conditions were simulated: 100% power which is equivalent to 5344 RPM, 80% power which is equivalent to 4275 RPM and 60% power which is equivalent to 3206 RPM for s total of 12 simulations.
Following the results, two cases were selected for the aeroacoustics analysis based on the relevance of their fluid-dynamic field.
The chapter is divided into the following sections:

- **Section 7.1**: The performance maps are displayed and discussed
- **Section 7.2**: The flow field which characterizes the different cases is analyzed and velocity profiles are plotted.
- **Section 7.3**: The forces generated by the different configurations are computed and discussed
- **Section 7.4**: A summary of the main fluid-dynamic features of the configurations is provided. Also, the two cases for the aeroacoustics analysis are chosen.

7.1 Performance maps

To evaluate the engine's performance, 4 surfaces have been placed inside the engine at key points of the engine, respectively Inlet, Interstage, Stage and Exit. For each surface flow properties were sampled and averaged over an interval equal to 6 full rotations. In Figure 7.1 the locations of each surface are shown. While the Inlet,

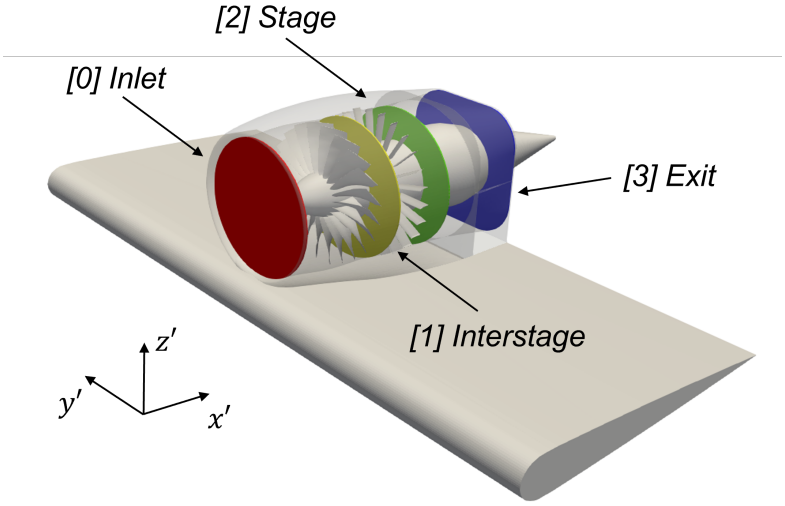

Figure 7.1: Location of the 4 surfaces

Interstage and Stage surfaces are placed in the same position for each configuration, the Exit surface position depends on the nozzle configuration. Referring to the Fan Coordinate System Table 7.1 defines the location of the surfaces.

Surface	Position
Inlet	$x' = -R_{rotor}$
Interstage	$x' = 0.1013\,m$
Stage	$x' = 0.3215\,m$
Exit	Configuration dependent

Table 7.1: Position of the different surfaces with respect to the Fan coordinate system

A performance map is a plot of the measured performance parameters as a function of the mass flow elaborated by the engine. Since the ducted fan consists

of a rotor and a stator, the overall performance is affected by the coupling of the two elements. Therefore, the performance parameters were calculated relative to the stage (surface behind both rotor and stator). Stage total pressure ratio and stage adiabatic efficiency are presented in Figure 7.2.

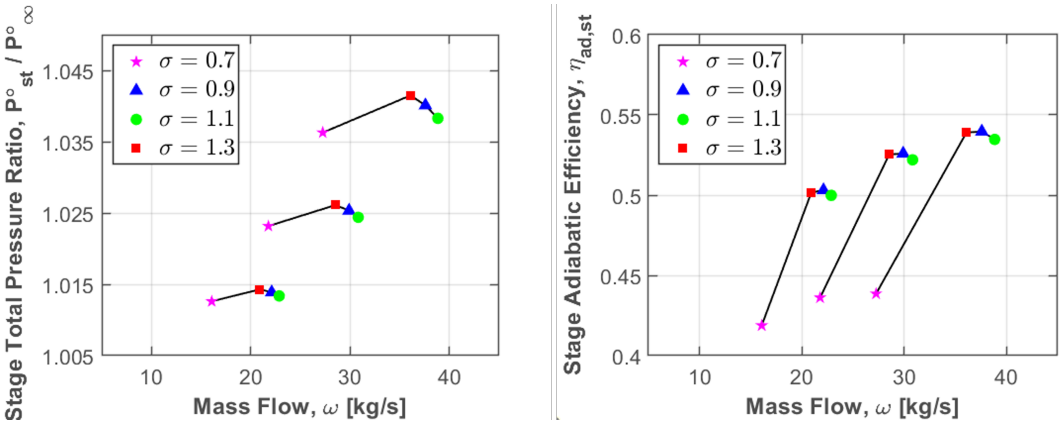

Figure 7.2: Engine performance maps

The adiabatic stage efficiency is defined as follows:

$$\eta_{ad,stage} = \frac{\left(\frac{P^\circ{}_{stage}}{P^\circ{}_\infty}\right)^{\frac{(\gamma-1)}{\gamma}} - 1}{\left(\frac{T^\circ{}_{stage}}{T^\circ{}_\infty}\right) - 1} \tag{7.1}$$

It takes into account the total pressure jump generated by the stage (numerator) and relates it to the ratio of the total temperatures. The mass flow is a measure of the amount of fluid flowing through a section of area A in the unit of time. and is defined as:

$$\omega = \rho A V \tag{7.2}$$

There is a substantial difference in performance between the $\sigma = 0.7$ case and the other three cases which occurs for all three engine settings. From the adiabatic efficiency results, it is clear that in the $\sigma = 0.7$ configuration the engine is working in a different condition which is negatively affecting its performance. For all the three RPM settings the adiabatic efficiency of this case is about 10% lower than the others. As expected the mass flow increases as the RPM increases. However, the change in mass flow does not follow the increase in the exit area. In particular, when the area ratio is increased from $\sigma = 1.1$ to $\sigma = 1.3$ the mass flow decreases pointing out the establishment of a phenomenon which affects the amount of flow processed by the engine.
To more directly compare the engine performance between the nozzle configurations, a loss coefficient for total pressure was defined. This parameter was used as a

measure of the performance drop across the different locations of the engine, as a percentage. In the case of the performance drop between rotor and stator, the coefficient is defined as follows:

$$Loss\,Coefficient = \frac{(P^{\circ}{}_{interstage} - P^{\circ}{}_{stage})}{P^{\circ}{}_{interstage}} \cdot 100 \tag{7.3}$$

while in the case of the performance drop between the stator and the exit as:

$$Loss\,Coefficient = \frac{(P^{\circ}{}_{stage} - P^{\circ}{}_{exit})}{P^{\circ}{}_{stage}} \cdot 100 \tag{7.4}$$

Figure 7.3 the two Loss coefficients are plotted versus the three engine operating conditions $N/N_{100\%}$ for each of the four nozzle positions. For all the configurations the stator loss coefficient increases as the rotational speed of the rotor rises. While for the cases $\sigma = 0.9/1.1/1.3$ the trend seems similar, for the $\sigma = 0.7$ case losses between operating conditions are greater. When comparing the results for the same rotational speed, it is clear that the $\sigma = 0.7$ features the greatest losses. This result suggests that the stator is operating in a worse condition in comparison with other cases. The flow in the fan wake is generally a swirl flow characterized by a high radial velocity component which reduces the thrust generated by the engine. To convert the kinetic energy of the swirling flow into additional thrust a stator is placed downstream of the fan. As stators are designed to work efficiently within a certain range of angles of attack (AOA) when the oncoming flow has a different AOA separation and thus losses can occur.

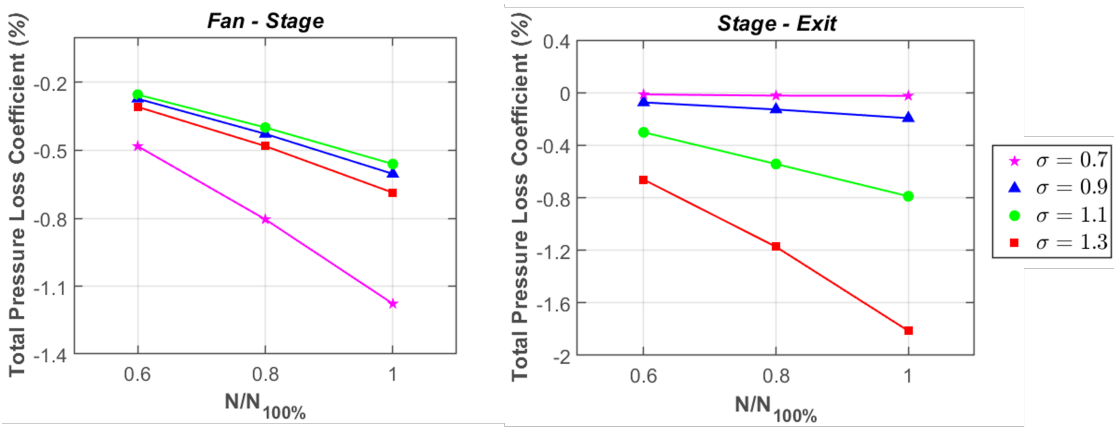

(a) Stator total pressure drop

(b) Nozzle total pressure drop

Figure 7.3: Loss coefficient for the stator and the nozzle

Another important result can be obtained from the trend shown by the total

pressure losses observed in the duct section between the stator and the outlet (Figure 7.3 b). For the cases where the exit area is increased ($\sigma = 1.1$ and $\sigma = 1.3$) the total pressure drop in the variable section of the duct is higher while for the other two cases the losses are small or absent. By plotting the axial velocity variation across the 4 locations defined in Figure 7.1 the situation becomes clearer. As expected the flow is accelerated by the pressure jump generated across the rotor disk by the fan. After the stator location, however, the axial flow velocity is reduced for the cases $\sigma = 0.9/1.1/1.3$. Indeed, as the inner duct of the engine diverges, the velocity decreases while for the $\sigma = 0.7$ configuration where the inner duct converges the velocity increases resulting in a total pressure drop of almost zero. The high deflection angle of the duct caused by the nozzle rotation present in the cases $\sigma = 1.1$ and $\sigma = 1.3$ induces flow separation which is responsible for losses localized in this part of the ducted fan. The nozzle separation plays a key role in determining the amount of flux the propulsion system processes since the continuity condition must be met in every section of it. Hence, the axial flow velocity magnitude is also impacted by what happens at the engine exit. In the $\sigma = 0.7$ case as the engine internal duct is reduced by the variable nozzle position results in the establishment of a pressure field that reduces the amount of flow being processed by the engine and as is visible in Figure 7.4 also the axial velocity in the different sections of the engine.

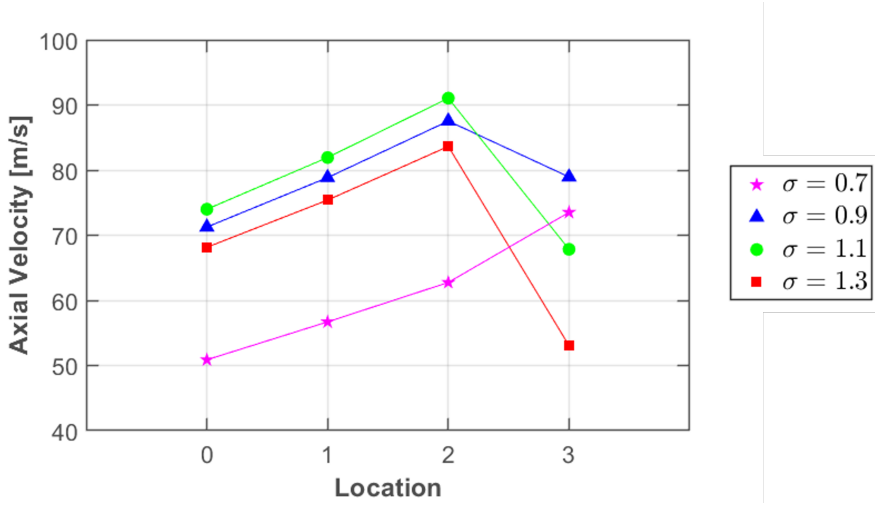

Figure 7.4: Axial velocity at the location defined in 7.1

7.2 Flow field

The flow field of the configuration is extremely complicated. Furthermore, the four nozzle configurations exhibit phenomenologies that are globally similar but different in magnitude or completely different phenomena. To better visualize the behaviour of the engine and the flow separation, the total pressure coefficient is defined as,

$$C_{p_{tot}} = \frac{P^{\circ} - P^{\circ}_{\infty}}{\frac{1}{2}\rho_{\infty} V_{tip}^2} \tag{7.5}$$

was plotted on a plane normal to the Y direction (with respect to the fan coordinate system) that cuts the engine symmetrically (Figure 7.5) for the 100% power setting (5344 RPM). The total pressure coefficient is defined with respect to the blade tip velocity V_{tip}.

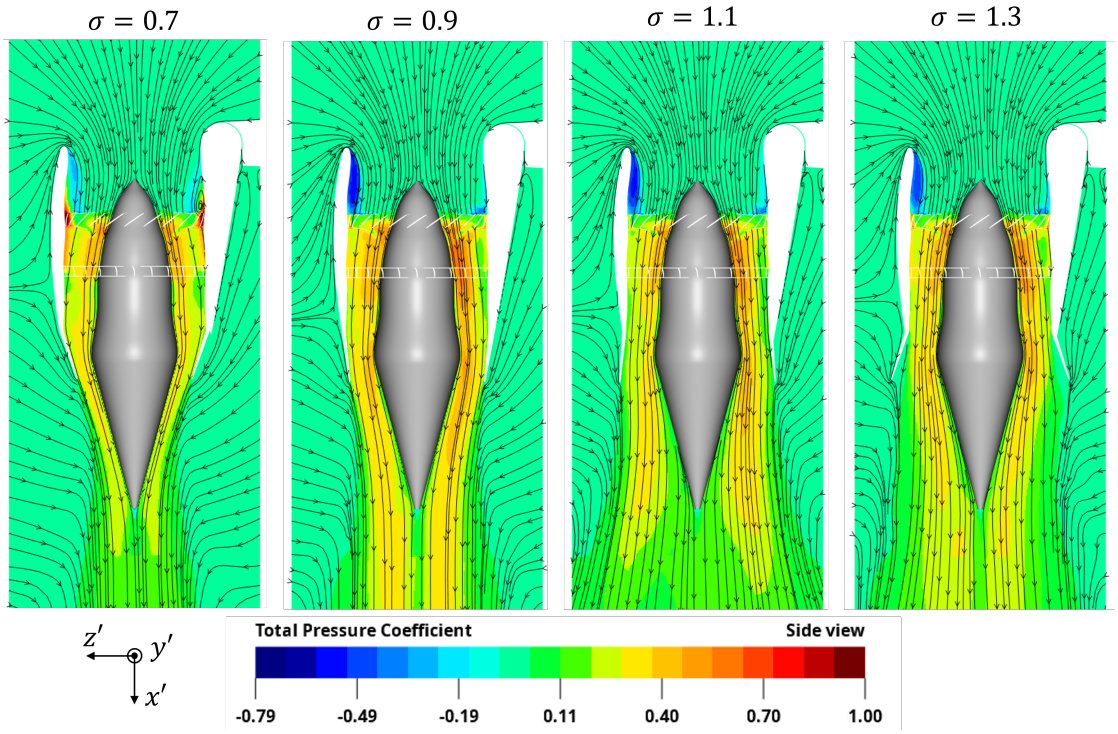

Figure 7.5: Distributions of the total pressure coefficients for the 4 cases at 100% power engine setting

As already introduced in Section 5.1 the engine design is not optimized for this type of application, thus the engine is expected to work in off-design conditions. The big inlet separation is evidence of this state. As the investigation has been carried out considering a hover condition the flow around the engine (which is

essentially stationary) is forced inside the engine duct. While the streamlines on the wing side of the engine are more guided thanks to the small curvature, on the nacelle side the high curvature induces streamlines distortion and subsequent flow separation (represented by the dark blue area visible in the figures). This results in an engine breathing area reduction and thus in a lower mass flow elaborated with respect to the ideal value.
The presence of the separation bubble also acts as a fluid surface which induces two main effects on the flow. First, it causes an asymmetry in the flow processed by the two sides of the engine in the Z direction. Namely, the wing side sees a higher magnitude of mass flow than the nacelle side. Instead, the flow maintains its symmetry in a plane normal to Z that passes through the ducted fan's axis of symmetry (along the Y-axis). The two velocity profiles are presented respectively in Figure 7.6 a and b.
The second effect of the separated flow bubble is the acceleration of the flow. On the wing side of the engine, the flow is guided by the small curvature radius that causes the fluid to stay attached to the wall. The axial velocity profile in this region is thus uniform with a constant value located at the centre of the area between the nacelle wall and the hub wall (7.6 c negative side z/R). Separate flow, on the other hand, cause the incoming flow to move through an area that is reducing, thereby resulting in an acceleration. The axial velocity is therefore characterized by a pick value at around $z/R = 0.8$ in the Z direction (7.6 c) and $y/R = \pm 0.8$ in the Y direction, in other words near the separated flow. In the y direction, the symmetry is preserved while in the z direction is not. The $\sigma = 1.1$ case still features the higher axial velocity value, slightly larger than the other two cases, whereas the lower value is found for the $\sigma = 0.7$ case. The line along which the velocity values have been recorded and plotted crosses the hub starting from the $x = R_{rotor}/2$ location, resulting in the absence of data near the centre of the duct.
A further observation is that the rotor blades fail to process the fluid properly near the wall, at a location equal to $r/R = 90 - 95\%$ of the blade radius. The reason for this effect is that, at this location, the separated flow coming from the inlet lip is characterized by a high radial velocity component resulting in a high angle of attack experienced by the blades. For the $\sigma = 0.7$ case, rotor blades are essentially stalled at this distance and can not process the flow. For the other three cases, the situation is similar, however, the smaller separation bubble and lower radial component help the rotor blade to work at lower AOA starting from a distance closer to the blade tip compared to the $\sigma = 0.7$ case.
Regions of reduced total pressure coefficient are therefore located behind the rotor at the same location where the blades are stalled (as can be seen in Figure 7.5). For the same reason, a significant lower axial velocity can be found at the inter-stage location for the $\sigma = 0.7$ case, evidencing the worst condition in which the rotor

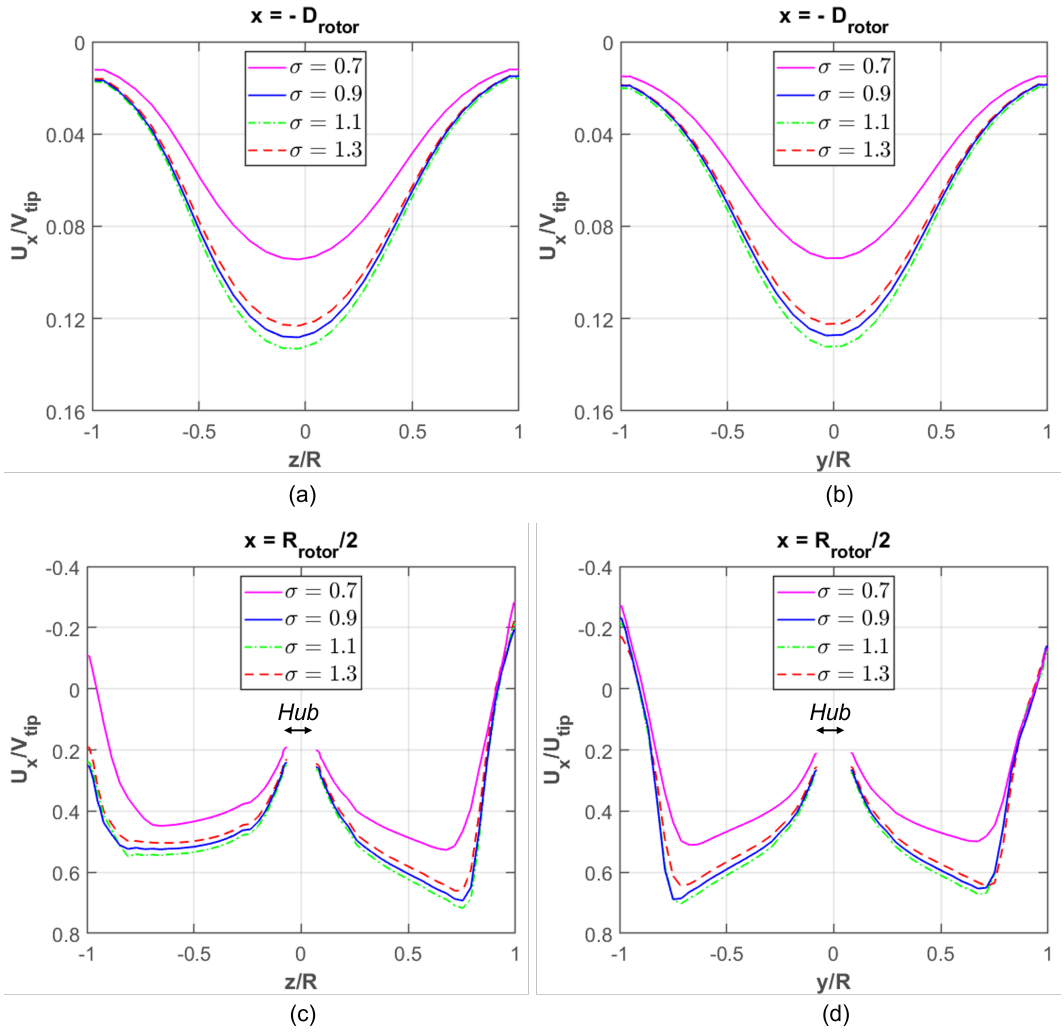

Figure 7.6: Normalized axial velocity respectively at $x' = -D_{rotor}$ (a and b) and $x' = R_{rotor}/2$ (c and d)

works. Axial velocity at this location is shown in figure 7.7. The total pressure and axial velocity highest value are thus shifted around $r/R = 50\%$ and near the hub. The radial velocity components of the flow U_y and U_z at a distance equal to $x = R_{radius}/2$ (with respect to the fan coordinate system) in front of the rotor are displayed in Figure 7.8. In the Y direction the symmetry (Figure 7.8 b) can be still observed. The radial velocity component U_z in the $\sigma = 0.7$ case has a maximum located near the nacelle wall that is around 50% higher than in the other 3 cases. The velocity values near the nacelle do not return to zero as expected in reality, this depends on the application of a Wall Function in the boundary layer modelling

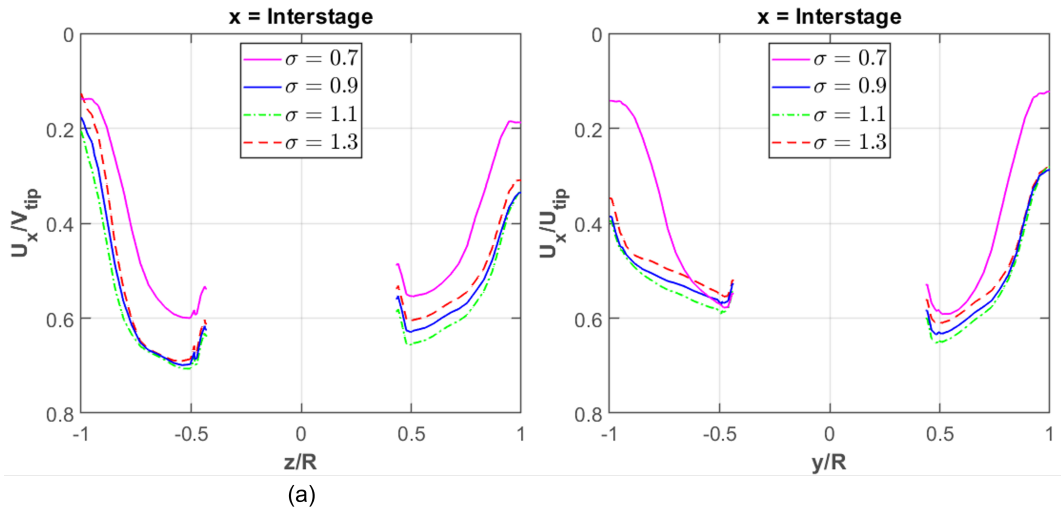

Figure 7.7: Normalized axial velocity at $x = 0.1013\,m$ = Interstage (see Table 7.1

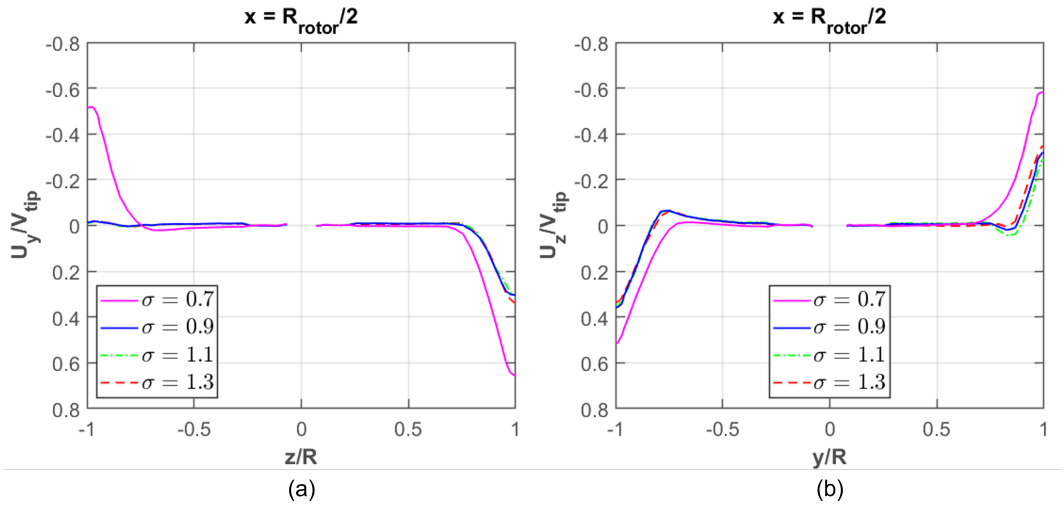

Figure 7.8: Normalized radial velocity at $x = R_{rotor}/2$

(as described in Section 4.3.1).
For the cases $\sigma = 0.9/1.1/1.3$ the plot of the radial velocity in the Z direction (7.8 a) shows how the flow is guided by the wing wall resulting in the total absence of radial component. On the other hand, in $\sigma = 0.7$ case the flow is marked by a high radial component which is also found near the wing wall and it is twice as high as in the other cases analyzed.

Based on the results, it was verified that the geometry of the internal engine

duct (and thus the exit area ratio) strongly influences the fluid field of the analyzed configurations. In the $\sigma = 0.7$ case the convergent geometry produced by the nozzle rotation results in a high-pressure region which affects the flow processed by the engine. The pressure field is outlined by plotting the distribution of the static pressure coefficient inside the engine which is defined as:

$$C_p = \frac{P - P_\infty}{\frac{1}{2}\,\rho\, V_{tip}^2} \tag{7.6}$$

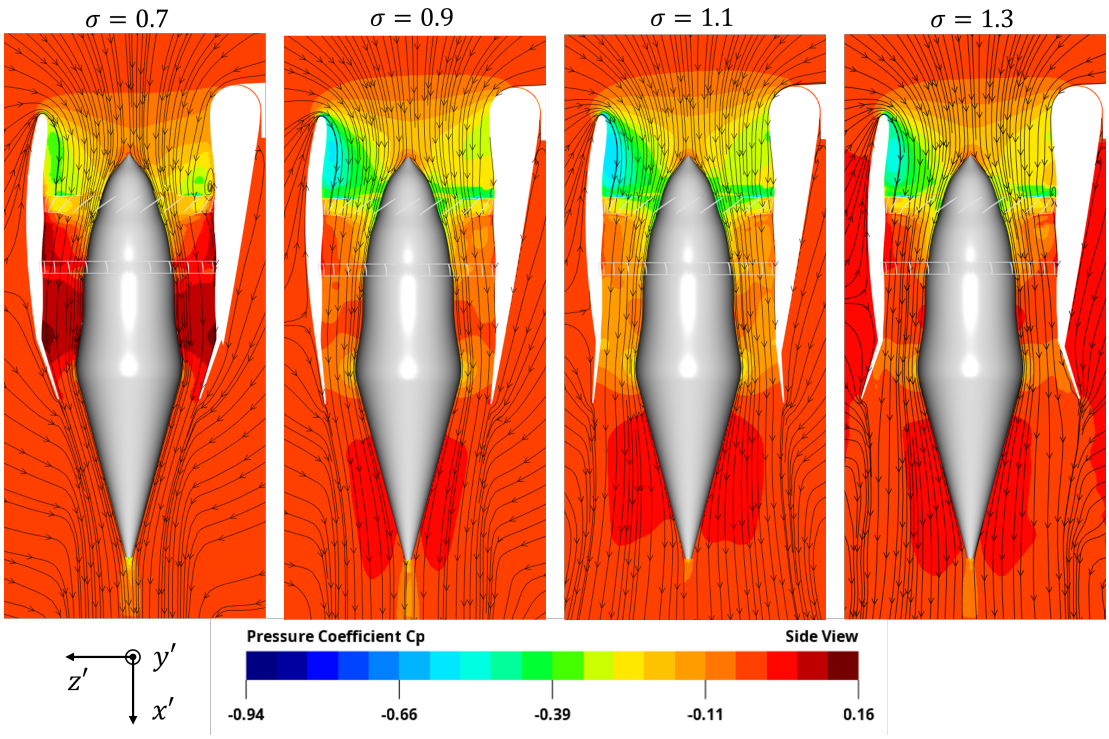

Figure 7.9: Distributions of the static pressure coefficients for the 4 cases at 100% power engine setting

As expected, the high-pressure region is located near the nozzle axis of rotation. The high-pressure act as a barrier that the fluid has to overcome, thus increasing the work the rotor must perform to achieve the same performance as other conditions. For the other nozzle configuration as the high-pressure region is not here the flow processed by the engine does not experience the same level of influence. However, the flow separation induced by a high nozzle divergence angle limits the mass flow. A more in-depth consideration of this effect is resent in the section 7.4.

7.3 Thrust measurements

Following the analysis of the fluid field, the thrust produced by the engine has been computed to complete the performance investigation.
The ducted fan total thrust has been computed using the following equation.

$$Total\,Thrust = T_{tot} = \underbrace{(\dot{m}_{exit}U_{x,exit} - \dot{m}_{inlet}U_{x,inlet})}_{Gross\,Momentum} + \underbrace{(p_{exit} - p_{inlet})\,A_{exit}}_{Pressure} \quad (7.7)$$

The thrust can be divided into two contributions:

- **Gross momentum thrust contribution**: which depends only on the axial velocity difference between the average axial velocity U_x at the ducted fan inlet and that at the outlet.
- **Pressure contribution**: which is due to the difference between the averaged static pressure at the exit and inlet of the engine with respect to the exit area A_{exit}

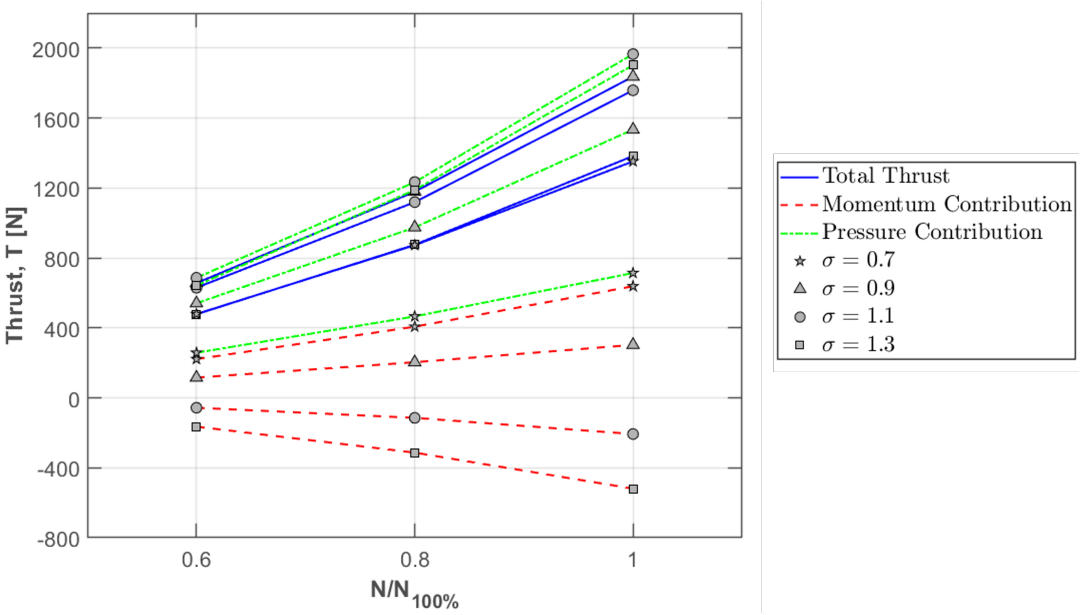

Figure 7.10: Variation of total thrust and its two contributions for the 4 cases at 3 different engine settings: $100\%, 80\%, 60\%$ of the maximum power condition 5344 RPM

The data used for the thrust calculation were obtained in the same way that the data from the performance maps and fluid dynamic field analyses were calculated,

i.e., by averaging the variables sampled on the surfaces shown in Figure 7.1 over a time equal to 6 rotations.
The influence of the exit area ratio over the engine total thrust is visible when the two thrust contributions are plotted individually. For the cases $\sigma = 1.1$ and $\sigma = 1.3$ where the exit velocity is decreased by the fluid dynamic phenomena previously discussed in Section 7.2, the momentum contributes negatively to the total thrust as the exit axial velocity is lower than the inlet axial velocity. For cases $\sigma = 0.7$ and $\sigma = 0.9$, on the other hand, the contribution is positive and the highest contribution occurs for the 0.7 case where the flow is re-accelerated by the converging duct. The largest contribution to the total thrust for all 4 cases is made by the pressure. In this case, the configuration where the exit area is increased makes a larger impact on the produced thrust, thus balancing the previous negative contribution.
Overall the $\sigma = 0.9$ produce the highest thrust around 1800 N followed by the $\sigma = 1.1$ case with about 1700 N, while cases $\sigma = 0.7$ and $\sigma = 1.3$ produce about the same thrust but with a 22% reduction.

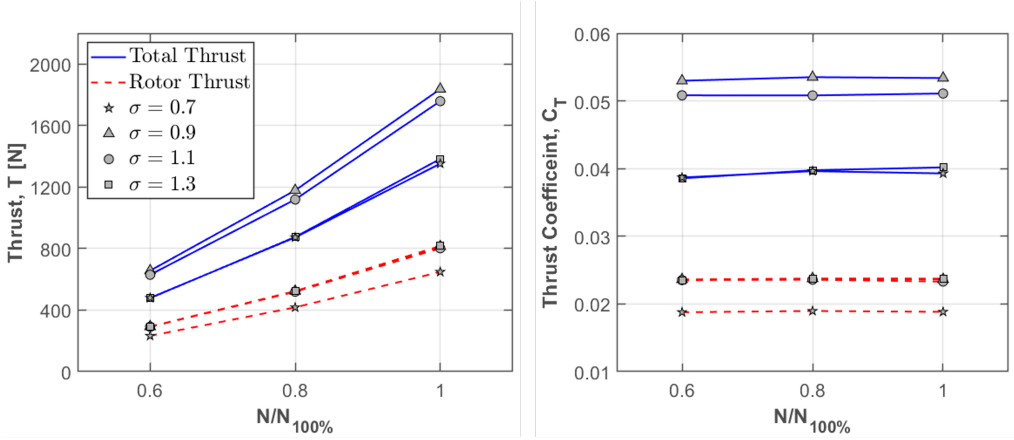

(a) Rotor thrust contribution to the total thrust

(b) Thrust coefficient

Figure 7.11: Rotor thrust contribution and thrust coefficient C_T for the 4 cases at 3 different engine settings (100%, 80%, 60% of the maximum power condition 5344 RPM)

The total thrust produced by a ducted fan can be also seen as consisting of the rotor alone contribution and a duct contribution as described in Chapter 2. By highlighting the thrust produced by the rotor the difference between the condition in which the rotor itself is working in the different conditions is clear. The thrust produced by the rotor in the $\sigma = 0.7$ case is lower for each engine setting, as the rotational speed increases, the difference in the thrust produced by the $\sigma = 0.7$ case

and the others increases. This result supports the findings of the fluid field analysis showing that with a closed nozzle the engine is working in the worst condition.

In Figure 7.11 the thrust coefficient is defined as,

$$C_T = \frac{T}{\rho\, D^4\, \Omega^2} \tag{7.8}$$

Finally, the Figure of Merit was computed as a measure of the ducted fan efficiency in hover as also done in other similar investigations [8]. For a ducted fan the Figure of Merit can be proven to be defined as:

$$M = \frac{C_T^{\frac{3}{2}}}{\sqrt{2}\, C_P} \tag{7.9}$$

where C_T is the Thrust Coefficient defined in 7.8 while C_P is the Power Coefficient which has been calculated starting from the torque τ produced by the rotor:

$$C_P = \frac{P}{\rho\, D^5\, \Omega^3} = \frac{\tau\, \Omega}{\rho\, D^5\, \Omega^3} \tag{7.10}$$

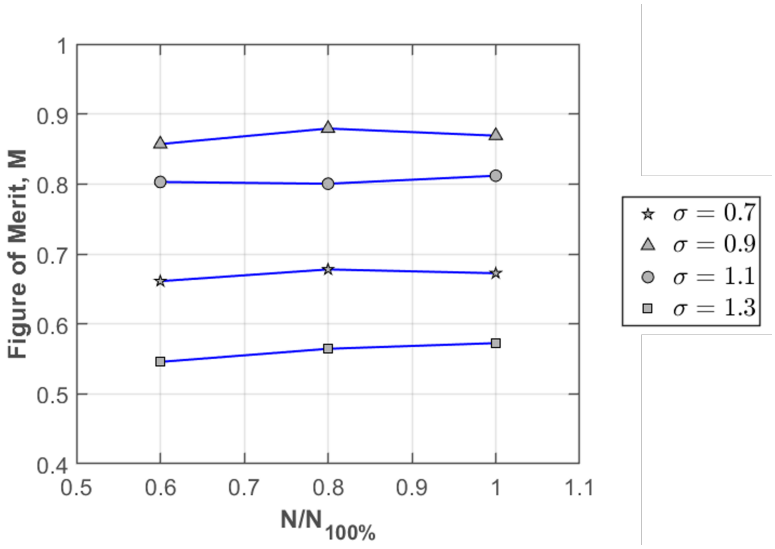

Figure 7.12: Figure of Merit

7.4 Key Findings

The Chapter presented and discussed the results of the engine performance analysis. The investigation of engine performance and the fluid dynamics phenomena that distinguish the different configurations among the others was necessary for the selection of the cases of greatest interest for acoustic analysis and to obtain a comprehensive understanding of the fluid dynamic field of the engine. Based on the results of the numerical simulations, it was found that changes in the exit surface area ratio are strongly correlated with changes in the internal fluid dynamics of the engine, thus impacting its performance. In general, three scenarios can be defined:

1. **Convergent exit duct ($\sigma = 0.7$)**: When the variable nozzle is set in a configuration which leads to a convergent internal duct (at the engine exit) the flow is re-accelerated by the geometry. As a result, the flow exit velocity is kept high. However, the sudden area reduction results in the establishment of a high-pressure zone which acts as a barrier. Since the engine is operating in subsonic conditions, the incoming flow is affected by this high-pressure region. The processed mass flow as well as the inlet axial velocity are reduced and the rotor is found to operate in a non-optimal condition. The nozzle blockage effect stalls the flow near the nacelle wall in front of the rotor, which then struggles to process a flow with a high radial velocity component. Thus, the rotor's thrust is reduced and the blades' loading is asymmetric. In addition, high losses are generated behind the stator due to flow separation which is induced by the high angle of attack that the incoming flow has.

2. **Linear exit duct ($\sigma = 0.9$ / $\sigma = 1.1$)**: In the case of a variable nozzle which is set in a configuration that does not block the flow and allows it to stay attached to the nacelle walls, hence limiting losses at the exit the engine is found to be more efficient in terms of produced thrust and Figure of Merit. As shown in figure 7.12, cases $\sigma = 0.9$ and $\sigma = 1.1$ show the highest Figure of Merit values which have been used as a Hover efficiency parameter. Also, both cases produce the highest value of thrust among the 4 configurations. In this case, the flow field is therefore mainly affected by the inlet separation which, however, can not be eliminated as it is caused by the nacelle design. Since the nacelle design point is the cruise phase, the inlet lip separation is probably a characteristic phenomenon of this type of architecture that can only be mitigated. Taking a closer look at the two cases, it can be seen that the very small difference between their performances can only be attributed to the difference in axial exit velocity. To maximize thrust and performance, it is important to minimize the loss of axial velocity in the nozzle.

3. **Divergent exit duct ($\sigma = 1.3$)**: Although no investigations have been done

of the 4 configurations in the cruise phase, it is possible to claim that the engine performs better with the variable nozzle in an "open" configuration rather than in a "closed" one. However, it was possible to find a limit in the area ratio of the engine beyond which the beneficial effect vanishes and a negative effect arises. Case $\sigma = 1.3$ results show that when the divergence angle of the variable nozzle is too high, flow separation occurs inside the nozzle. Separation induces a smaller exit area (compared to what it would be in the case of attached flow) that affects the processed mass flow. It also results in a lower exit axial velocity and high losses. The limit is reached when the separation starts at the nozzle rotation point. Once reached the limit, which depends upon the engine design, and keeping the same RPM, a further increase in the exit area ratio (i.e. nozzle rotation) does not bring any effect to engine performance.

According to the results discussed in the chapter, the cases $\sigma = 0.7$ and $\sigma = 0.9$ have been selected for the high-fidelity computational analysis, as they represent the cases of greatest interest. A far-field aeroacoustic investigation of the two configurations has been carried out based on the fluid field data obtained from the high-resolution simulation. Results are reported in Chapter 8.

Chapter 8

High-fidelity simulation results

In this chapter the aerodynamic and acoustic results obtained from the high-resolution simulations of the two configuration are compared and discussed. The chapter is divided into three sections. Sections 8.1 and 8.2 report the aerodynamic results in terms of engine performance and flow field analysis. Section 8.3 discusses the aeroacoustic results.

8.1 Engine performance

Performance results for the two engine configurations are presented in Table 8.1. The data were extracted following the same procedure applied in low-fidelity analysis (see Chapter 7).
In line with previous analyses, the engine is found to generate more thrust in the configuration with an exit area ratio of $\sigma = 0.9$ than in the $\sigma = 0.7$ configuration. The stage adiabatic efficiency η_{stage} is also 5% higher, emphasizing that the engine is operating more efficiently. As already discussed, total thrust T_{tot} is composed of

Configuration	**Mass flow** $[kg/s]$	$\mathbf{T_{tot}}$ $[N]$	$\mathbf{T_{tot_p}}$ $[N]$	$\mathbf{T_{tot_m}}$ $[N]$	$\mathbf{T_{rotor}}$ $[N]$	$\eta_{\mathbf{stage}}$ $[-]$
$\sigma = \mathbf{0.9}$	39.2	2084.4	1772.7	311.7	842.1	0.53
$\sigma = \mathbf{0.7}$	32.9	1716.8	903.6	813.2	800.3	0.48

Table 8.1: Performance data of the two engine configurations

two contribution: the *Gross momentum contribution* and the *Pressure contribution*. For the baseline case, the two contributions represents the 85% and 15% of the

total thrust. For the closed configuration, on the other hand, they contribute approximately to the 53% and 47%. The result is interesting and proves what has already been found. While the more closed configuration produces a greater jump in velocity, the reduced exit area does not produce the same thrust component as when the nozzle is more widely open. Moreover, although the mass flux is affected by the reduced exit area, the momentum contribution of the $\sigma = 0.7$ configuration is higher. The beneficial effect of the duct is evident and reflects what was found during the literature review. Figure 8.1 shows how the axial flow

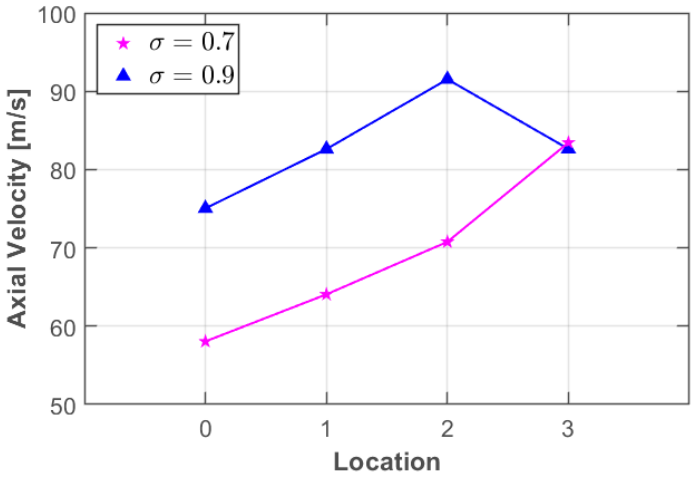

Figure 8.1: Axial velocity values in 4 locations inside the engine duct

of the two configurations change along the x' axis of the Fan coordinate system in 4 locations (see Figure 7.1 for more information about the surfaces location). The two configurations share approximately the same exit velocity, however the velocity jump produced by the $\sigma = 0.7$ case is higher as the inlet axial velocity is lower. This justifies the higher component of thrust related to Gross momentum in the $\sigma = 0.7$ case.
As the results do not give any more information than what was already found in the performance analysis, it was preferred to focus on the characteristics of the flow field.

8.2 Flow field

As shown in Chapter 7 the flow field of the ducted fan model is complex. The aerodynamic characteristics are influenced by several fluid-dynamic phenomena. To determine which phenomena most influence the engine's acoustic footprint, the characteristics of mean flow and instantaneous flow are examined. results on mean

flow reflect what has already been found in the low-resolution analyses, the main effects, however, are resumed for completeness of the following discussion.

8.2.1 Mean Flow

Measurements of physical quantities were averaged over 6 rotations to obtain the average flux discussed in this section. First, to get an overall view of the flow field, the total pressure coefficient of the two configurations is analyzed on the $y' = 0$ symmetry plane. Flow separation at the inner lip of the nacelle is visible as already found in the previous investigation. It is represented by the negative total pressure coefficient zone (in dark blue) visible in Figure 8.2. The inlet separation is caused by the high contraction that the flow experiences moving from a stationary condition around the engine to the low-pressure zone generated by the rotor. A higher nacelle inlet lip can help, however, the nacelle is designed to work properly in the longest phase of the mission, the cruise. Therefore it is challenging to find a trade-off design which can work properly in both cruise and hover. The rotating section of the wing on which the engine lies guides the flow without leading to strong contractions, thus delaying flow separation.

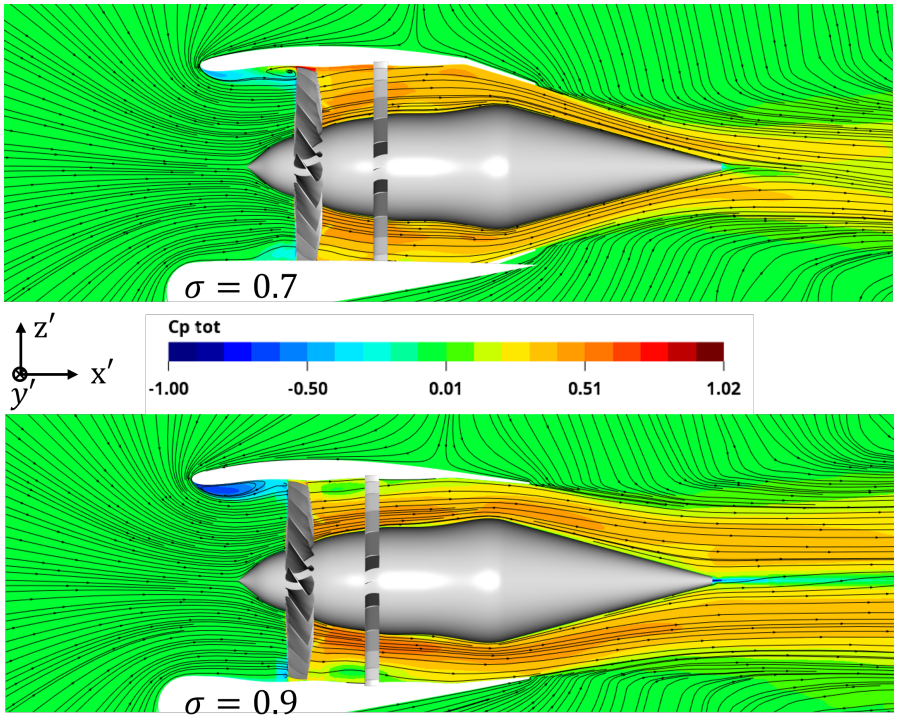

Figure 8.2: Visualization of the Total pressure coefficient Cp_{tot}, symmetry plane XZ

For case, $\sigma = 0.9$ the separation on the flow side of the nacelle is stronger on average. Moreover, behind the rotor a low total pressure coefficient region is found for $\sigma = 0.9$ case and not for the $\sigma = 0.7$ one. This effect will be covered more in detail during the discussion of instantaneous flow characteristics. On the other side, for the latter, a negative Cp_{tot} region is found in front of the rotor on the wing side of the engine. The inlet separation results in two effects:

- An asymmetry in the flow processed by the rotor (between the two sides of the engine duct)
- Ingestion of turbulent flow

The first effect can be visualized by plotting the axial velocity profile in front of the rotor at a distance equal to $x' = R_{rotor}/2$ from the Fan coordinate system centre. The separated flow act like a convergent wall inducing an acceleration in the upper

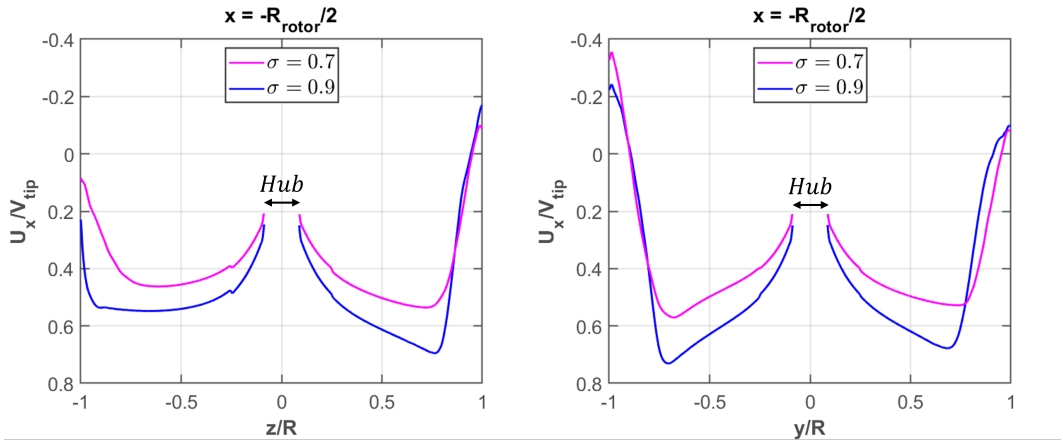

(a) (b)

Figure 8.3: Axial velocity profiles in the z' (a) and y' (b) direction for the two configurations at $x' = -R_{rotor}/2$

part of the engine with a maximum value near the nacelle surface while on the wing side of the duct the axial velocity profile is quite flat at the core. The same effect is found on the y axis where however the flow symmetry is still appreciable. Processing an asymmetric flow, on the other hand, involves large fluctuations of forces on both the rotor and stator and thus vibrations that strongly affect the noise level produced.
The flux behind the rotor shows a high Cp_{tot} value around a blade radius position of $r/R = 0.5$ as expected. However, Baseline case values are higher than those found for the 0.7 case, verifying that the rotor in this configuration produces slightly

more thrust.
As shown in figure 8.3 the axial velocity of the $\sigma = 0.9$ case is higher than in the $\sigma = 0.7$ one in all the sections of the engine except for the nozzle. Here, the divergent area of the baseline configuration slows the flow down, while the convergent area of the 0.7 model speeds it up so reaching the same velocity at the exit. The lower axial velocity and mass flow processed by the engine is determined by the reduced outlet area, which, as already seen, results in a zone of high pressure near the nozzle axis of rotation that acts as a barrier affecting the inlet flow. As the literature review revealed [16], this effect may be due to a suboptimal engine operating condition. By increasing the rotational speed (RPM) of the rotor, this effect may vanish bringing the engine into a more efficient operating condition.
Looking at the radial velocity profile at the same location determines how the

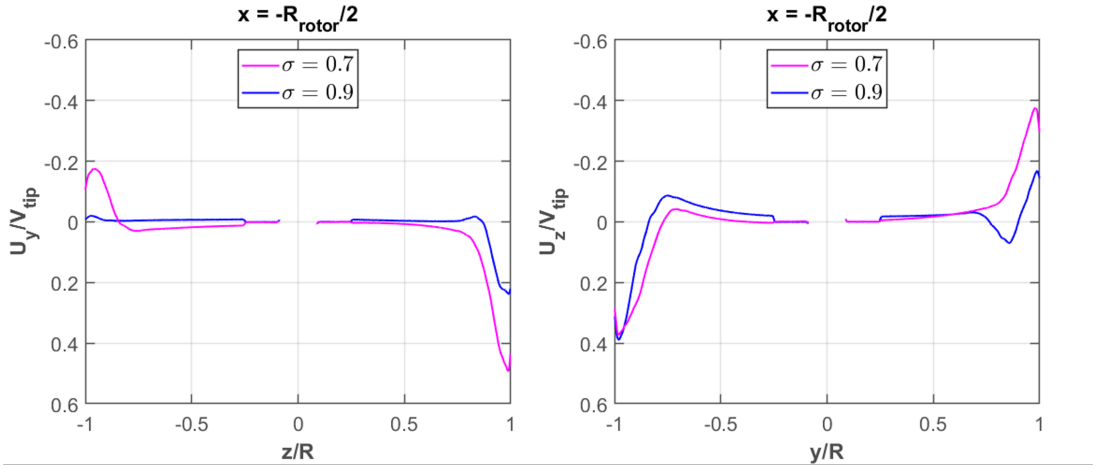

(*a*) (*b*)

Figure 8.4: Radial velocity profiles in the z' (a) and y' (b) direction for the two configurations at $x' = -R_{rotor}/2$

stagnation bubble determined in the low-resolution analyses is no longer present. The higher resolution thus allowed for a better representation of the fluid properties near the nacelle. Nevertheless, the flow in $\sigma = 0.7$ case has a larger radial component than that found in $\sigma = 0.9$ case as shown in Fig. 8.4. In the z-direction, a zero radial velocity value is determined in the 0.9 on the nacelle wing side, while non-zero in the 0.7 cases thereby supporting the presence of a turbulent zone.
Finally, to verify the performance of the stator, the radial velocity components before and after its location are compared. Velocity profiles are plotted in the y' (Fig. 8.5) and z' (Fig. 8.6) directions of the Fan coordinate system.
It is evident from the profiles that the flow behind the rotor is marked by a high radial component determined by the rotation. For the $\sigma = 0.7$ case the radial

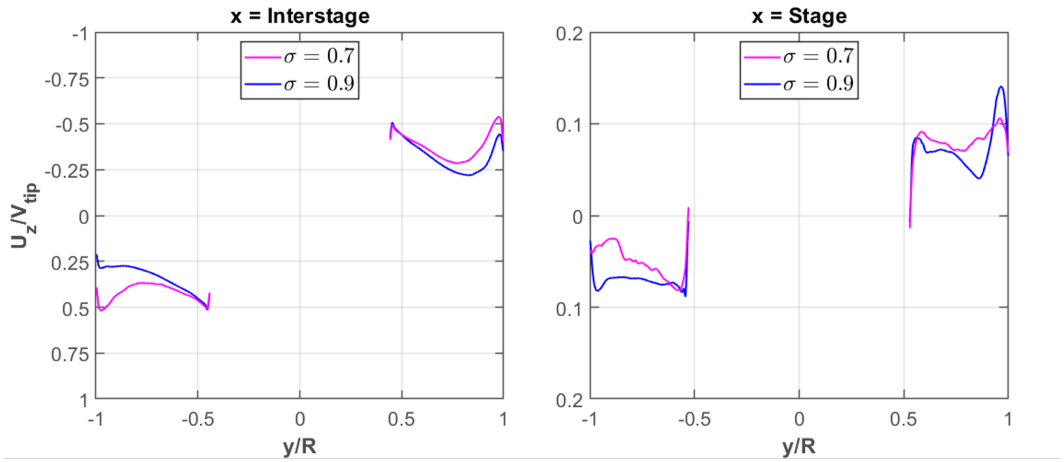

Figure 8.5: Radial velocity component, y' direction at $x' = 0.101\,m$ and $x' = 0.321\,m$

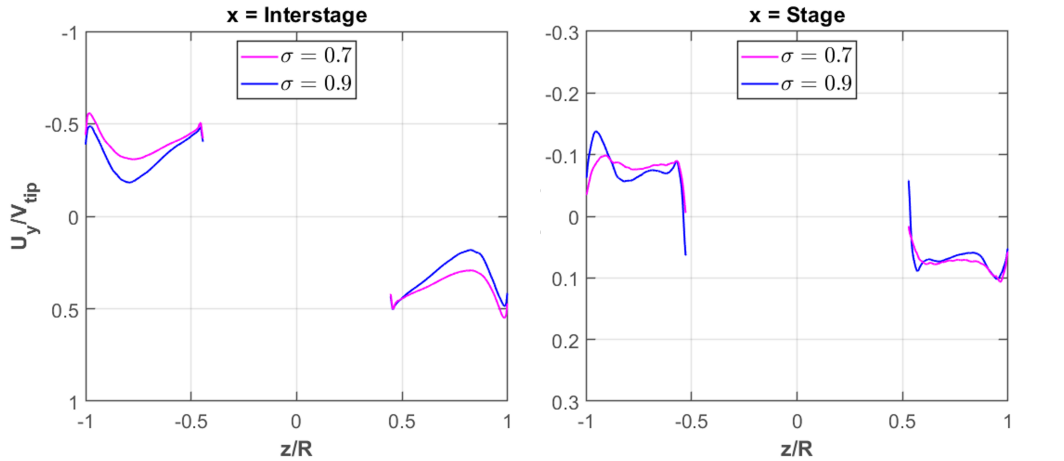

Figure 8.6: Radial velocity component, z' direction at $x' = 0.101\,m$ and $x' = 0.321\,m$

component is slightly higher, especially in the central area of the jet. However, this component is greatly reduced by the stator in both configurations, proving the efficiency of the element.

8.2.2 Instantaneous Flow

The visualization of instantaneous flow was realized by saving the fluid dynamic field around the engine. To visualize the turbulent characteristics of the flow processed by the two configurations a snapshot of the normalized vorticity magnitude ω^* is shown in Fig. 8.7. The normalized vorticity magnitude is defined as $\omega^* = \omega D_{rotor}/V_{tip}$ where D_{rotor} is the diameter of the rotor and V_{tip} is the velocity of the blade tip, already employed in the definition of other non-dimensional parameters.

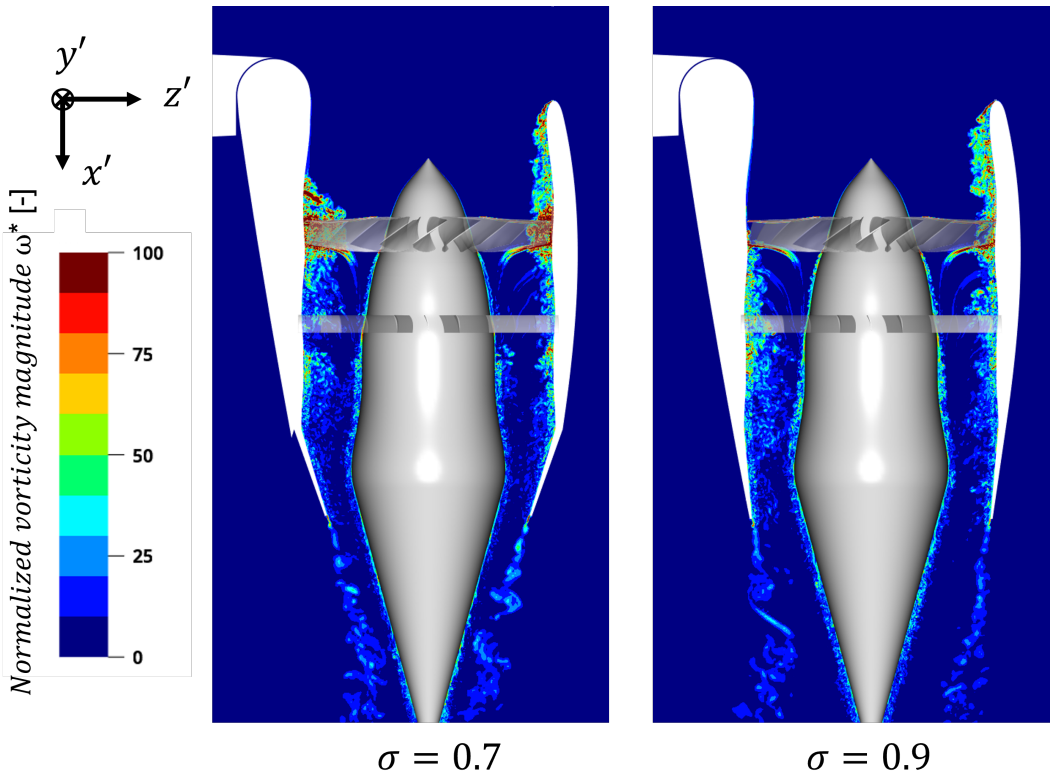

Figure 8.7: Snapshot of the vorticity magnitude inside the ducted fan for the two configurations

The vorticity provides a visualization of how the flow separation at the inlet lip is remarkably similar for the two cases. In contrast, case $\sigma = 0.7$ differs from $\sigma = 0.9$ by the presence of a second separation zone in front of the rotor disk. The highest ω^* values are located in the fluid-dynamic field around the rotor suggesting that this is the area that manufacturers need to focus on most to reduce the noise produced by this type of propulsion system.
In both the fluid fields the helical wake generated by the passage of the blades is visible. The vortex generated by the blade tip also known as *tip leakage vortex*, on the other hand, is not displayed distinctly probably due to the interaction of the

blade tip with the turbulent flow processed by the engine. To better visualize the vortex structures, normalized vorticity in the y direction ω_y^* is analyzed and shown in Fig. 8.8.

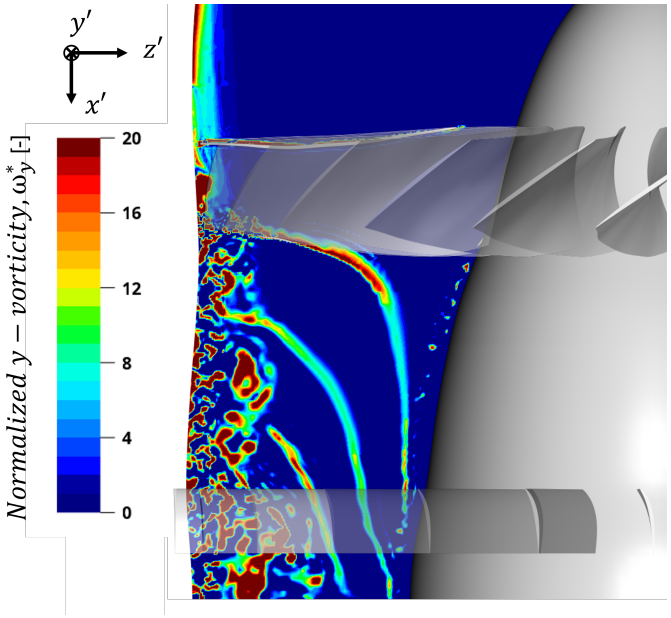

Figure 8.8: Snapshot of the vorticity magnitude inside the ducted fan for the two configurations

Baseline case $\sigma = 0.9$ is chosen for this analysis as already proven, on the wing side of the nacelle the flow is essentially axial and almost free of radial components. Therefore, the lack of interaction between blade and turbulent flow allows better visualization of the vortical structures generated by the blade passage. The tip leakage vortex is determined by the pressure difference between the two sides of the blade (ie. pressure and suction sides). The vortex size is limited by the action of the wall unlike what would happen for a free propeller where the missing wall would not restrict the size of the vortex structure. Several turbulent structures are present in the case under analysis, but the tip leakage vortex cannot be distinguished. Rather, it is evident how the wake generated by the blades passes interacts with the turbulent structures located near the surface of the nacelle. Moreover, due to the contraction of fluid, the latter also shifts toward the centre of the flow.
According to the performance analysis, the 0.7 case caused the stator to work in a non-ideal condition, causing localized losses behind it. The normalized vorticity magnitude ω^* was analyzed on an XY plane at $r/R = 0.5$ of the rotor blade to confirm the presence of this effect.
As shown in the figures 8.9, for $\sigma = 0.7$ case the flow comes to the stator with an angle of attack which anticipates flux separation on the suction side of the

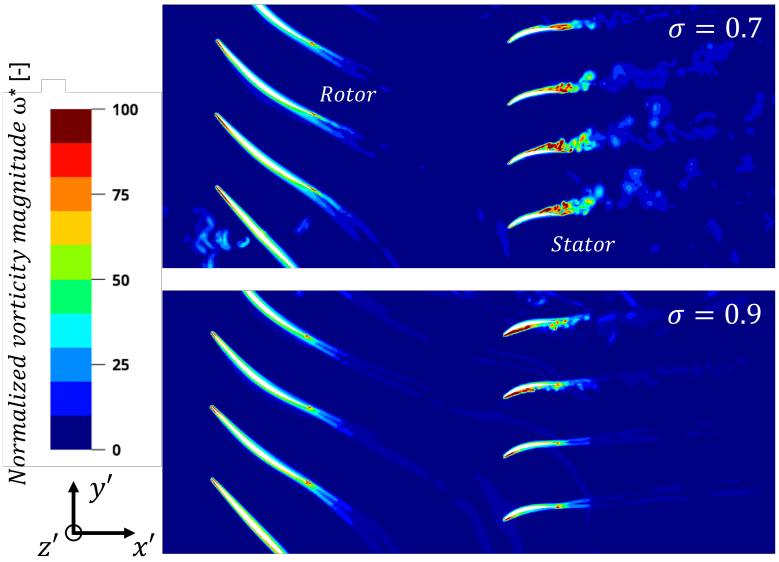

Figure 8.9: Snapshot of the vorticity magnitude on a XY plate at $r/R = 0.5$

blade, thus resulting in a wide wake which increases flux vorticity component and unsteady forces acting on the stator.
Conversely, in $\sigma = 0.9$ case, the angle of attack is near the optimal, leading to a more limited wake and thus a reduced increase in vorticity.

8.3 Acoustics analysis

The fluid-dynamic phenomena explored in the previous sections constitute the sources that impact the near-field and far-field acoustic of the engine. A good method for visualizing the acoustic wavefronts is through calculation of the instantaneous dilation field defined as follows:

$$\Theta = \nabla \cdot \mathbf{u} = -\frac{1}{\rho_0 c_0^2} \frac{\partial p}{\partial t} \tag{8.1}$$

where ρ_0 and c_0 are respectively the media density and speed of sound.
The instantaneous pressure, velocity and density were sampled on an XZ plane that symmetrically cuts the model with a frequency of $f_{sampling} = 20\,kHz$ which is the same as the one used for FWH surfaces. The time derivative of the pressure was calculated using the tool PowerACOUSTIC which has been used also for the far-field analysis. Fig. 8.10. compares the dilatation field of the two configurations. First, the visualization allows verifying how non-reflection and wave absorption settings (acoustic sponge) in the simulation setup phase were correctly defined. Indeed, the field does not show reflections from boundaries.

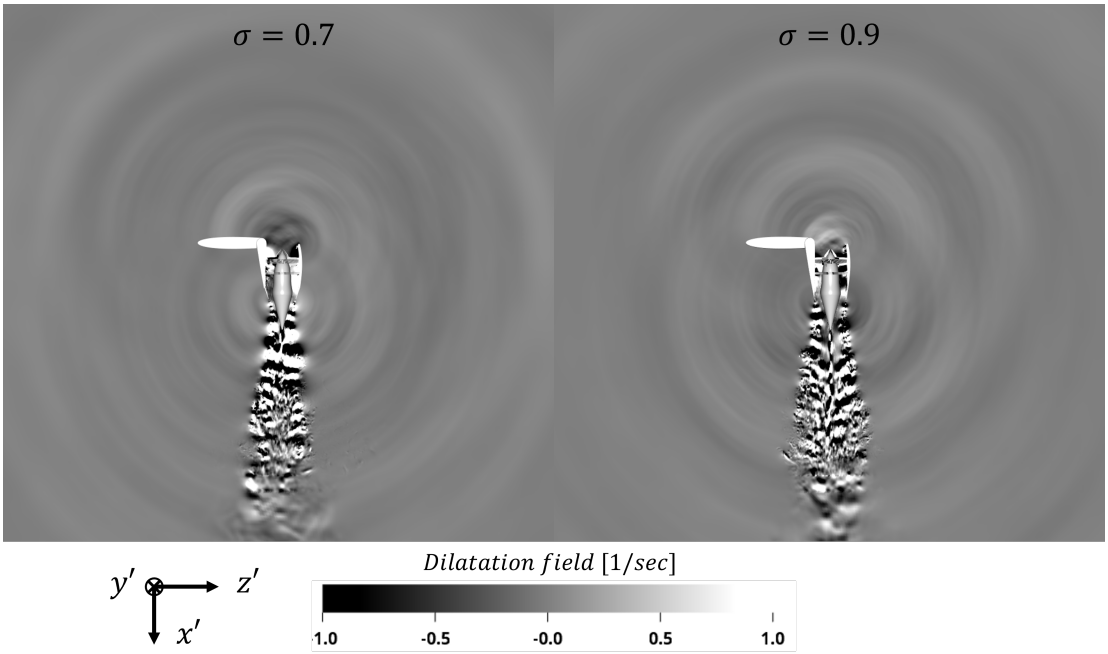

Figure 8.10: Comparison of the instantaneous Dilatation field of the two configurations

The dilation field provides an opportunity to localize the main acoustic sources and to value the directivity characteristics of the acoustic pressure fluctuations generated by the engine. Concerning the direction of sound propagation, the shielding action of the duct is visible, especially at the inlet of the engine. Pressure fluctuations generated by the rotor rotation are radiated in the vertical direction instead of being propagated in all directions as in the case of a free propeller. The directivity of these fluctuations is found to be imposed by the duct geometry. This important result is supported by what was found during the literature review: the acoustic field of a ducted fan/propeller is highly influenced by the directivity imposed by the presence of the structure around the rotating element, thus is significantly different from that produced by a free propeller.
The same directivity pattern is not found at the nozzle exit. Here, the flow energized by the rotor flows into a steady environment, causing a mass injection that introduces a strong fluctuation in the surrounding field. The acoustic wavefront radiates both in the direction of the wake and to the side of the engine, thus impacting the lateral acoustic field. Figure 8.11 provides a picture of the dilatation field inside and near the engine. The influence of the unsteady phenomena occurring inside the engine on the pressure fluctuations is clearly visible in this picture.
The fastest pressure fluctuations are located in the wake. However, significant

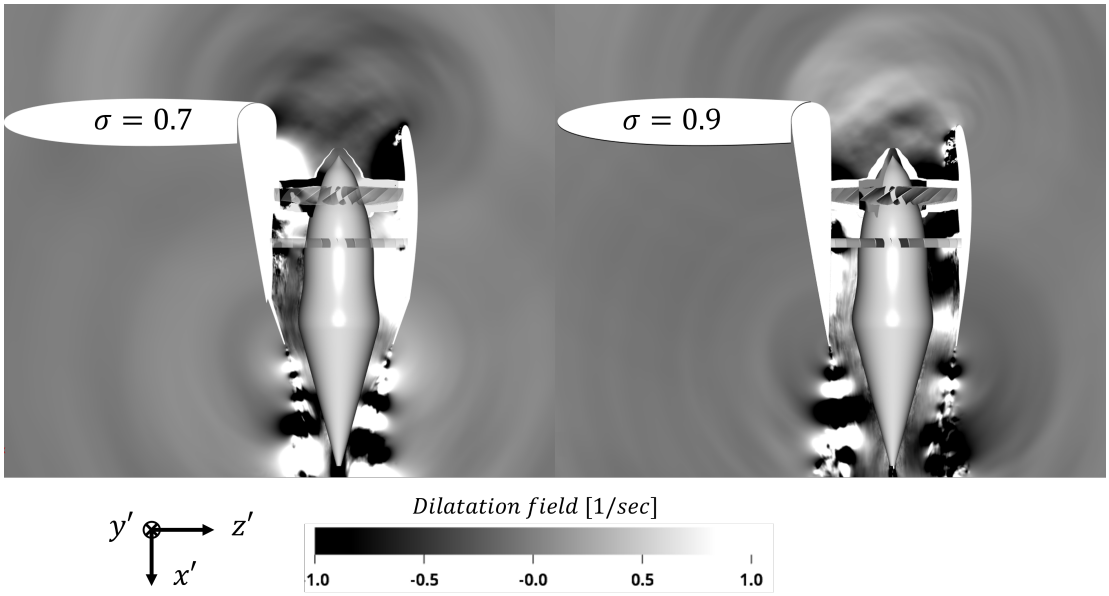

Figure 8.11: Detail of the instantaneous dilatation field of the two configurations

power sources are not displayed here. Predominant sound sources are therefore located at the nozzle exit and in the rotor region.
From the analysis of the fluid field, it was found that the turbulence resulting from the inlet lip separation results in two effects: the interaction of a turbulent flow with the rotor blades and the development of a non-symmetrical flow which is then processed by the engine. The strong fluctuations in the forces that the fluid applies to the structures resulting from these phenomena represent a strong acoustic source. Figure 8.10 also provide an important information. In both cases, fluctuations on the wing side of the engine are weaker. The wing is acting like a barrier against the acoustic waves resulting in a region where perturbations are weaker if compared with, for example, the region in front of the inlet. This effect is further examined in the next section.

8.3.1 Far-field analysis

As already introduced in Chapter 5, a far-field analysis of the acoustic field generated by the engine has been carried out using the FWH acoustic analogy. In this way the computational cost of the acoustic analysis is limited to the sampling region as the acoustic pressure is radiated from the FWH surfaces to the observer location (ie. the microphone locations). In this thesis, the FWH permeable method has been employed in the far-field analysis.
The aim is to characterize the sound pressure level and the directivity of the sound

emitted by the engine at a distance of $30.5\,m$ which represents the *High hover height* of the vertiport model presented in section 5.3.2 which was taken as a reference. Microphone data has been processed using Welch's method to estimate the power spectra of the signals. The sound pressure level was then calculated by making use of the following equation:

$$SPL = 10\,log_{10}\left(\frac{PSD}{p_{ref}^2}\right)\,[dB] \tag{8.2}$$

where PSD is the power spectral density of the signal and the reference pressure p_{ref} is equal to $p_{ref} = 2\,10^{-5}\,Pa$.
The directivity of the sound emitted by the engine can be characterized by analysing the overall sound pressure level (OASPL) for each microphone used in the far-field analysis. Figure 8.12 shows the axial directivity of the OASPL on the XZ symmetry plane of the engine. Frequencies between $80 - 8000\,Hz$ were considered in the computation. In the following discussion, the position of the microphones is expressed in terms of the angle θ as it is easier to switch to polar coordinates for this discussion. The directivity of the two configurations is almost identical

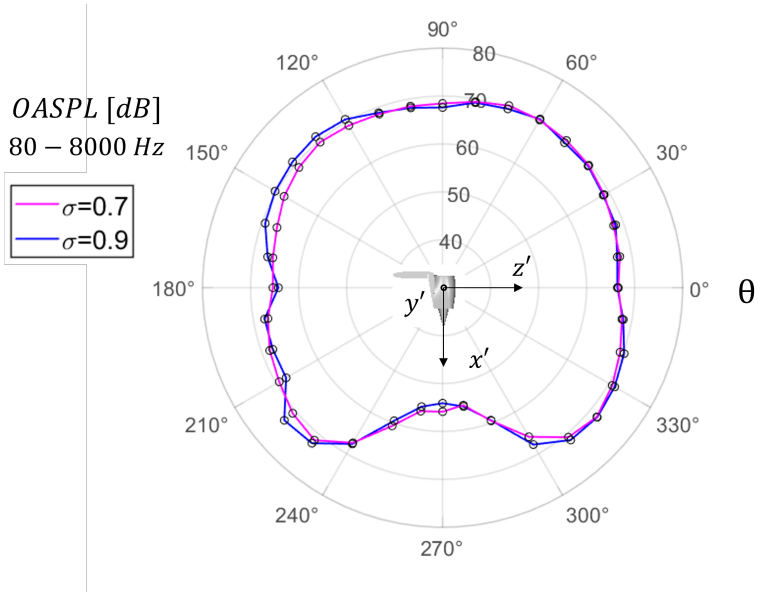

Figure 8.12: Directivity of OASPL at $r = 30.5\,m$, frequency range $80 - 8000\,Hz$

but there are local differences in measured SPL. The same characteristics of the acoustic field outlined by the visualisation of the dilation field are found in this analysis. The highest values are found at the microphones located in the upper part of the field, namely in the direction of the engine inlet (between $\theta = 30°$ and $\theta = 150°$). The values obtained from the microphones placed sideways, on the

other hand, are visibly lower. The difference is about 4 dB, which indicates that the sound power is halved in this direction. If, on the other hand, data obtained from microphones located in the direction of the wing and those symmetrical to them with respect to the XY plane are compared, no major differences are found. Moving on both sides of the engine towards the lower side ($x' > 0$ direction), the sound pressure level recorded increases again up to $\theta = 240°$ and $\theta = 300°$ right before the region affected by the engine wake. These microphones are located in the direction of the wavefronts generated by the jet stream flowing into the environment. Lower values found in the microphones located in this region can be justified by considering that the contribution of the lower face of the permeable surface was not taken into account during data processing for the far-field analysis. Figure 8.13 shows the difference in overall sound pressure level computed by the microphones Δ_{OASPL} between the two configurations.

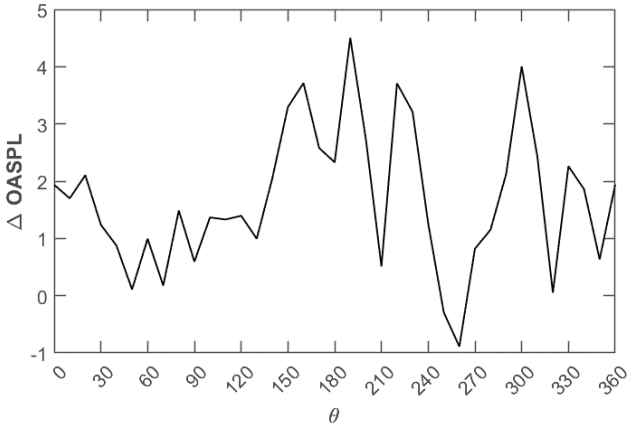

Figure 8.13: Difference between the OASPL computed for the two cases, $\Delta_{OASPL} = OASPL_{0.9} - OASPL_{0.7}$

Overall, the baseline configuration $\sigma = 0.9$ proves to produce a more powerful acoustic field than the $\sigma = 0.7$ configuration with peaks even above 3dB. This result can be attributed to several factors. The output speed of the two configurations is the same, thus jet velocity is not one of the main factors determining the difference. These must be sought in the characteristics of the flow that settles inside the ducted fan and which is processed by the engine. As the flow analysis revealed, the inlet separation produces a non-symmetrical flow that leads to the generation of a non-constant thrust by the engine. Furthermore, the turbulence generated by this condition being processed by the rotor interacts with the other turbulent structures in the flow, increasing the overall interactions between the latter.
Finally, figure 8.14 presents the power spectrum analysis of the noise signal at two different locations. The spectrum analysis is performed applying Welch's method

with a frequency bandwidth of $\Delta f = 80Hz$ and an overlapping factor between the window of 50%. Spectral analysis reveals the power contributes of each frequency to the acoustic field at the microphone location. Moreover, by normalizing the frequencies with the blade passage frequency (BPF) it is possible to visualize the tonal contribution to the acoustic field.

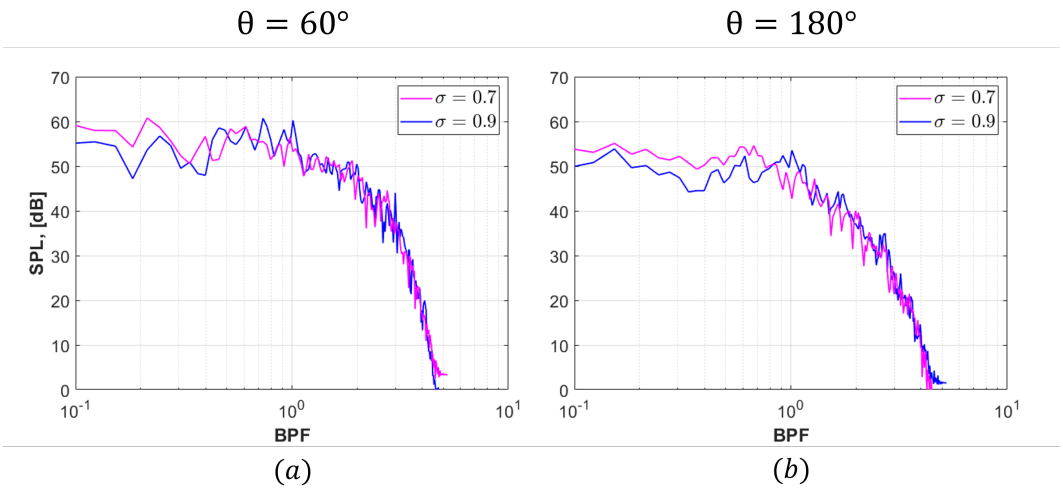

Figure 8.14: Power spectrum analysis for two microphones located at $\theta = 60$ (a) and $\theta = 180$ (b)

Based on the directivity analysis shown in Figure 8.12 microphones located at $\theta = 60$ (a) and $\theta = 180$ (b) were selected for the analysis. The aim is to find the differences in the two power spectra and the reason for the difference in the acoustic field between the two points in terms of OASPL. In both cases, the contribution of the tonal peaks is visible only for the baseline configuration ($\sigma = 0.9$), especially at $\theta = 60°$ where the first three BPF are visualized. In contrast, the $\sigma = 0.7$ shows no tonal contribution to the spectrum in both locations. It appears that the broadband noise covers the BPF frequencies affecting the entire spectrum of the engine. Tonal peaks related to the BPF represent a greater contribution to the noise produced by a propulsion system of this type, the lack of these peaks can be considered as one of the elements that led to lower acoustic power for $\sigma = 0.7$ case. Comparing the two microphones, on the other hand, it can be seen that the high frequencies in $\theta = 60$ result in a smaller contribution to the OASPL as they decay faster.

Chapter 9

Conclusions and Recommendations

The objective of this thesis was to investigate the effect of a variable nozzle on the aerodynamic and acoustic field of a ducted fan installed in an over-the-wing (OTW) configuration. Several conclusions can be drawn from the analysis of the calculations; the most important results are grouped in the following section according to the research aim, defined at the beginning of the project. Moreover, Section 9.2 introduces the reader to a series of recommendations and advice for the future development of the project.

9.1 Conclusions

The first aim of the project was to understand the main aerodynamic and acoustic characteristics of ducted fans operating at typical RPM for eVTOL application. The review of the literature resulted in the following findings:

- **Flow field**: Several factors contribute to the characterisation of the flow field of this particular propulsion system, and analyzing their influence on performance is challenging The design of the engine cover plays a key role as it affects the incoming flow and thus impacts the properties of the flow processed by the rotor. Usually, the nacelle is designed to be efficient in the longest phase of the mission, the cruise. However, as this type of propulsion system can also be used to produce thrust during hovering, the conditions under which the nacelle operates change dramatically. When operating in hover, a small lip radius produces strong streamlines distortion and inlet separation which then results in a turbulent flow being ingested by the engine. Another key parameter in the ducted fan design is the tip clearance (ie. the distance between the blades and the nacelle surface). The closer the blades are to the

surface of the nacelle, the greater the thrust generated by the engine under the same operating conditions. Moreover, by keeping this distance small the tip leakage vortex size is reduced, thus positively impacting performance and efficiency. The presence of the duct makes it possible to properly design the stator vanes, which helps reduce the swirl component of the fluid and thus increase the thrust.

- **Acoustic field**: The presence of the duct determines a strong influence on the directivity of the sound generated by the engine. Noise is mainly radiated in the direction of the inlet while for an open propeller this type of directivity is not found. The duct provides also a surface on which acoustic liners can be installed. The main acoustic signature are: a tonal noise which is related to the blade passage frequencies and a broadband noise which is weaker and is related to other unsteady processes.

- **Over-the-wing configuration**: The effect that the installation of a ducted fan above a wing has on the performance of the two elements has been little discussed in the literature. However, since in this configuration the propulsion system can be seen as a boundary layer injection configuration, the same effect can be applied.

The second phase of the thesis aimed to determine the general effect that the area ratio σ has on the performance of this propulsive system when operating in hover. A 3D CAD model of a ducted fan was therefore created incorporating all the main characteristics of this propulsion system and replicating the technical solution proposed by the German company Lilium. Performance maps of four nozzle configurations were produced by modifying the engine operating condition (ie. RPM) among three different settings (60%, 80% and 100% of the hypothetical max power $RPM = 5344$) for a total of twelve low-fidelity simulations. The three scenarios found are summarized below:

1. **Convergent nozzle ($\sigma = 0.7$)**: In a convergent exit nozzle configuration $\sigma < 1$ the mass flow elaborated by the engine is reduced. The flow is re-accelerated as it passes through the converging nozzle thus no separation is found before the exit. However, the sudden reduction in the area creates a high-pressure zone that acts as a barrier and influences the incoming flow and in general the efficiency of both rotor and stator. The configuration leads to a lower thrust and higher losses.

2. **Linear nozzle ($\sigma = 0.9$ / $\sigma = 1.1$)**: A linear exit nozzle do not affect the incoming flow as in the case of convergence. It is more efficient as in this configuration the engine can produce the highest total thrust values. However,

losses can be detected in the nozzle area as the flow slows down approaching the condition at which it separates from the nozzle surface. if this does not happen before exit, losses are reduced.

3. **Divergent nozzle ($\sigma = 1.3$)**: The assumption at the heart of the analysis is that the engine can work in a better condition if during hover the nozzle is opened, thus increasing the area ratio σ. Results, however, show different behaviour. When the nozzle is settled into a divergent configuration (σ >1) flow separation occurs inside the nozzle. This causes the flow to experience a smaller outlet area (compared to that which would be the case with the attached flow) which affects the processed mass flow rate. It also results in a lower axial velocity at the outlet and high losses.

Even though the results achieved depend heavily on the geometry of the model used and cannot be considered true as they were obtained from low-resolution analyses, it was possible to state that the engine performs better with the variable nozzle in an "open" rather than a "closed" configuration. However, there is a limit in the area ratio of the engine beyond which the beneficial effect vanishes and a negative effect arises. From these results, nozzle configurations 0.9 and 0.7 were selected for the high-resolution fluid dynamic and acoustic field analysis.
Several important results emerge from this analysis that confirm what has already been found in the literature review:

- In hover condition the small nacelle lip radius produces high distortion to the streamlines and thus inlet separation. The turbulent is then processed by the engine, leading to strong interactions between the turbulent structures and the rotor. The latter then experiences strong fluctuations in the forces acting on it. Furthermore, the separation results in a non-symmetry in the flow processed by the engine, thus leading to an imbalance of the thrust.

- In the $\sigma = 0.7$ case the lower exit area ratio results in a lower mass flow being elaborated by the engine. The convergent nozzle affects the fluid field elaborated by the engine, separations occur on stator blades and in front of the rotor on both sides of the nacelle. For the $\sigma = 0.9$ case this behaviour is not found.

- The engine is found to be more efficient for $\sigma = 0.9$ case with a stage adiabatic efficiency equal to 53% while for the $\sigma = 0.7$ the efficiency is 5% lower. Also, the total thrust is higher in the first configuration.

- A circular array of 36 microphones is placed around the engine on the XZ symmetry plane at a distance $r = 30.5\,m$. The directivity of the acoustic field imposed by the duct and wing is found in the results of the far-field

analysis and the dilatation field visualization. The difference in terms of OASPL between two microphones, one located in the direction of the engine inlet and the second located on the side of the engine turns out to be around 4 dB.

- the engine with an area ratio $sigma = 0.9$ is noisier than the other. Since the axial output speed of the two configurations is the same and the quadrupolar contribution is minimal, the source of the difference resides in the magnitude of the unstable forces acting on the engine and the larger size of the output area

9.2 Recommendations

As a guide for future analyses of ducted fan-type propulsion systems in over-the-wing configurations, the following recommendations and advice are provided.

- **Experimental analysis**: The analyses performed in this research were carried out through the use of numerical simulations. Although the data obtained represent a good means of understanding the performance and characteristics of the architecture studied, they do not have absolute validity. To better validate the results, it would therefore be necessary to carry out experimental analyses on a realistic model to extract the fluid and acoustic field characteristics.

- **Definition of a known ducted fan model**: The lack of known geometries in the literature made it very complex to create a model that met all the characteristics sought. Furthermore, the use of a new model does not allow the analyses carried out to be compared with others already present in the literature. The results obtained, therefore, provide a good overview of the fluid-dynamic and aeroacoustic characteristics of a propulsion system of this type, without however verifying the actual validity of the data obtained. It is therefore recommended the creation of a basic model that can be used freely and thus allow the results of different analyses to be compared in order to allow the technological advancement of this engine.

- **High-resolution performance analysis**: The overall effect of the variable nozzle on the performance of the engine was carried out with low-resolution simulations. Results are thus grid dependent and can not be used as a reference. An investigation of the nozzle effect on the performance should be done with a higher resolution mesh and the convergence of the simulations must be investigated through a grid convergence study.

- **Solid FWH surface**: The far-field analyses presented in the chapter were carried out by employing the acoustic analogy of FWH applied to a permeable surface. To better validate these results, the far-field analyses could be compared with the results obtained by applying the FWH solid analogy in the same conditions of the current investigation.
- **Ground reflection**: Fluid dynamic and acoustic analyses were carried out without considering the ground effect on both the engine performance and the acoustic field. Is therefore recommended to extend the simulations to a case where the presence of the ground is modelled by a surface placed at a well know distance from the engine.
- **Cruise configuration analysis**: The thesis focused on the acoustic and performance characteristics of the model for a hover configuration. Analysing the same nozzle configurations during a hypothetical cruise phase would provide a broader view of the performance and acoustic characteristics of this novel architecture.
- **e-VTOL certification**: Currently, the e-VTOL category lacks regulation in terms of both noise produced and performance. It is expected that such regulations will be published in the coming years. Consequently, to better position the characteristics of this propulsion system with the guidelines defined by the regulatory bodies, analyses should be carried out with reference to these guidelines.

Bibliography

[1] M.Hader, S.Baur, S.Kopera, T.Schonberg, and J-P Hasenberg. *Urban Air Mobility: USD 90 billion of potential: How to capture a share of the passenger drone market*. Tech. rep. The Roland Berger Center for Smart Mobility, Sept. 2020.

[2] Department of Economic United NAtions and Social Affairs Population Division. *World Urbanization Prospects, The 2018 Revision*. Tech. rep. New York, 2019.

[3] Urban Air Mobility NASA. *Urban Air Mobility Market Study*. Tech. rep. Sept. 2018.

[4] P. Nathen, A. Strohmayer, R. Miller, S. D. Grimshaw, and J. Taylor. «Architectural performance assessment of an electric vertical take-off and landing (e-VTOL) aircraft based on a ducted vectored thrust concept». In: Apr. 2021.

[5] P. Schmollgruber, D. Donjat, M. Ridel, I. Cafarelli, O. Atinault, C. François, and B. Paluch. «Multidisciplinary design and performance of the onera hybrid electric distributed propulsion concept (Dragon)». In: vol. 1 Part F. American Institute of Aeronautics and Astronautics Inc, AIAA, 2020, pp. 1–27. ISBN: 9781624105951. DOI: 10.2514/6.2020-0501.

[6] Simon Marié, Denis Ricot, and Pierre Sagaut. «Comparison between lattice Boltzmann method and Navier–Stokes high order schemes for computational aeroacoustics». In: *Journal of Computational Physics* 228.4 (2009), pp. 1056–1070. ISSN: 0021-9991. DOI: https://doi.org/10.1016/j.jcp.2008.10.021.

[7] B.Eng. S.L.Dixon. *Fluid Mechanics and Thermodynamics of Turbomachinery (5th Edition)*. Elsevier, 1998. ISBN: 978-0-7506-7870-4.

[8] Ali Akturk and Cengiz Camci. «Tip clearance investigation of a ducted fan used in VTOL UAVs part 1: Baseline experiments and computational validation». In: vol. 7. 2011, pp. 331–344. ISBN: 9780791854679. DOI: 10.1115/GT2011-46356.

[9] J. Pereira. «Hover and wind-tunnel testing of shrouded rotors for improved micro air vehicle design». PhD thesis. Jan. 2008.

[10] R. Arina. «Introduction to Aeroacoustics». In: Politecnico di Torino, 2021.

[11] Thomas Rossing. *Springer handbook of acoustics*. Springer Science & Business Media, 2007.

[12] S. Glegg and W. Devenport. *Aeroacoustics of Low Mach Number Flows Fundamentals, Analysis, and Measurement*. Elsevier, 2017. ISBN: ISBN 978-0-12-809651-2.

[13] S.W. Rienstra and A. Hirschberg. *An Introduction to Acoustics*. 2021.

[14] Romani.G. «Computational aeroacoustics of rotor noise in novel aircraft configurations: A lattice-Boltzmann method-based study». PhD thesis. 2022.

[15] T. Zhang and G. N. Barakos. «Review on ducted fans for compound rotorcraft». In: vol. 124. Cambridge University Press, July 2020, pp. 941–974. DOI: 10.1017/aer.2019.164.

[16] Rodolfo Bontempo, Massimo Cardone, Marcello Manna, and Giovanni Vorraro. «Ducted propeller flow analysis by means of a generalized actuator disk model». In: vol. 45. Elsevier Ltd, 2014, pp. 1107–1115. DOI: 10.1016/j.egypro.2014.01.116.

[17] Paul F Yaggy, Amesresearch Center, and Kenneth W Goodson. *Aerodynamics of tiltind ducted-fan configurations*. NASA.

[18] Ali Akturk and Cengiz Camci. «Experimental and computational assessment of a ducted-fan rotor flow model». In: vol. 49. American Institute of Aeronautics and Astronautics Inc., 2012, pp. 885–897. DOI: 10.2514/1.C031562.

[19] Preston Martin and Chee Tung. *Performance and Flowfield Measurements on a 10-inch Ducted Rotor VTOL UAV*. June 2004.

[20] Will Graf, Jonathan Fleming, and Wing Ng. *Improving Ducted Fan UAV Aerodynamics in Forward Flight*. 2008.

[21] Ghanem F. Oweis, David Fry, Chris J. Chesnakas, Stuart D. Jessup, and Steven L. Ceccio. «Development of a tip-leakage flow - Part 2: Comparison between the ducted and un-ducted rotor». In: *Journal of Fluids Engineering, Transactions of the ASME* 128 (4 2006), pp. 765–773. ISSN: 00982202. DOI: 10.1115/1.2201619.

[22] Dhwanil Shukla and Narayanan Komerath. «Rotor–duct aerodynamic and acoustic interactions at low Reynolds number». In: *Experiments in Fluids* 60 (1 Jan. 2019). ISSN: 07234864. DOI: 10.1007/s00348-018-2668-z.

[23] Reynard de Vries, Nando van Arnhem, Francesco Avallone, Daniele Ragni, Roelof Vos, Georg Eitelberg, and Leo L. M. Veldhuis. «Experimental Investigation of Over-the-Wing Propeller–Boundary-Layer Interaction». In: *AIAA Journal* 59 (6 June 2021), pp. 2169–2182. ISSN: 0001-1452. DOI: 10.2514/1.j059770.

[24] T. Zhang, G. Qiao, D. A. Smith, G. N. Barakos, and A. Kusyumov. «Parametric study of aerodynamic performance of equivalent ducted/un-ducted rotors». In: *Aerospace Science and Technology* 117 (Oct. 2021). ISSN: 12709638. DOI: 10.1016/j.ast.2021.106984.

[25] Alastair McIntosh. *Technology behind the Lilium Jet*. URL: https://lilium.com/newsroom-detail/technology-behind-the-lilium-jet.

[26] Tao Zhang and George N. Barakos. «High-fidelity numerical analysis and optimisation of ducted propeller aerodynamics and acoustics». In: *Aerospace Science and Technology* 113 (June 2021). ISSN: 12709638. DOI: 10.1016/j.ast.2021.106708.

[27] Harvey H. Hubbard. *Sound measurements for five shrouded propellers at static conditions*. Tech. rep. NACA-TN-2024, 1950.

[28] Anwar M.N. Malgoezar, Ana Vieira, Mirjam Snellen, Dick G. Simons, and Leo L.M. Veldhuis. «Experimental characterization of noise radiation from a ducted propeller of an unmanned aerial vehicle». In: *International Journal of Aeroacoustics* 18 (4-5 July 2019), pp. 372–391. ISSN: 20484003. DOI: 10.1177/1475472X19852952.

[29] S. M. Alavi Moghadam, M. Meinke, and W. Schröder. «Analysis of the acoustic field of a ducted axial fan». In: *23rd AIAA/CEAS Aeroacoustics Conference, 2017* (2017). DOI: 10.2514/6.2017-3873.

[30] Hugo F.M. Bento, Reynard de Vries, and Leo L.M. Veldhuis. «Aerodynamic performance and interaction effects of circular and square ducted propellers». In: American Institute of Aeronautics and Astronautics Inc, AIAA, 2020, pp. 1–21. ISBN: 9781624105951. DOI: 10.2514/6.2020-1029.

[31] Gianmarco Bianchi, John Doherty, and Michael Pekris. «Aerodynamic Investigation of a Boundary Layer Ingestion Wing-Electric Ducted Fan Model». In: *The Future of Aerodynamics The Future of Aerodynamics-Royal Aeronautical Society Applied Aerodynamics Conference, Bristol* (July 2018).

[32] E. A.P. Marcus, R. De Vries, A. Raju Kulkarni, and L. L.M. Veldhuis. «Aerodynamic investigation of an over-the-wing propeller for distributed propulsion». In: American Institute of Aeronautics and Astronautics Inc, AIAA, 2018. ISBN: 9781624105241. DOI: 10.2514/6.2018-2053.

[33] Alejandra Uranga, Mark Drela, David K. Hall, and Edward M. Greitzer. «Analysis of the aerodynamic benefit from boundary layer ingestion for transport aircraft». In: *AIAA Journal* 56 (11 2018), pp. 4271–4281. ISSN: 00011452. DOI: 10.2514/1.J056781.

[34] Erlend Magnus Viggen. «The lattice Boltzmann method: Fundamentals and acoustics». PhD thesis. Feb. 2014.

[35] et al. T.Krüger. *The Lattice Boltzmann Method*. Springer International Publishing, 2017. DOI: https://doi.org/10.1007/978-3-319-44649-3.

[36] D. Herrmann. *A study of the suitability of powerflow as an educational engineering design tool for undergraduate students*. Tech. rep. University of Stuttgart.

[37] Yuanxun Bao and Justin Meskas. *Lattice Boltzmann Method for Fluid Simulations*. Tech. rep. New York University, Apr. 2014.

[38] Dassault Systèmes. «SIMULIA PowerCASE User's Guide». In: June 2020.

[39] D. Casalino. «An advanced time approach for acoustic analogy predictions». In: *Journal of Sound and Vibration* 261.4 (Apr. 2003), pp. 583–612. DOI: 10.1016/S0022-460X(02)00986-0.

[40] P. di Francescantonio. «A new boundary integral formulation for the prediction of sound radiation». In: *Journal of Sound and Vibration* 202 (May 1997), pp. 491–509. ISSN: 0022460X. DOI: 10.1006/jsvi.1996.0843.

[41] D.M. Nark L.V. Lopes D.D. Boyd and K.E. Wiedemann. «Identification of Spurious Signals from Permeable Ffowcs Williams and Hawkings Surfaces». In: 73rd American Helicopter Society Annual Forum (FORUM 73). May 2017.

[42] S.K. Lele S. Mendez M. Shoeybi and P. Moin. «On the use of the FfowcsWilliams-Hawkings Equation to Predict Far-Field Jet Noise from Large-Eddy Simulations.» In: *International Journal of Aeroacoustics* 12 (Jan. 2013), pp. 1–20. DOI: 10.1260/1475-472X.12.1-2.1.

[43] W.C.P. Van Der Velden. «Computational aeroacoustic approaches for wind turbine blade noise prediction». PhD thesis. Delft University of Technology, 2017. DOI: 10.4233/UUID:EA709745-7238-47E0-90D1-C8381FD34F39.

[44] Christopher E. Hughes. «Aerodynamic performance of scale-model turbofan outlet guide vanes designed for low noise». In: 2002. DOI: 10.2514/6.2002-374.

[45] *Vertiports Prototype Technical Specifications for the Design of VFR Vertiports for Operation with Manned VTOL-Capable Aircraft Certified in the Enhanced Category (PTS-VPT-DSN)*. 2022.

[46] P.J. Roache. *QUANTIFICATION OF UNCERTAINTY IN COMPUTATIONAL FLUID DYNAMICS*. 1997, pp. 123–60. URL: `www.annualreviews.org`.